UNIVERSITY OF CALIFORNIA
SANTA CRUZ

THE BIRTHS OF PLANETS AND DEATHS OF STARS

A dissertation submitted in partial satisfaction of the
requirements for the degree of

Doctor of Philosophy

in

ASTRONOMY AND ASTROPHYSICS

by

Tyler Takaro

September 2022

The Dissertation of Tyler Takaro is approved:

Ruth Murray-Clay, Chair

Enrico Ramirez-Ruiz

Andrew Skemer

Connie Rockosi

Peter Biehl
Vice Provost and Dean of Graduate Studies

Table of Contents

List of Figures

List of Tables

Abstract

The Births of Planets and Deaths of Stars

by

Tyler Takaro

This thesis studies the formation of planets and the destruction of stars that explode as supernovae. To understand planet formation and recreate the diversity of exoplanets that we see in our galaxy, we need a better understanding of protoplanetary disks. We develop a time-evolving model for the solid particles in these disks, tracking maximum particle size and surface density in their outer regions. This time dependent particle modeling shows us that disks pass through several regimes as more particles drift inwards, lowering maximum particle sizes and surface densities. By combining this model with our model for pebble accretion, we are able to estimate growth rates for injected protoplanetary cores. Applying our models to a sample of seven disks, we find that planetesimals should grow rapidly, particularly early in the disk's lifetime before it has drained too much. To reproduce observed planetary masses, we find that protoplanetary cores must reach planetesimal sizes before the ages of typically observed disks.

Turning our attention to smaller particles, we develop a new model for pebble accretion to explore the growth of lower mass protoplanetary cores. We apply full gas effects to the dynamics of small cores, finding that their new velocities play a crucial role in understanding their growth. Additionally, we model full probability distributions for the relative velocities of interacting particles, rather than simply studying the mean

velocity. As we extend the model down to cm scales, we find that gas interactions play the dominant role in setting relative velocities for inter-particle collisions. At these small scales especially, particles in the low velocity tail of the velocity distribution can be accreted particularly rapidly, enhancing growth. In examining these rare growth interactions, our model suggests a path for solid body growth across the meter-scale barrier, up to planetesimal masses.

Finally, I also present my work statistically modeling the ages of Type Iax supernova progenitor stars. In this study, we use Hubble Space Telescope photometry of the stellar regions around Type Iax supernovae explosion sites to estimate ages for these regions. This is performed by statistically rigorous fitting of theoretical stellar models to our multi-band photometry. We are ultimately able to generate probability distributions for the ages of each supernova we consider, generating strong constraints on the formation channel for these events.

Acknowledgments

I would like to thank my advisor Ruth Murray-Clay, whose time, wisdom, and advice have been fundamental in completing this thesis. Additionally, I would like to thank the rest of my committee, Enrico Ramirez-Ruiz, Connie Rockosi, and Andy Skemer, for all of their advice and assistance during my graduate career.

In addition, I would like to thank my friends and family for their support over the last six years. I would especially like to thank my partner Brenna whose unceasing love and support has helped to carry me at times over these years.

Published Material

The text of this dissertation includes reprints of the following published material led by Takaro, with the permission of the listed coauthors.

Chapter 4 was published in the literature as Takaro et al. (2020). I was responsible for developing the models, performing the analysis, writing the text, and creating the figures. I wish to thank my coauthors Ryan J. Foley, Curtis McCully, Wen-fai Fong, Saurabh W. Jha, Gautham Narayan, Armin Rest, Maximilian Stritzinger, and Kevin McKinnon, for their support and feedback in the course of this research. In addition to my co-authors, I'd like to thank Ruth Murray-Clay for her help in getting me to finish this paper.

Chapter 1

Introduction

In most astronomers' understanding, planets form in the disks surrounding young stars, also known as protoplanetary disks. These disks are made up of both small solid bodies (which we'll call dust, or pebbles), and a significant gaseous component. The interactions between these solid bodies and the gas in which they are embedded are key to understanding how planets form and grow. In this thesis, I develop models to understand both the dynamics and the evolution of protoplanetary disks and the planets which form within them.

In order to understand protoplanetary disks, we carefully model the growth and dynamics of the (mostly) small solid particles which compose the disks alongside their surrounding gas. The interactions between small particles (from initial ISM sizes of 10^{-5} cm (Mathis et al. 1977; Zubko et al. 2004) up to about ~ 10 cm) and the gas that surround them allow these particles to rapidly collide and grow up to these many cm scales.

The problem of growing solid bodies from initial dust sizes up to solid planetsimals can be broken into three components. First, we consider how a particle can grow from initial dust sizes up to $\sim$ 10 cm. Next, one must explain the growth from these many cm scales up to small planetesimal scales ($\sim 10^7$ cm). This is a difficult stage of growth, in part because particles at this size rapidly drift inwards towards the star before they can grow to larger sizes, a problem known as the "meter-scale barrier" (Weidenschilling 1977). Lastly, we have the stage of growth from planetesimal scales to final core masses. Pebble accretion has classically been used for this last stage of growth, as planetesimals are able to rapidly accrete small particles and reach final core masses. In this thesis, we expand this application, examining how gas and particle dynamics affect particle growth at all scales.

In addition to drift, particles also must reckon with fragmentation. If particles collide at high enough velocities, rather than sticking and growing, they may instead fragment, destroying one or both particles (Brauer et al. 2008; Zsom et al. 2010). In this way, fragmentation acts as another barrier to particle growth. For this thesis, we assume a certain collision velocity at which particles will fragment, and use this to model the limits that fragmentation puts on particle growth.

Pebble accretion (or gas-assisted growth) is able to explain the rapid growth of planetesimals to core masses by enhancing the cross-section for growth and decreasing the relative velocity between interacting particles. This is a result of the interactions between solid particles and the surrounding gas. An outward pressure gradient in protoplanetary disks causes the gas to rotate at a sub-Keplerian rate. The embedded particles

thus feel a headwind from the gas, slowing the particles and increasing the opportunities for favorable interaction between particles, increasing growth rates. The very same gas effect which causes a "meter-scale barrier" also allows larger planetesimals to grow at extremely rapid rates. Because pebble accretion has the potential to play a critical role in planet formation, the process has been studied extensively (e.g. Ormel & Klahr 2010; Perets & Murray-Clay 2011; Lambrechts & Johansen 2012; Ormel & Kobayashi 2012; Guillot et al. 2014; Lambrechts & Johansen 2014; Levison et al. 2015; Morbidelli et al. 2015; Ida et al. 2016; Visser & Ormel 2016; Chambers 2016; Johansen & Lambrechts 2017; Xu et al. 2017; Rosenthal et al. 2018; Rosenthal & Murray-Clay 2018; Bitsch et al. 2019).

1.1 Disk Model

Drawing on the work of Birnstiel et al. (2012), Lambrechts & Johansen (2014), and Powell et al. (2017), we examine these drift and fragmentation limited particle sizes in protoplanetary disks as they evolve. Modeling the particles' growth up to the minimum size at which they begin to drift, we track the progression of a pebble front outward through the disk. This pebble front is the location in the disk where particles are just now beginning to drift. Initially, particles are so small that they largely move with the gas flow orbiting the young star. Only once they grow large enough to maintain their own momentum independently from the gas do their velocities diverge from the gas flow, and they feel gas drag, causing them to drift inwards. As the disk evolves, the pebble front moves outward in the disk, as particles further out in the disk grow large

enough to begin to drift.

This point in time, when the maximum particle size changes defines a boundary between the two primary regimes that define a disk's era of planetary formation. As the maximum particle size evolves in these disks, so too does the overall solid surface density. Over time, more and more solids drift into the central star, steadily draining the disk of solid material from which to form planets. Understanding this evolving surface density allows us to predict when and where in the disk we expect growth to be the most effective.

While pebble accretion is remarkably efficient at rapidly forming planets, under certain conditions it can be too rapid to match with observations. As such, a need arises for a natural mass scale where pebble accretion halts. One such mass scale that has previously been suggested is the "pebble isolation" mass (Morbidelli & Nesvorny 2012; Lambrechts et al. 2014; Bitsch et al. 2018). This mass is defined as the point where a protoplanetary core becomes large enough that it generates a pressure bump which traps pebbles from drifting into the core's region of influence. An alternative mass scale, dubbed the "flow isolation" mass by Rosenthal & Murray-Clay (2020), occurs when the largest pebbles available in the disk are small enough that they couple to the gas flow around the core, preventing gas drag from further aiding core growth. This process isolates the core from the pebbles which it could use to grow, ending pebble accretion. In the outer disk, this "flow isolation" mass is smaller than the "pebble isolation" mass under nearly all reasonable disk conditions, meaning that flow isolation mass nearly always sets the limiting mass scale for pebble accretion in our model.

In order for a protoplanetary core to become flow-isolated, there must be a process which limits the maximum particle size in the protoplanetary disk. There are several different processes which can lead to this maximum particle size limit (Kusaka et al. 1970; Weidenschilling 1984; Beckwith et al. 2000; Testi et al. 2014). In this study, we focus on particle drift and fragmentation as the potential causes of this maximum particle size. The same headwind which decreases the relative velocity between particles and forms the foundation of pebble accretion theory also naturally limits particle size due to particle drift. Assuming that all particles are small enough ($St < 1$; see Section **??**), the larger a particle grows, the faster it drifts. As total growth times lengthen for larger particles, at a certain particle size, the growth time exceeds the drift time, and particles drift into the star before they can grow. This sets a "drift limited" maximum particle size. Additionally, as particles grow they become more susceptible to fragmentation. As detailed in Birnstiel et al. (2012), this process limits particles from growing larger than a "fragmentation limited" size, as any particles which are larger than this size are quickly ground down due to fragmentary collisions. Whether from drift or fragmentation, we expect the particles in protoplanetary disks to be largely limited to some maximum size, which allows the flow isolation paradigm to apply.

In this thesis, we apply this protoplanetary disk modeling to a sample of seven disks, studying the growth of potential planetesimals in these disks. We generate maximum particle size and surface density estimates, modeling how these evolve as the disk ages. We also use our pebble accretion model to generate predicted growth times for planetesimals injected into these disks, finding that growing early in the disks' lives is

key to planetesimals reaching typical planet masses.

1.2 Pebble Accretion Model

We modify and apply our pebble accretion model, first introduced in Rosenthal et al. (2018), and later expanded upon in Rosenthal & Murray-Clay (2018). This is an order-of-magnitude model, by which we mean that any approximations or neglected physics are such that all results are expected to be accurate to within an order-of-magnitude. In our model, we consider the system of two interacting bodies orbitting a central star. We call the larger of these two bodies the protoplanetary core, while we denote the smaller as the accreted particle. In contrast to Rosenthal et al. (2018), we allow both bodies to experience drag from the gaseous component of the protoplanetary disk. This, combined with the application of three different regimes of gas drag on the protoplanetary core, allow us to consider an extremely wide range of orbitting body sizes, from the sub-mm in radius up to many thousands of km.

The extent to which a solid particle is coupled to protoplanetary disk gas is typically parameterized in terms of the Stokes number. The Stokes number is a measure of the time it will take a particle to stop due to the gas drag it encounters, roughly in units of the particle's orbital period. For this reason, it is also known as the dimensionless stopping time. It can be calculated as $St = \frac{m v_{\rm rel} \Omega}{F_D}$, where F_D is the drag force experienced by the particle. One can also think of the Stokes number as a dimensionless measure of particle size, which better encapsulates the dynamic behavior of the particle under the influence of gas drag. Stokes numbers $\ll 1$ indicate small

particles which simply follow the local flow of gas, while Stokes numbers $\gg 1$ indicate large particles which are completely decoupled from the gas.

The full details of how the pebble accretion model operates can be found in Rosenthal et al. (2018); Rosenthal & Murray-Clay (2018), but we provide a brief summary here. To calculate a growth time for a protoplanetary core, we apply the approximation: $t_{grow} \sim \frac{m}{\rho \sigma v}$, where m is the mass of the core, ρ is the density of particles available for accretion, σ is the cross section for accretion in core-particle interactions, and v is the encounter velocity. Of these terms, both the cross section and the encounter velocity can take very different forms depending on the regime under consideration. The cross section in particular is largely determined by a comparison of the relative magnitude of R_{stab} (the minimum orbital radius for a particle to orbit about the core), and R_{Bondi} (the approximate scale height of core's budding atmosphere). We define and compare these radii in order to define the key regimes in which we model pebble accretion.

This atmospheric length scale, R_{Bondi}, can be approximated as the point at which the sound speed within the atmosphere equals the escape velocity from the planetesimal core. This radius is the point at which the thermal energy in the gaseous atmosphere is sufficient to liberate particles from being gravitationally bound to the planetesimal.

$$R_B = \frac{GM_p}{{c_s}^2} \tag{1.1}$$

where M_p is the mass of the planetesimal, and c_s is the sound speed of the gas.

The innermost stable orbital radius, $R_{\rm stab}$, is the scale at which the gas drag force on an orbiting particle matches the gravitational force from the core acting on the particle. That is,

$$R_{\rm stab} = \sqrt{\frac{GM_p m}{F_D}} \tag{1.2}$$

where m is the mass of the smaller body, and F_D is the gas drag force on the small body.

When $R_{\rm stab} > R_{\rm Bondi}$, particles can orbit the core without entering the more dense proto-atmosphere. On these particles' orbits, the gas slows the particle until its relative kinetic energy falls below the "capture energy" of the core, allowing for accretion. To be accreted, the particle must move slowly enough that the work done by gas drag in an in-falling orbit exceeds the relative kinetic energy of the particle. If the work done by the gas during this interaction is insufficient to remove all relative kinetic energy from the particle, the particle will escape from the core unaccreted.

On the other hand, if $R_{\rm stab} < R_{\rm Bondi}$, the situation is reversed. The gas flow dominates the dynamics of a particle orbitting at R_{stab}, complicating the picture. If the work done on a particle by gas drag is greater than the relative kinetic energy of the particle, the particle comes to rest with respect to the gas. This causes the particle to follow the gas flow, never entering the planetesimal's atmosphere, and avoiding accretion. On the other hand, if the work done by the gas is less than the relative kinetic energy of the particle, the particle maintains a velocity relative to the gas. This allows the particle to maintain a collision trajectory, being accreted even though it is never

fully stopped by the gas surrounding the core.

By covering both of these accretionary regimes, our model calculates collision cross sections, relative velocities, and growth times for a wide range of both orbiting particle and planetesimal core sizes. We apply this pebble accretion model, alongside our disk evolution model to understand each aspect of planetary formation in the first two chapters of this thesis. Just as pebble accretion allows us to model the supply of small particles to planetesimals, flow and pebble isolation help us model the final masses which solid planetesimals may reach by the time that their gaseous disks evaporate, halting the potential for future growth through pebble isolation.

1.3 Supernova Study

In addition to studying the earliest moments of a planet's life, I also study the final moments of a star's. Depending on a stars final mass, it may end as a supernova. Type Iax supernovae are a particular subclass of supernova, similar to the very common Type Ia supernova (Wang et al. 2013; Jha 2017). I designed, built, and used a statistical model to estimate the ages of several stars which would go on to explode as Type Iax supernovae. Using this model, I fit multi-band Hubble Space Telescope (HST) observations to theoretical models of stars of known ages. Because stars are thought to generally form in clusters from large clouds of gas, they tend to have similar ages to their neighbors. This age similarity allows one to estimate the ages of the group of stars in the local region in order to generate a statistical estimate for the age of the star when it exploded as a supernova. By performing this procedure for 9 supernovae

observed with HST, my co-authors and I define a probability distribution for age of a Type Iax progenitor star. This allows us to make statistically informed statements about the formation channel for these supernovae, giving strong evidence for one particular model.

1.4 Outline of this work

In Chapter 2, we present our disk evolution model, which we use to understand the growth of small particles in protoplanetary disks, as well as the growth of planetesimals via these small particles. Chapter 3 continues by applying the pebble accretion model to new parameter ranges, to explore the role that gas can play in speeding up the growth of solids up to and beyond the meter-scale-barrier. Finally, in Chapter 4, we present an earlier work which focuses instead on the deaths of stars though supernovae. We develop and use a statistical model to estimate the final ages of stars which go on to explode as Type Iax supernovae.

Chapter 2

Pebble Accretion in Drift Dominated Disks

2.1 Introduction

In this chapter, we apply both our state-of-the-art pebble accretion model and the flow isolation mass scale with our model for drift-dominated disks to make predictions for planetary demographics in the outer disk. We will determine the limiting solid planet masses that can be produced by rapid pebble accretion in the drift-limited outer regions of protoplanetary disks as a function of stellar mass, stellocentric distance, and the level of nebular turbulence. We will evaluate the sensitivity of these results to the initial sizes of seed planetesimals, showing typical growth times for a wide range of planetesimal sizes. In section 2.2, we go over the models which we use for pebble accretion, flow isolation, and to evolve our drift-dominated protoplanetary disk. In

section 2.2.2, we combine our models for flow isolation and the drift-limited maximum particle size in a protoplanetary disk to derive the maximum size for solid planets as a function of basic disk parameters. In section 2.3, we apply our framework to seven example disks to show typical growth times for planetesimals within these disks. Additionally, we explore the dependence of the isolation mass and growth times on various key disk parameters. Lastly, in section 2.4, we summarize our results, present our conclusions, and discuss pathways for future work.

2.2 Pebble Accretion in Drift Dominated Disks

2.2.1 Flow Isolation Mass

The various pebble accretion studies (e.g. Ormel & Klahr 2010; Lambrechts & Johansen 2012; Rosenthal et al. 2018) generally agree on at least one conclusion: that protoplanets can accrete pebbles on extremely rapid timescales. Once cores reach masses $\gtrsim 10^{-3} M_{\oplus}$, their cross section for accretion balloons, allowing pebbles to be accreted at impact parameters up to a body's Hill radius, given by $R_H = a(M_p/3M_*)^{1/3}$, where a is the semi-major axis of the protoplanet. Growth by pebble accretion is thus substantially faster than "traditional" growth processes, which rely solely on gravitational interactions to increase the cross section of a growing planet past its physical radius.

As described in Rosenthal & Murray-Clay (2020), proto-planetary growth via pebble accretion is so rapid that, without another process to shut off growth, all planets which reach the minimum mass to grow through pebble accretion (around $10^{-4} M_{\oplus}$) could be expected to grow to gas giants (an issue also highlighted by Lee & Chiang 2016).

Demographic studies of exoplanets do not find this ubiquity of gas giants. Rather, many studies (e.g. Borucki et al. 2010; Batalha et al. 2013; Fressin et al. 2013; Petigura et al. 2013; Zhu et al. 2018) find that Super-Earths and Sub-Neptunes are the most common class of observed exoplanets (at least in the regions where current detection methods are sensitive to small planets). If pebble accretion is as effective at growing planets as prior works have indiciated, we must appeal to a natural mass scale at which growth shuts off, leaving a majority of proto-planetary cores small enough to form Super-Earths.

One example of a limiting mass scale for pebble accretion is the "flow isolation" mass outlined in Rosenthal & Murray-Clay (2020). The dynamical interactions between a proto-atmosphere and the protoplanetary disk can cause the gaseous component of the disk to flow around the proto-atmosphere, rather than penetrating into it (Ormel & Kobayashi 2012). As explained in Section 1.2, particles which are completely coupled to the gas ($St \ll 1$) will follow the local gas flow (Picogna et al. 2018). Thus, the same interactions which cause the gaseous disk to flow around a proto-atmosphere will also cause strongly coupled particles to flow around the proto-atmosphere. If the largest particles which are available for pebble accretion (i.e. not other planetesimals in the disk) are all small enough that they are strongly coupled to the gas and flow around a planetesimal, the planetesimal will halt growth from accreting pebbles.

Another example of a limiting mass scale for pebble accretion is the "Pebble Isolation" mass (Bitsch et al. 2018). Much like the flow isolation mass, the pebble isolation mass relies on gas dynamics in the disk to isolate planetesimals from the pebble which they would otherwise utilize to rapidly grow. However, where flow isolation relies

on the creation of an over-density in the gas surrounding the planetesimal (a proto-atmosphere), the pebble isolation model instead relies on these planetesimals inducing a pressure bump in the gaseous disk, trapping sufficiently small particles, and preventing them from reaching the planetary core (Kanagawa et al. 2018). In Rosenthal & Murray-Clay (2020), the authors demonstrate that the flow isolation mass is of order the pebble isolation mass, but that the flow isolation mass is nearly always smaller than the pebble isolation mass. For this reason, in this study we will focus on the flow isolation mass as our limiting mass scale.

We would naturally expect a protoplanetary disk to have a maximum particle size available, either from drift, fragmentation, erosion, or elsewise (Kusaka et al. 1970; Weidenschilling 1984; Beckwith et al. 2000; Testi et al. 2014). When this maximum particle size is sufficiently small ($St \ll 1$), gas dynamics in the disk will flow isolate the planetesimals, shutting off growth with pebble accretion. Flow isolation occurs because small particles are so strongly slowed by gas drag that they quickly lose their entire kinetic energy relative to the gas. These particles, which are at rest relative to the gas, will follow the gas flow through the disk.

As a planetesimal grows by colliding with solids in the disk, it will also accrete a proto-atmosphere from the gaseous component of the disk (Piso & Youdin 2014), as mentioned in Chapter 1. Within this proto-atmosphere, the gas is essentially stationary with respect to the planetesimal. This static atmosphere causes the nebular gas to flow around the planetesimal and atmosphere. As small particles ($St \ll 1$) follow the flows of the nebular gas, this can prevent these particles from penetrating the budding

atmosphere, halting pebble accretion. Typically with pebble accretion, we think of gas interactions as aiding the growth of planetesimals, primarily by increasing cross sections for interactions with small particles. However, in this case the gas drag actually slows accretion, by preventing particles from getting close enough to be accreted.

To estimate this flow isolation mass, we find the core mass for which $R_{\rm Bondi} = R_{\rm stab}$ for the largest particles in the disk. This tells us the maximum mass a planetesimal core can reach before the largest particles it can accrete from the disk are too small to maintain their momentum relative to the gas. If this maximum impact parameter ($R_{\rm stab}$) is smaller than the scale height of the proto-atmosphere ($R_{\rm Bondi}$), we say that the planetesimal is flow isolated. Assuming a maximum dimensionless particle size $St_{\rm max}$, and examining each regime for $R_{\rm stab}$, we find the following expression for the flow isolation mass (equation 30 from Rosenthal & Murray-Clay 2020):

$$M_{\rm flow} = M_* \left(\frac{H}{a}\right)^3 \min\left[\frac{c_s}{v_{\rm gas}} St_{\rm max}, \sqrt{St_{\rm max}}, \frac{1}{\sqrt{3}}\right] \tag{2.1}$$

where M_* is the stellar mass, H is the scale height of the gas disk, a is the orbital distance of the planetesimal, and v_{gas} is the RMS velocity of the gas relative to the local Keplerian velocity. The three regimes shown here are when the minimum orbital radius is set by the wind-shearing radius (Perets & Murray-Clay 2011), the orbital shearing radius, and the Hill radius respectively.

As we see in equation 2.1, the flow isolation mass strongly depends on the maximum particle size (parameterized as $St_{\rm max}$) available in the disk. To determine this maximum particle size, we carefully model the growth and dynamics of the solid

particles in these disks as they evolve.

2.2.2 Disk Evolution

As the disk evolves, it passes through several different phases as the particles grow and drift. Particles drift in protoplanetary disks due to the same physics which makes pebble accretion possible. The sub-Keplerian rotation rate of the gaseous component of the disk imparts a headwind on the embedded particles. This headwind from the gas robs the particles of their angular momentum, and causes them to drift radially inward. Particles with a Stokes number of unity are the fastest drifters (Weidenschilling 1977) and, for the particle sizes probed by observations of the outer regions of protoplanetary disks, large particles drift inwards faster than smaller particles. Particles that are sufficiently small have their momentum so rapidly dissipated that they are essentially always at rest with respect to the gas. This prevents the particles from drifting inwards towards the host star, as the gas is no longer able to slow the particles, and decrease their angular momentum (Brauer et al. 2007; Morbidelli & Nesvorny 2012). Thus, the smallest particles must first grow before they are able to drift inwards .

We develop our disk evolution modeling by extending the work of Lambrechts & Johansen (2014) and Powell et al. (2019). Each of these studies model the growth and dynamics of solid bodies in protoplanetary disks, estimating the solid surface density in disks for a given solid particle size. They then can apply a particle size distribution, to model the full solid particle surface density. While these two works share a common goal, they differ somewhat in how they get there. Each calculates a maximum particle size in the disk, then uses this information to generate the solid surface density. They

also share the assumption that the maximum sized particles are those for which the growth and drift times are equal. Below this maximum size, particles grow more rapidly than they drift, growing to larger sizes before they are destroyed, while above this size, particles drift more rapidly than they grow, being destroyed before they can finish growing. Where these two models differ is in their final assumption. In Lambrechts & Johansen (2014), the authors assume that the largest particles are supplied by drift, thus requiring mass continuity across disk annuli. The authors of Powell et al. (2019) on the other hand, assume that these largest particles are instead supplied by local growth. This assumption manifests as a requirement that the drift and growth times not only match each other, but that they also match the current age of the disk. These two different final assumptions give different results for maximum particle sizes and solid surface densities. In this chapter, we expand upon and combine the two models, showing that disks can transition smoothly from one to the other as they evolve.

Both Lambrechts & Johansen (2014) and Powell et al. (2019) describe the time that a particle spends growing to a size at which it begins to drift. Each of these studies implicitly assume that the particles in a protoplanetary disk are initially smaller than the minimum size for drift. Thus, there is a delay time during which the particles grow from their initially small size to the size at which drift begins. Powell et al. (2019) calls this the "early growth time" (see their Appendix B). Lambrechts & Johansen (2014) instead discuss a "pebble front", which moves outward from the star to the outer edge of the disk over time. The pebble front describes the point at which particles have had long enough to grow that they are just now large enough to begin drifting. We employ

the pebble front framework in this chapter, as a useful way to delineate the relevant regimes of the disk's evolution.

Using this pebble front location information, we identify three relevant timescales. First, we have the time at which the pebble front passes a particle's current location in the disk, which we call $t_{\mathrm{PF}}(a)$. At this time particle drift dominates solid body growth, and pebble accretion becomes efficient. This peak in efficiency occurs because the largest particles see their peak in size at this time, giving quick growth times and high flow isolation masses. This efficient growth is contingent on having large enough planetesimal cores, which may be the result of rare favorable growth, or of cores being scattered from other parts of the disk. This efficient growth period continues as the pebble front moves outwards, keeping the particle supply drift dominated, allowing the disk to be well modeled with a constant $\dot{M}$.

Next, we have the time at which the locally grown pebbles exceed the supply of pebbles drifted in from the pebble front. To determine this time, we compare these mass fluxes throughout the disk, normalized for the growth annulus area. When the local, growth supplied $\dot{M}/Area$ first exceeds the global, drift supplied $\dot{M}/Area$, the disk begins to transition from the regime described by Lambrechts & Johansen (2014) to the regime described by Powell et al. (2019). We call this time $t_{\mathrm{Transition}}$. The location of the pebble front at this time defines a sort of disk edge, from which the pebble front "bounces back" inwards. The bouncing back pebble front's inner edge is defined as the location to which a maximally sized particle drifts from the disk edge in the time since $t_{\mathrm{Transition}}$. The final important timescale is when the pebble front bounces back

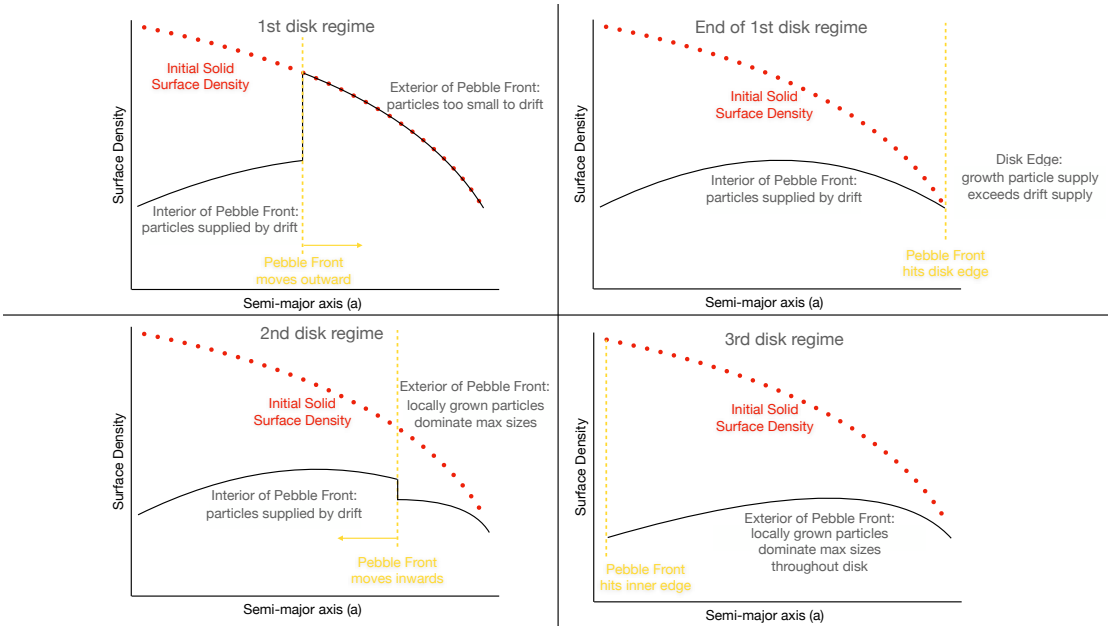

Figure 2.1: A diagram describing the surface density evolution through the three disk regimes.

from the outer edge of the disk and arrives at the inner edge of the disk, which we will call t_{PFBB}. From this, we see 3 growth regimes in our protoplanetary disks: when $t_{\mathrm{PF}}(a) < t_{\mathrm{disk}} < t_{\mathrm{Transition}}$, when $t_{\mathrm{Transition}}) < t_{\mathrm{disk}} < t_{\mathrm{PFBB}}$, and when $t_{\mathrm{disk}} > t_{\mathrm{PFBB}}$. Each of these disk regimes is illustrated in Figure 2.2.2.

Before the beginning of the first regime, particles throughout the disk are too small to drift (Dominik et al. 2007). During this time, particles grow due to collisions induced by random thermal motion. This is a much slower type of growth than the growth via pebble accretion, as particles are only able to collide with their nearby neighbors. For the purpose of this study, we think of this as a sort of "burn in" period, during which no major planetary growth occurs.

Once the pebble front passes the particle's location in the disk at time $t_{\mathrm{PF}}(a)$, our first disk regime begins (shown in the first panel of Figure 2.2.2). As the pebble

front is now exterior to the particle's location in the disk, new particles are constantly drifting inwards past our particle's location. In this window of time, we mostly apply the method from Lambrechts & Johansen (2014), though we expand their work to apply to a larger range of turbulence levels and disk ages. We analytically solve for the surface density, maximum particle size, and maximum stokes number in the Epstein drag law regimes, for both a low turbulence (laminar dominated relative velocity) and a high turbulence (turbulent dominated relative velocity) regime. These formulae come to us by combining two constraints: the requirement that the maximally sized particle have equal growth and drift times, and the requirement of disk surface density continuity (equation 15 in Lambrechts & Johansen (2014)). First, we present the low turbulence regime. The maximum particle size $s_{\max}$ is

$$\begin{aligned} s_{\max} &= \sqrt{\frac{\pi}{8}} \left(\frac{3\Lambda \epsilon_p f_d}{8\delta} \right)^2 \frac{\Sigma_g}{\alpha \eta \rho_{int}} \\ St_{\max} &= \frac{\pi}{4} \left(\frac{3\Lambda \epsilon_p f_d}{8\delta} \right)^2 \frac{1}{\alpha \eta} \\ \Sigma_d &= \left(\frac{8}{3\Lambda \pi} \right)^2 \frac{\delta \alpha \dot{M} \Omega}{(\epsilon f_d v_k)^2} \end{aligned} \tag{2.2}$$

where Σ_d is the solid surface density, α is a measure of the turbulence strength (Shakura & Sunyaev 1973), ρ_{int} is the internal particle density, and Σ_g is the gaseous surface density.

Now, we have the high turbulence regime:

$$
\begin{aligned}
s_{\max} &= \left(\frac{3\Lambda\epsilon_p}{8\delta^2}\right)^{2/5}\left(\frac{1}{2\pi^7}\right)^{1/10}\frac{\Sigma_g^{3/5}\dot{M}^{2/5}\Omega^{2/5}}{\rho_{int}}\left(\frac{v_k}{c_s^2}\right)^{4/5} \\
St_{\max} &= \sqrt{\frac{\pi}{2}}\left(\frac{3\Lambda\epsilon_p}{8\delta^2}\right)^{2/5}\left(\frac{1}{2\pi^7}\right)^{1/10}\left(\frac{\dot{M}\Omega}{\Sigma_g}\right)^{2/5}\left(\frac{v_k}{c_s^2}\right)^{4/5} \\
\Sigma_d &= \left(\frac{8\delta}{3\epsilon_p}\right)^{2/5}\left(\frac{1}{3^2\pi^4}\right)^{1/5}\left(\dot{M}\Omega\right)^{3/5}\left(\frac{\Sigma_g}{c_s v_k^2}\right)^{2/5}
\end{aligned}
\tag{2.3}
$$

where v_{kep} is the core's Keplerian velocity, c_s is the sound speed in the gas, λ_{mfp} is the mean free path in the gas, and Ω is the core's orbital frequency.

Now, plugging in $\dot{M}$ (equation 14 from Lambrechts & Johansen 2014), we calculate the surface density as:

$$
\begin{aligned}
\Sigma_{\text{d}} &= \frac{2}{\sqrt{3}}\left(\frac{2}{3}\right)^{1/3}\pi^{-1/4}\sqrt{\frac{\Sigma_g}{v_{\text{kep}}a}}(GM_*)^{1/6}\sqrt{\Sigma_g}\epsilon_d^{1/3}f_d^{5/6}t^{-1/6} \\
&\approx 0.75\sqrt{\frac{\Sigma_g}{v_{\text{kep}}a}}(GM_*)^{1/6}\sqrt{\Sigma_g}\epsilon_d^{1/3}f_d^{5/6}t^{-1/6}
\end{aligned}
\tag{2.4}
$$

where M_* is the solar mass, ϵ_d is a dimensionless constant defining the sticking efficiency, here set to 0.5, and f_d is the initial dust to gas ratio, which we set as 10^{-2} for the extent of this thesis.

Next, the 2nd regime begins when the local growth of pebbles exceeds the supply of pebbles drifted from the pebble front. This is when $t_{\text{Transition}}) < t_{\text{disk}} < t_{\text{PFBB}}$ (shown in the 2nd panel of Figure 2.2.2). The largest particles are now grown locally rather than drifted in, giving us a new particle size and surface density in the outer regions of the disk. In these regions, the model presented in Powell et al. (2017) applies.

This transition is not immediate throughout the disk, as it takes time for the inner regions of the disk to feel this change that begins at the pebble front. We model this transition between particle regimes by tracking the drifting position of the maximally sized particle at the edge of the disk when $t_{\rm disk} = t_{\rm PF}(a_{\rm max})$ (see the 3rd panel of Figure 2.2.2). We use this particle's radial position in the disk to demarcate the barrier outside of which the maximum particle size has further decreased. Inside of this barrier, the maximum particle size is determined by the model based on Lambrechts & Johansen (2014), while outside of the it, the particle size is set by the model of Powell et al. (2017). When this particle arrives at the inner edge of the disk, we say that the pebble front has "bounced back", and a smaller maximum particle size (determined by the model in Powell et al. (2017)) is present throughout the disk. This marks the end of the 2nd regime.

The 3rd regime begins when the "bouncing back" pebble front reaches the inner edge of the protoplanetary disk, when $t_{\rm disk} > t_{\rm PFBB}$ (illustrated in the 4th panel of Figure 2.2.2). At this time, the particles throughout the disk which drift by our growing planetary seed originate in the outer edges of the protoplanetary disk. In this regime, the model presented in Powell et al. (2017) is valid, and we can use the order-of-magnitude assumption that $t_{\rm drift} = t_{\rm growth} = t_{\rm disk}$ throughout the disk. In figure 2.2.2, we present another cartoon to illustrate when and where each disk regime is active.

The specifics of which regime is the dominant phase of planet formation depends on the time at which plantesimals large enough to undergo pebble accretion form in the disk, the radial extent of the protoplanetary disk which we are considering, and

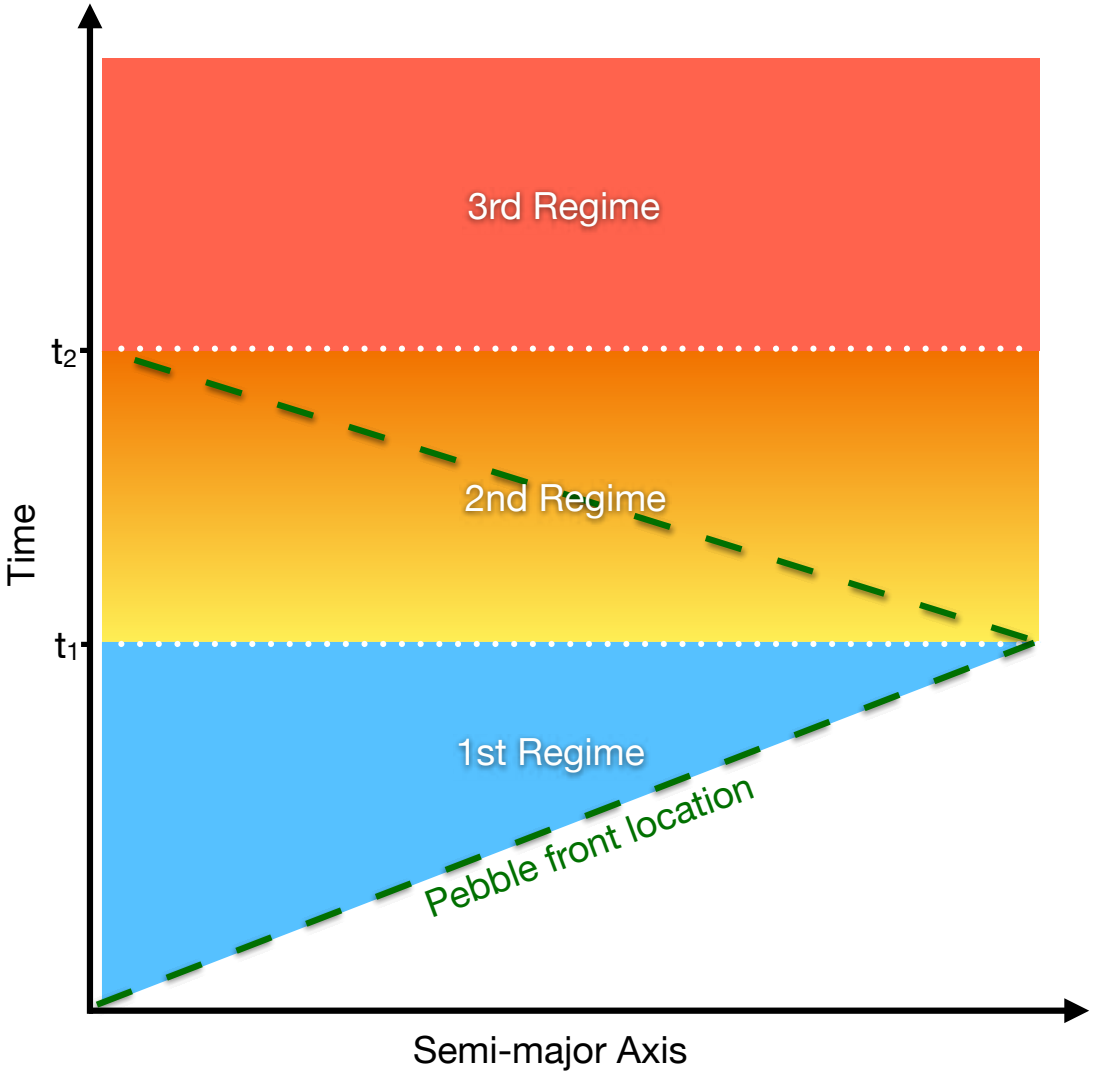

Figure 2.2: Another diagram of the three disk regimes, and when they apply. The disk transitions from the first regime (shown in blue) to the second regime (shown in orange and red) when the locally grown particle supply exceeds the particle supply drifted in from the pebble front. The third regime (shown in red) begins when the pebble front fully "bounces back" from the edge of the disk.

lastly the overall solid surface density of the disk. The question of when planetesimals form is certainly a challenging one, and one which we do not aim to answer with this study (though there are some paths forward here, including the rare occurences of rapid growth described in Chapter 3, and the streaming instability (e.g. Youdin & Goodman 2005; Johansen et al. 2007)). Instead, we will treat this time, $t_{\rm planetesimal}$ as a free parameter in our model. By and large, we would expect planets to grow in the 1st regime for disks with large radial extent, and in the 2nd or 3rd regime for small disks. This occurs because the radial extent of the disk determines how long it spends in the 1st regime, as opposed to the 2nd and the 3rd. For this reason, we will present the results of this study for the 1st, 2nd and 3rd regimes, to remain agnostic as to the specific conditions which govern planetary growth.

As the disk evolves, and more and more pebbles are able to grow large enough to drift inwards, the disk slowly loses solid mass, thanks to particles drifting into the host star. By the end of the 1st regime, when $t_{\rm disk} = t_{\rm PF}(a_{\rm max})$, the disk's solid surface density has already significantly decreased from its initial value, particularly in the inner disk. The protoplanetary disk TW Hydra's evolving surface density is shown in figure 2.2.2. The solid surface density continues to rapidly decrease in the 2nd and 3rd regimes, leading to significantly longer growth times for planetesimals, as compared to the 1st regime.

We model the transition between these disk regimes by tracking the relative growth rates of particles when they grow via interactions with particles drifting inwards from the pebble front, as compared to when they grow from interactions with particles

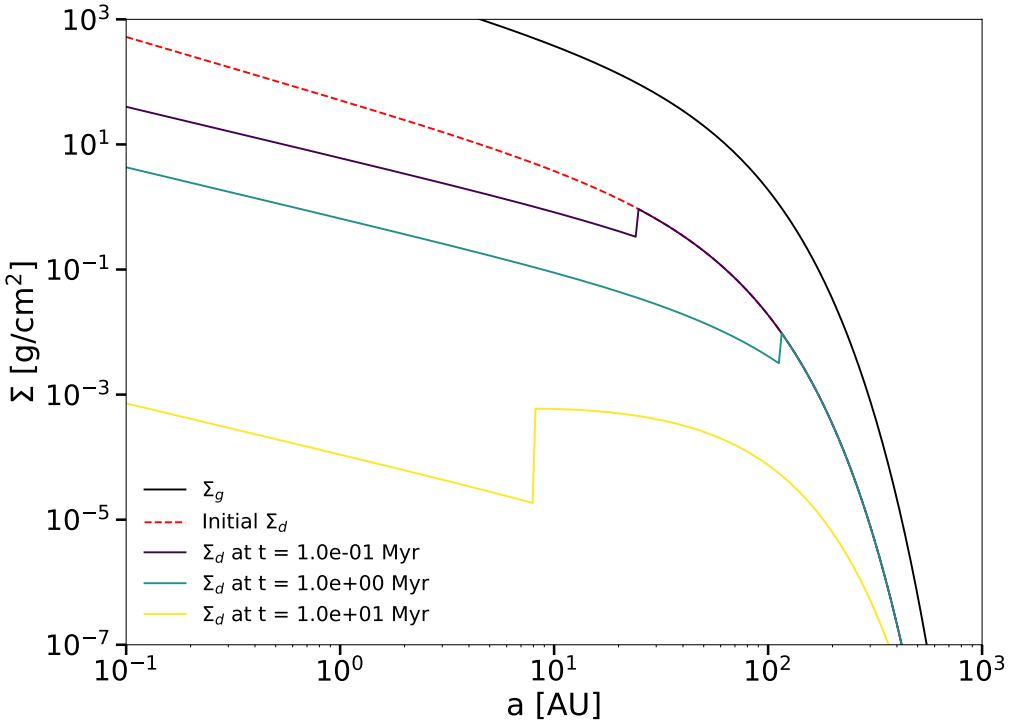

Figure 2.3: The surface density of the disk TW Hydra as a function of time. The gaseous surface density is shown as a solid black line, and the initial solid surface density is shown as a dashed red line. The evolved solid surface density is then plotted for several times as the solid colored lines. As the disk ages, it passes from the 1st regime (as described in Lambrechts & Johansen 2014) to the 2nd and eventually 3rd regimes (as described in Powell et al. 2017).

grown in their local region. To make this comparison, we examine the growth rate per area in the evolving disk, noting where and when locally grown particles first exceed the supply of drifting particles. This is shown in figure 2.2.2. We also present the TW Hydra surface density, zoomed in on the ages and locations nearest the disk transition, to highlight the changing surface density across the transition, in Figure 2.2.2.

We present this comparison between growth rates across regimes in another way below, by defining a "growth efficiency". To accomplish this, we determine a typical time for a planetesimal to grow from the minimum mass necessary for pebble accretion to the flow isolation mass. We measure this time in each regime, then compare these characteristic timescales to the lifetime of each regime. The lifetimes of each regime can be described as $t_{\mathrm{1ndRegime}} = t_{\mathrm{PF}}(a_{\mathrm{max}}) - t_{\mathrm{PF}}(a)$, $t_{\mathrm{2ndRegime}} = t_{\mathrm{PFBB}} - t_{\mathrm{PF}}(a_{\mathrm{max}})$, and $t_{\mathrm{3rdRegime}} = t_{\mathrm{DiskLifetime}} - t_{\mathrm{PFBB}}$). We then divide each regime's lifetime by the typical planetesimal growth time in that regime, so that we can compare this "growth efficiency" between disk regimes. We present the results of this calculation in figure 2.2.2.

This growth efficiency peaks in the disk's first regime, though it steadily declines over time. Once the 2nd regime begins, the efficiency rapidly falls in the outer regions, as the Powell et al. (2019) regime takes over. The pebble front eventually hits the inner edge, and the disk transitions to the 3rd regime, with efficiency falling throughout the disk.

2.2.3 Pebble front evolution

To better understand how our disks' surface densities evolve, we examine the evolution of the pebble front. We compare the timescale on which the pebble front

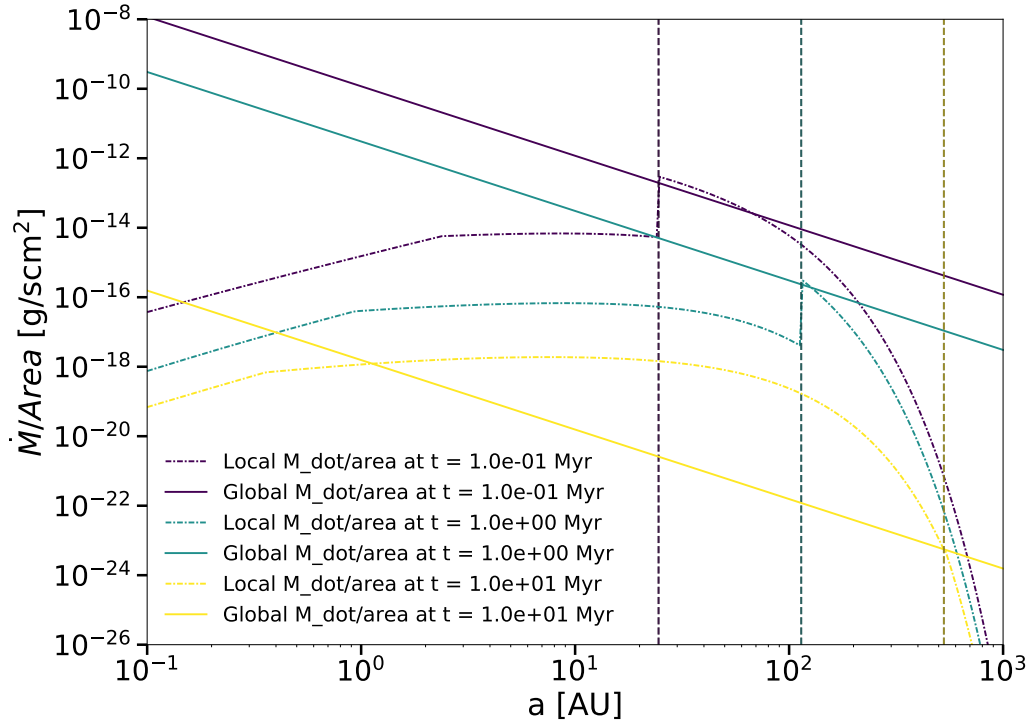

Figure 2.4: The $\dot{M}$ per area of the disk TW Hydra as a function of time. As the disk ages, the locally grown $\dot{M}$ per area increases, until it eventually exceeds the particle supply drifting inwards from the pebble front. At this point, the disk transitions from the 1st regime (as described in Lambrechts & Johansen 2014) to the 2nd and eventually 3rd regimes (as described in Powell et al. 2017). In this figure, we can see this as the dashed and dotted yellow line exceeding the solid yellow line. Remember that this $\dot{M}$ comparison only applies within the pebble front, the location of which is shown in vertical dashed lines.

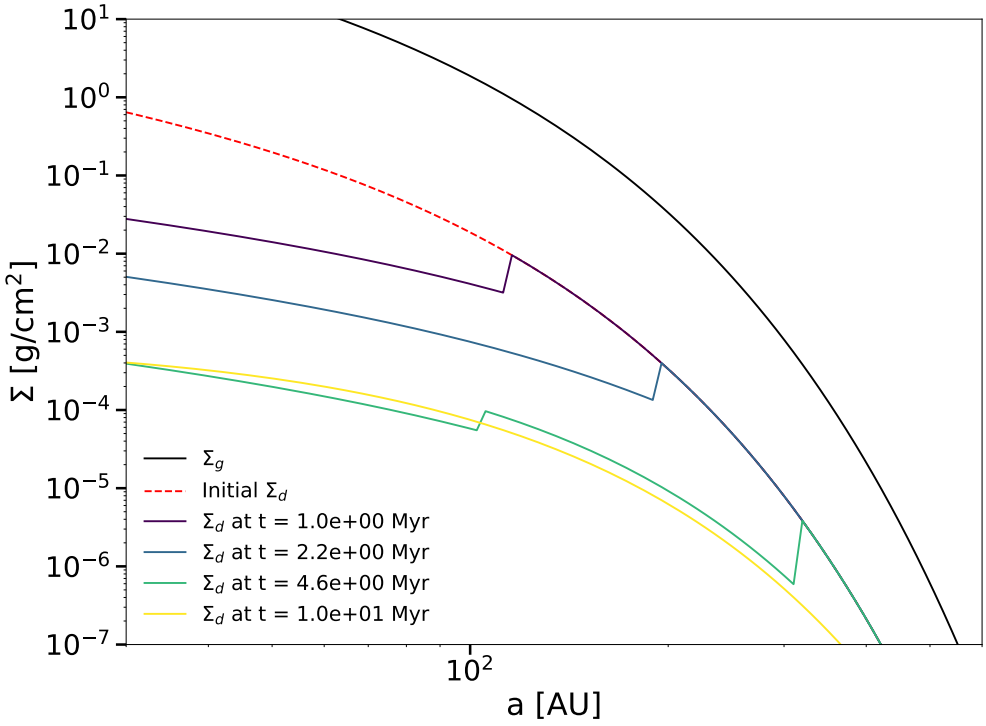

Figure 2.5: The surface density of the disk TW Hydra, again as a function of time. Here, we zoom in on a few disk ages, near the transition time between disk regimes, in order to focus on the behavior of the pebble front during this time. The first two disk ages show the disk in the 1st regime, as the pebble front drifts outward. The third age shows the disk in the 2nd regime, with the Powell et al. 2017 model applying from the inner region out towards the location of the inward drifting pebble front, and the Lambrechts & Johansen 2014 model applying from this inner edge, out to the location of the outer pebble front at the time of the transition. Lastly, the fourth age shows the disk in the 3rd regime, where the Powell et al. 2017 model applies to the entire region shown.

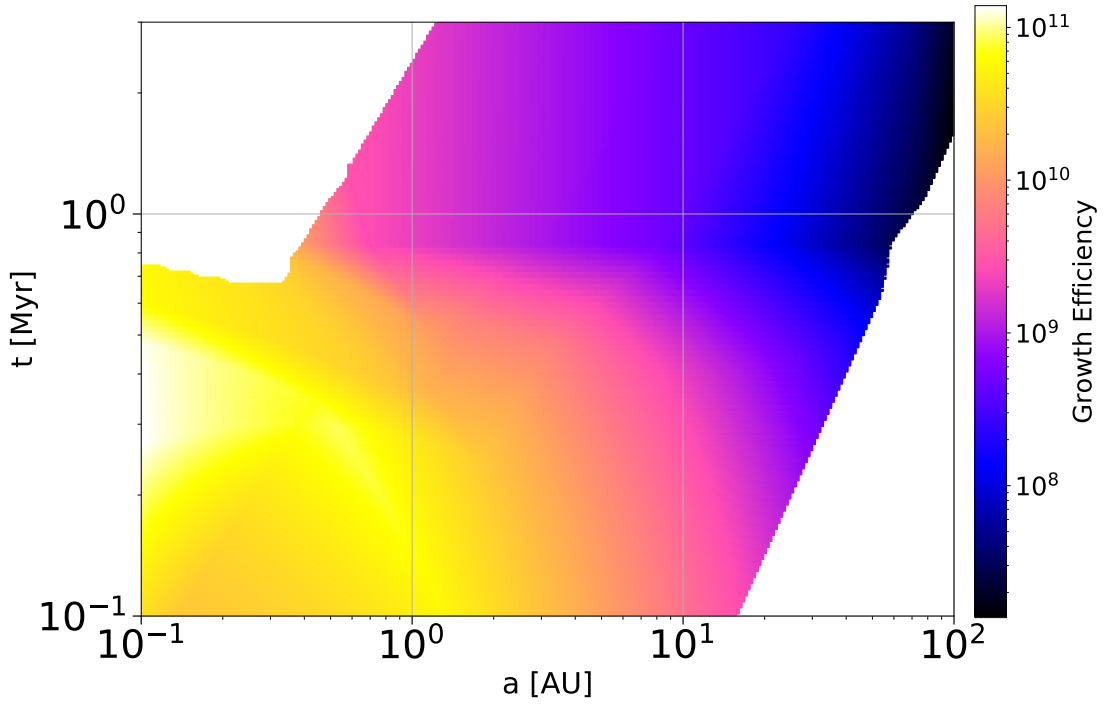

Figure 2.6: The ratio of disk lifetime to growth time from minimum mass to flow isolation mass, named Growth Efficiency, as a function of both semi-major axis, and disk age. Note the drop upon transitioning from the 1st regime to the 2nd and 3rd.

evolves, $t_{\rm PF,evo}$, to the drift time for the maximally sized particles in the disk, $t_{\rm drift}$. First, we evaluate the evolution of the pebble front. Lambrechts & Johansen (2014) present the pebble front location in their equation 10, which they calculate by equating the time a particle needs to grow before it can drift to the age of the disk. In this calculation, they assume an Epstein drag law, while we allow for a variety of drag laws in order to cover a wide range of particle sizes. While increased complexity allows for an exact calculation of the pebble front location, it makes an analytic form impossible. Fortunately, for the disks and times presented in this study, the analytic approximate form from Lambrechts & Johansen (2014) is accurate to about 1% (Garaud 2007). For this reason, we can use the approximate version of the pebble front location for this calculation of the pebble front evolution:

$$\begin{aligned} a_{PF} &= \left(\frac{3}{16}\right)^{1/3} (GM_*)^{1/3} (\epsilon_d f_d)^{2/3} t_{\rm disk}^{2/3} \\ \dot{a}_{PF} &= \frac{2}{3}\frac{a_{PF}}{t_{\rm disk}} \end{aligned} \tag{2.5}$$

where a_{PF} is the pebble front location, and $t_{\rm disk}$ is the disk age.

We define the timescale on which the pebble front evolves, $t_{\rm PF,evolution}$ as the ratio between the pebble front location and the speed at which the pebble front evolves outwards in the disk.

$$\begin{aligned} t_{\rm PF,evolution} &\approx \frac{a_{\rm PF}}{\dot{a_{\rm PF}}} \\ &\approx \frac{3}{2} t_{\rm disk} \end{aligned} \tag{2.6}$$

This shows us that the pebble front evolves on roughly the same timescale as the age of the protoplanetary disk.

Next, we estimate the drift time for maximally sized particles, as in Powell et al. (2017) and Chiang & Youdin (2010). Here, we calculate this drift time for the largest particles with stokes number $St_{\max}$.

$$\begin{aligned} t_{\text{drift}} &\approx \frac{a}{\dot{a}} \\ &\approx \frac{a}{2\eta v_{\text{kep}}} \frac{1 + St_{\max}^2}{St_{\max}} \\ &\approx \frac{a}{2\eta v_{\text{kep}} St_{\max}} \end{aligned} \tag{2.7}$$

where t_{drift} is the drift time, and η is a dimensionless measure of the pressure profile of the disk.

Now, employing the disk's maximum particle size in the 1st regime (when the pebble front has not yet reached the outer edge of the disk):

$$s_{\max} \approx \frac{3\sqrt{2}\Sigma_d}{16\eta\rho_{\text{int}}} \tag{2.8}$$

This maximum particle size is then used to calculate the associated maximum stokes number. If we assume that the maximum particle size is in the Epstein drag regime, we can derive the following analytic form for the maximum stokes number, as in equa-

tion **??**.

$$St_{\max} \approx \frac{3\sqrt{\pi}\epsilon_p \Sigma_d}{16\eta\Sigma_g} \tag{2.9}$$

where ϵ_p is a dimensionless measure of the coagulation efficiency of pebbles. We can then plug this approximate maximum stokes number into our equation for the drift time:

$$\begin{aligned} t_{\text{drift}} &\approx \frac{a}{2\eta v_{\text{kep}}} \frac{16\eta\Sigma_g}{3\sqrt{2}\epsilon_p\Sigma_d} \\ t_{\text{drift}} &\approx \left(\frac{2^{1/2}3^{1/4}}{\epsilon_p^{1/2}}\right) f_d^{1/2} \sqrt{\frac{t_{\text{disk}}}{\Omega}} \end{aligned} \tag{2.10}$$

Finally, we compare this drift time to the pebble front evolution time:

$$\begin{aligned} \frac{t_{\text{drift}}}{t_{\text{PF,evolution}}} &\approx \left(\frac{2^{1/2}3^{1/4}}{\epsilon_p^{1/2}}\right) f_d^{1/2} \sqrt{\frac{t_{\text{disk}}}{\Omega}} \frac{2}{3t_{\text{disk}}} \\ &\approx \sqrt{\frac{2\epsilon_d}{3\epsilon_p}} \\ \frac{t_{\text{drift}}}{t_{\text{PF,evolution}}} &\approx 0.26 \end{aligned} \tag{2.11}$$

Using reasonable assumptions about our disk parameters ($\epsilon_d = 0.05$, and $\epsilon_p = 0.5$), we find that the pebble front evolves on the same timescale as the largest particles drift. This is as expected, as the pebble front is the location where particles first grow large enough to drift. It is not surprising then, that this front evolves at the same rate as the drifting particles.

In the first disk regime, where the method modeled after Lambrechts & Johansen (2014) applies, it is assumed that the dust mass in a given annulus is set by drift from the annulus exterior. This assumption, of a "drift driven disk", is borne out by our calculation above. By demonstrating that the pebble front evolves on the same time-scale as the particles drift, we show that particles drifting from the pebble front can drive the disk's solid surface density, as long as the $\dot{M}_{\rm drift}$ exceeds the $\dot{M}_{\rm growth}$.

2.2.4 Model of Drift Dominated Outer Disk

In the drift-dominated regime, the outer-most locations of particles in disks can be constrained with multiwavelength observations of protoplanetary disks. These observations of disks in the millimeter can probe particle drift, and thus be used to infer the aerodynamic properties of the particles present in the disk. Using these observations, Powell et al. (2017, 2019) created a new method of determining the surface densities of protoplanetary disks, without assuming a tracer-to-H2 ratio. This method allows one to empirically infer many fundamental disk parameters, including the Stokes number of the maximum particle size as a function of disk semi-major axis. The model has already been applied to 7 disks thus far and has been able to reconcile the theory of particle evolution in protoplanetary disks with observations (Powell et al. 2019).

In order to determine the locations within disks, and the disk parameters which will lead to drift domination in protoplanetary disks, we apply the following method. First, as in both Lambrechts & Johansen (2014) and Powell et al. (2017), we set $t_{\rm drift} = t_{\rm grow}$, to determine the maximum size to which particles can grow before they drift. We then compare this maximum particle size to the particle size limit

from fragmentation processes, as described in Birnstiel et al. (2012), equation 8. If our maximum particle size exceeds the size limit from fragmentation, then we say that these particles are fragmentation limited, rather than drift limited.

This size limit from fragmentation in Birnstiel et al. (2012) is parameterized in terms of a fragmentation velocity, the velocity limit above which particle collisions lead to fragmentation rather than growth. The specifics of particle fragmentation are still uncertain, but there is general agreement that this particle fragmentation velocity is in the range of $1\frac{m}{s}$ to $50\frac{m}{s}$, depending on the particle size, density, composition, and other factors (e.g. Housen & Holsapple 1990, 1999; Stewart & Leinhardt 2009; Beitz et al. 2011).

In figure 2.2.4, we model drift and fragmentation in the disk DR Tau to find the region over which the disk is drift-dominated, and hence our model is applicable. To accomplish this, we calculate the maximum particle size in the disk as set by drift by finding the particle size which drift into the star at the same rate that it grows. We then compare this particle size to the particle size limit imposed by fragmentation, using the same methods as Birnstiel et al. (2012). When the drift limited size exceeds the fragmentation limited size, we call the disk "drift-dominated", and can confidently apply our model. For this figure, we use four different assumed fragmentation velocities, $v_{\text{frag}} = 1\frac{m}{s}$ (blue dotted line), $v_{\text{frag}} = 3\frac{m}{s}$ (green solid line), $v_{\text{frag}} = 10\frac{m}{s}$ (purple dotted line), and $v_{\text{frag}} = 30\frac{m}{s}$ (turquoise dotted line) which give us the inner boundaries of our drift dominated disk at approximately 167 AU, 22 AU, 3.5 AU, and 0.7 AU respectively. Note however, that this thesis focuses on the outer disk, so we don't consider inwards

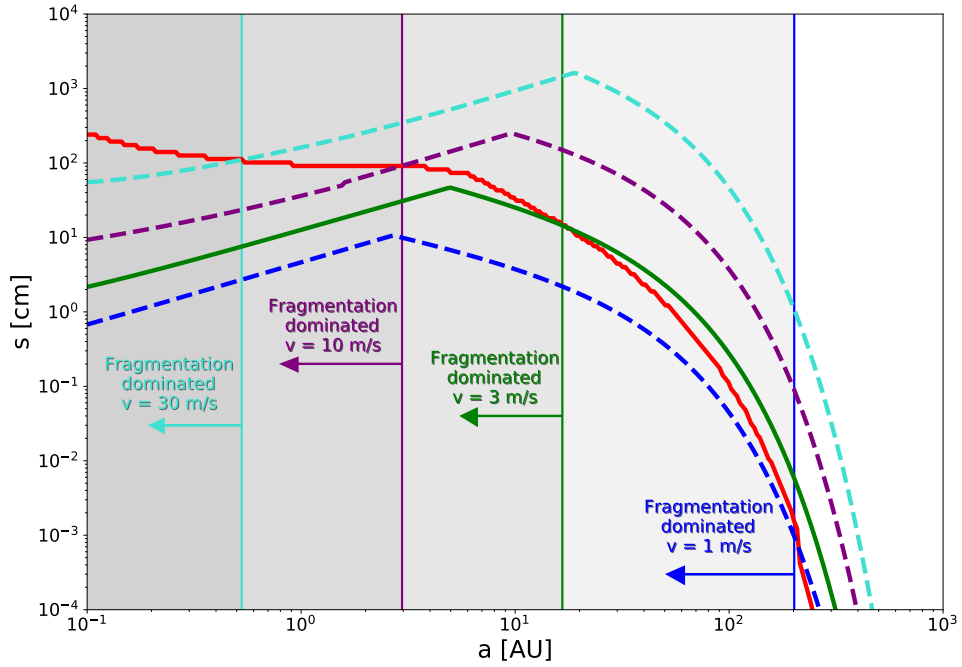

Figure 2.7: The maximum particle size in the protoplanetary disk TW Hydra as set by both fragmentation, and by particle drift. When the fragmentation limited size is greater than the drift limited size, we say that the disk is drift dominated, and our models are applicable. For this figure, we show our results for fragmentation velocities of $1\frac{m}{s}$ (blue dotted line), $3\frac{m}{s}$ (green solid line), $10\frac{m}{s}$ (purple dotted line), and $30\frac{m}{s}$ (turquoise dotted line).

of a few AU anyway.

2.2.5 Special Case of flow isolation

Here, we take our maximum particle size, previously presented in Section 2.2.2, and apply it to our formula for the flow isolation mass, to find the limiting mass scale, based only on disk parameters.

In the 1st regime described in Section 2.2.2, we assume only that $t_{\text{drift}} = t_{\text{grow}}$

to find the maximum particle size due to drift. Lambrechts & Johansen (2014) calculate this dominant particle size (see equation 20 of Lambrechts & Johansen 2014) to be:

$$St \approx \frac{\sqrt{3}}{8} \frac{\epsilon_p}{\eta} \frac{\Sigma_p}{\Sigma_g} \tag{2.12}$$

where ϵ_p is an order unity factor which describes the coagulation efficiency for pebbles. For this study, we assume $\epsilon_p = 0.5$. Plugging this maximum particle size into our expression for the flow isolation mass (Equation 2.1), we find:

$$M_{\rm flow} = M_* \left(\frac{H}{a}\right)^3 \min\left[\frac{\sqrt{3}}{8}\frac{\epsilon_p c_s \Sigma_p}{\eta v_0 \Sigma_g}, \frac{3^{1/4}}{2\sqrt{2}}\sqrt{\frac{\epsilon_p \Sigma_p}{\eta \Sigma_g}}, \frac{1}{\sqrt{3}}\right] \tag{2.13}$$

This formula for the flow isolation mass applies both in the 1st regime, and in the inner disk portion of the 2nd regime (where the pebble front has not yet bounced back).

If we are instead in the 3rd regime described in Section 2.2.2, we assume that the time that a particle has to drift is the same as the age of the disk. That is, $t_{\rm disk} = t_{\rm drift} \equiv |a/\dot{a}|$. Following the reasoning of Powell et al. (2017), we calculate the radial particle drift velocity as

$$\begin{aligned} \dot{a} &\approx -2\eta\Omega a \left(\frac{St}{1+St^2}\right) \\ &\approx -2\eta v_k \left(\frac{St}{1+St^2}\right) \end{aligned} \tag{2.14}$$

In a passively irradiated disk, $v_0 = \eta v_k$, where v_0 is the maximum particle drift velocity.

Our expression thus becomes

$$\begin{aligned} \dot{a} &\approx -2v_0 \left(\frac{St}{1+St^2} \right) \\ &\approx -2v_0 St \end{aligned} \tag{2.15}$$

where we assume $St \ll 1$ for the final line.

Finally, we apply the assumption that $t_{\text{disk}} = t_{\text{drift}} \equiv |a/\dot{a}|$. Combining this expression with equation 2.15 for $\dot{a}$ yields

$$St = \frac{a}{2t_{\text{disk}} v_0} \tag{2.16}$$

This equation and equation 2.12 give the maximum particle size (parameterized by Stokes number) in a drift-dominated disk as a function of semi-major axis, disk age, dust-to-gas ratio, and sub-Keplerian velocity. With this prescription, we know which particles are available for pebble accretion. Combining the maximum particle size from equation 2.16 with the flow isolation mass model of Rosenthal & Murray-Clay (2020) allows for the simple derivation of the maximum mass to which a solid planetesimal core can grow through pebble accretion:

$$M_{\text{flow}} = M_* \left(\frac{H}{a} \right)^3 \min \left[\frac{c_s a}{2t_{\text{disk}} v_0^2}, \sqrt{\frac{a}{2t_{\text{disk}} v_0}}, \frac{1}{\sqrt{3}} \right] \tag{2.17}$$

The 2nd regime described in Section 2.2.2 features each of these maximum particle sizes present in the disk simultaneously, with the particles exterior to the pebble front bouncing back to the inner disk being described by equation 2.16, while the

particles inside the returning pebble front are still set by equation 2.12.

2.3 Example Applications

2.3.1 Modeling real disks: 1st regime

Having introduced our method for determining maximum particle size in a protoplanetary disk, and the associated flow isolation mass to which we would expect planets to grow, we now step through the analysis process for several real disks. In this study, we examine the disks TW Hydra, Dr Tau, FT Tau, AS 209, HD 163296, CY Tau, and DoAr 25, all of which have multi-wavelength observations which we use to constrain the maximum particle size in these disks. Some important properties of the stars are listed in table 2.1.

For each disk in our sample, we model the time evolving solid surface density, along with the initial gas surface density. This information is presented in Figures 2.2.2, 2.3.1, 2.3.1, 2.3.1, 2.3.1, 2.3.1, and 2.3.1. We then apply our maximum particle size information (2.2.2 and **??**) to our pebble accretion code and flow isolation modeling to determine growth rates for potential planetesimals embeded in these disks. For each

Object	Stellar Mass ($M_\odot$)	Age (Myrs)	T_0 (K)	References
TW Hydra	0.8	5	82	Rhee et al. (2007), Qi et al. (2013)
DR Tau	0.8	1	121	Ricci et al. (2010), McClure (2019)
FT Tau	0.55	1.6	89	Ricci et al. (2010), McClure (2019)
AS 209	0.9	1.6	131	Herbig & Bell (1988)
HD 163296	2.3	5	284	Natta et al. (2004)
CY Tau	0.48	1	98	Bertout et al. (2007), McClure (2019)
DoAr 25	1	2	123	Andrews et al. (2008)

Table 2.1: The stellar properties of this chapters' sample.

disk, we present the growth times across planetesimal mass and semi-major axis for six different disk ages, to show the disk's evolution (Figures 2.3.1, 2.3.1, 2.3.1, 2.3.1, 2.3.1, 2.3.1, 2.3.1). In each of these disks, the growth times are so rapid in the 1st disk regime that we predict planetesimals to rapidly grow to their flow isolation masses as soon as they reach a minimum mass for traditional pebble accretion.

Of the seven disks in our sample, only two (TW Hydra and DR Tau) transition from the 1st disk regime to the 2nd and 3rd in the times tested in this chapter. We also present the growth and drift $\dot{M}/Area$ for each disk (Figures 2.2.2, 2.3.1, 2.3.1, 2.3.1, 2.3.1, 2.3.1, 2.3.1), to illustrate when and how certain disks transition, while others do not. The disks which do not transition maintain the possibility of efficiently growing planetesimals to their flow isolation mass throughout their lifetimes.

2.3.2 Model Parameters

1. Controlling parameters in flow isolation mass

   The parameters which enter into our equations for flow isolation mass (equations 2.13 and 2.17) can be reduced to the following: stellar mass M_*, disk temperature T, initial dust-to-gas ratio f_d, and of course the semi-major axis of our planetesimal (a) and the time since the disk's formation ($t_{\rm disk}$). Other parameters appear in our equations, but can be reduced down to these constituent pieces, including $H = \frac{c_s}{\Omega}$, $\eta \approx \frac{c_s^2}{2v_k^2}$, $c_s = \sqrt{\frac{k_B T}{\mu}}$, $v_0 = \eta v_k$, and $v_k = \sqrt{\frac{GM_*}{a}}$, where H is the scale height of the disk, k_B is the Boltzmann constant, and v_0 is the gas velocity. These fundamental parameters are listed for each object in our sample in Table 2.1. This chapter maintains an initial dust-to-gas ratio of 10^{-2}, as the authors

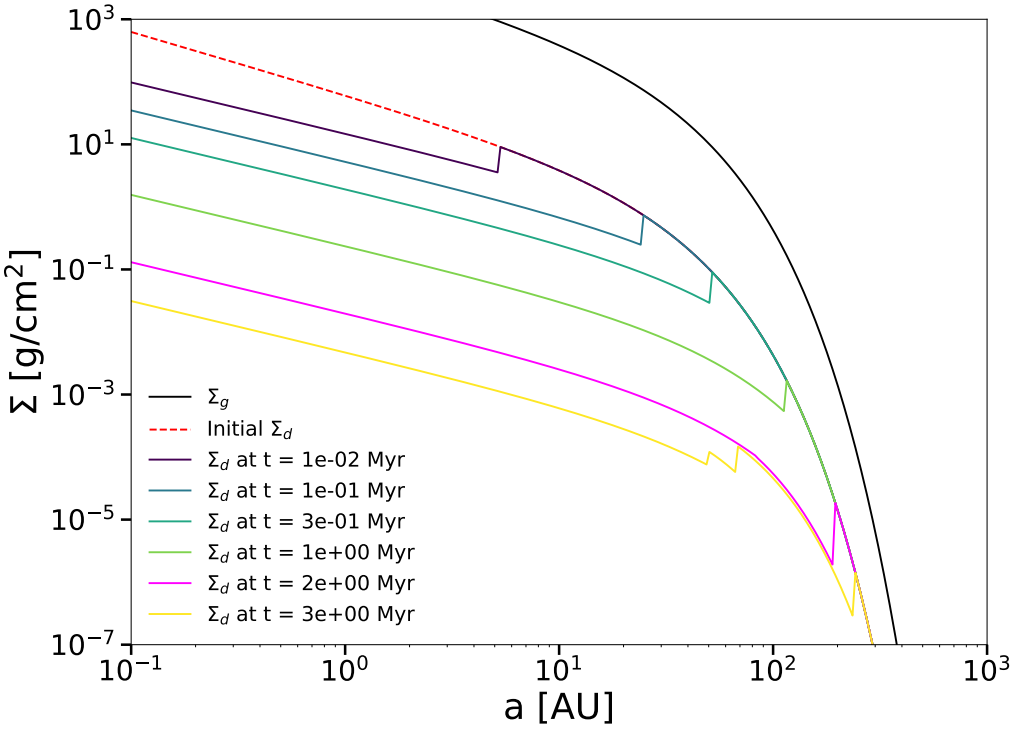

Figure 2.8: The surface density of the disk DR Tau as a function of time. As with TW Hydra, the gaseous surface density is shown as a solid black line, and the initial solid surface density is shown as a dashed red line. The evolved solid surface density is then plotted for several times as the solid colored lines. As the disk ages, it passes from the 1st regime (as described in Lambrechts & Johansen 2014) to the 2nd and eventually 3rd regimes (as described in Powell et al. 2017). For this disk, we find $t_{\text{Transition}} = 2.15$ Myr (shown in magenta).

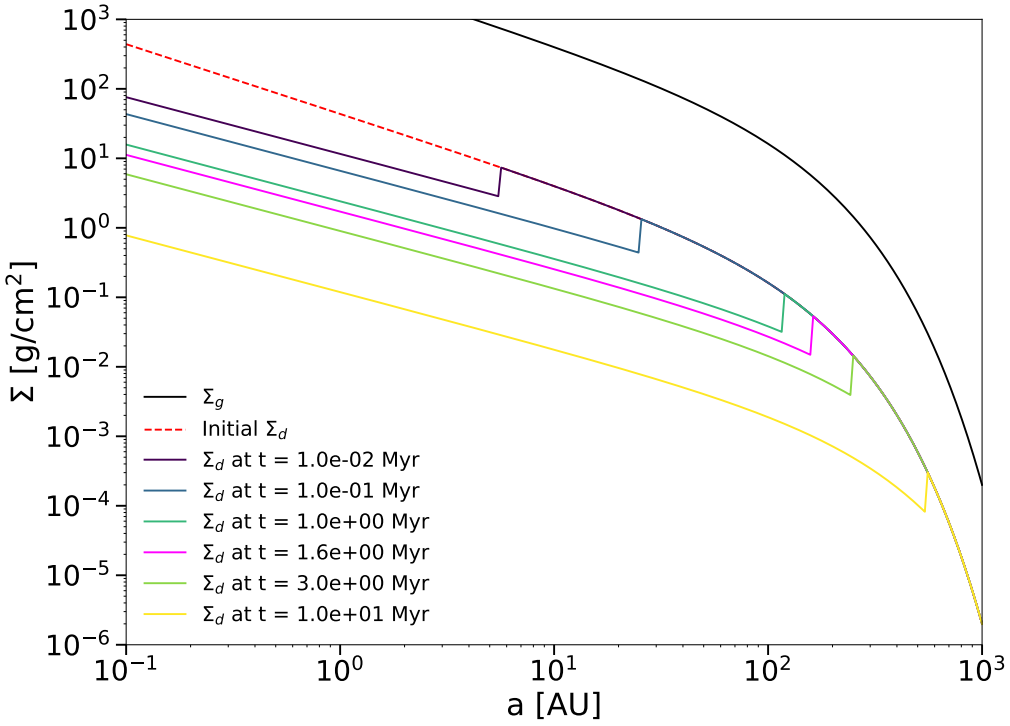

Figure 2.9: The surface density of the disk AS 209 as a function of time. The lines are the same as in other figures of the surface density. As the disk ages, the pebble front moves outward, but it does not transition from from the 1st regime (as described in Lambrechts & Johansen 2014) to the 2nd and eventually 3rd regimes. The magenta line shows the disk's current estimated age. This disks is one of the largest in our sample, maintaining a high surface density out to several hundred AU.

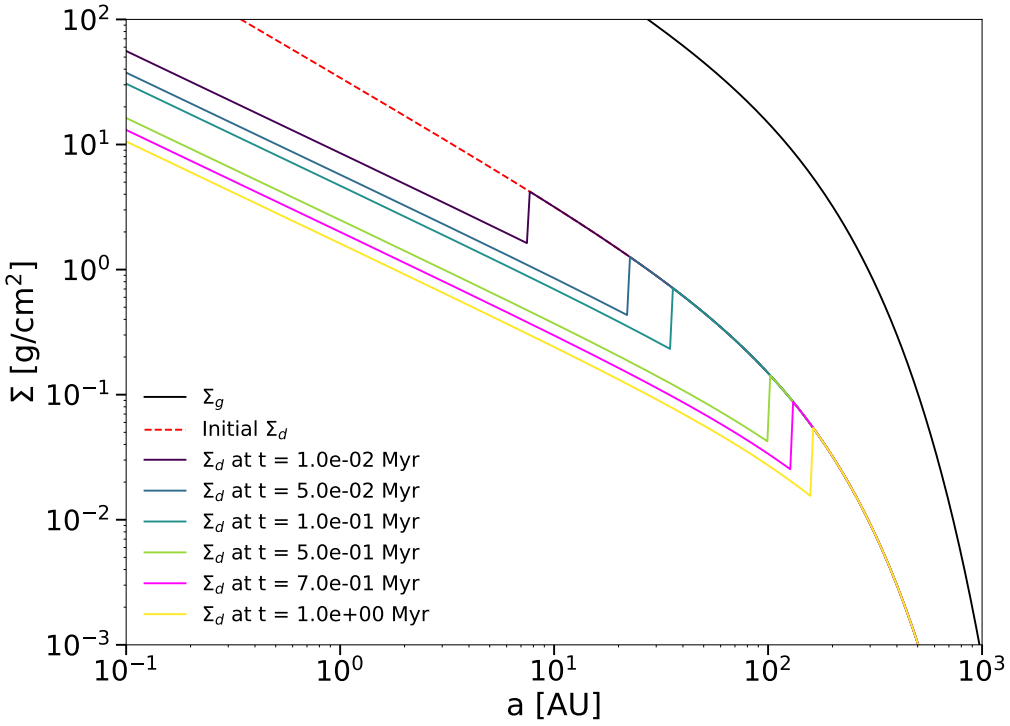

Figure 2.10: The surface density of the disk HD 163296 as a function of time. This figure uses the same line definitions as the other surface density plots, including the magenta line to show the disk's current estimated age. As with AS 209, this disk does not transition out of the 1st regime to the 2nd and 3rd regimes, as the drift driven particle supply continues to exceed the growth driven throughout the disk's lifetime.

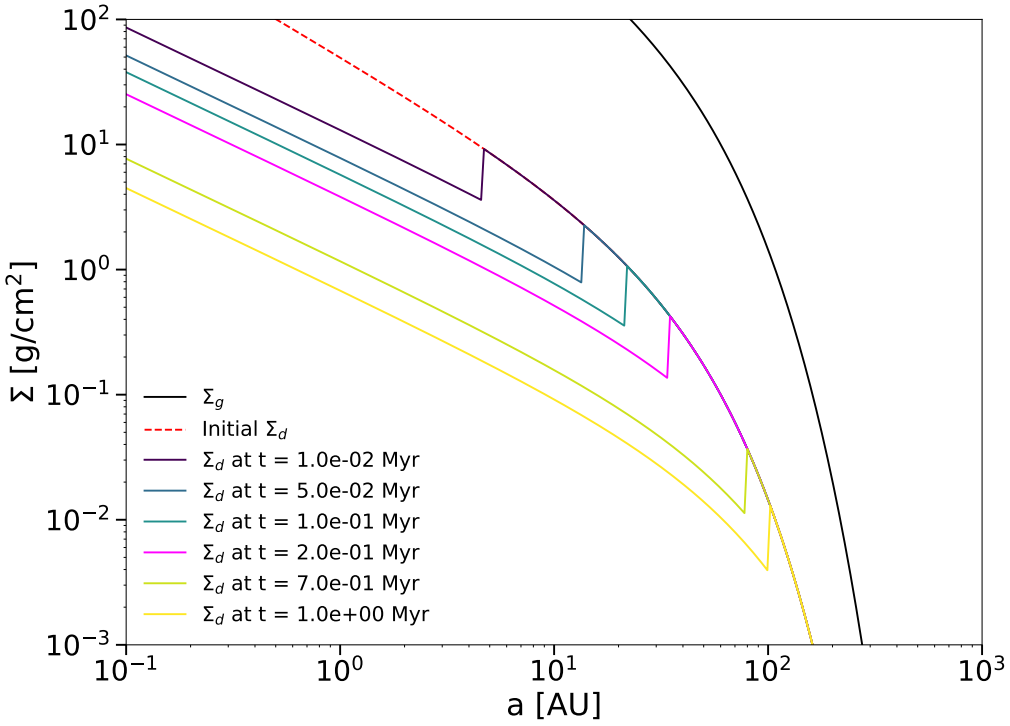

Figure 2.11: The surface density of the disk FT Tau as a function of time. This figure uses the same line definitions as the other surface density plots, including the magenta line to show the disk's current estimated age. This disk also does not transition out of the 1st regime to the 2nd and 3rd regimes, as the drift driven particle supply continues to exceed the growth driven throughout the disk's lifetime.

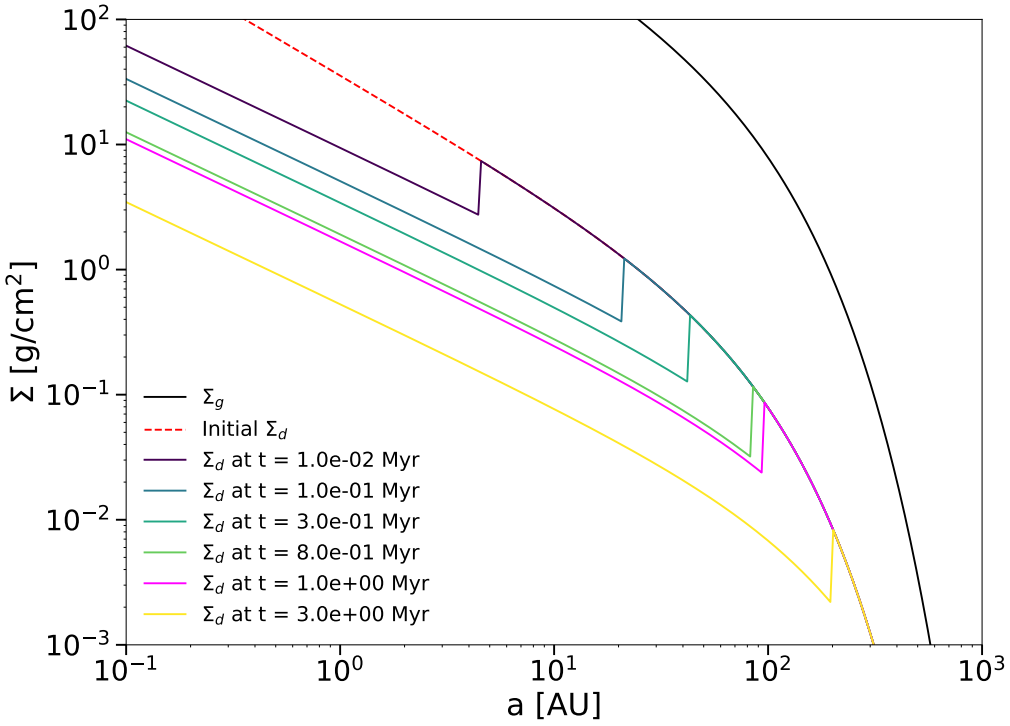

Figure 2.12: The surface density of the disk CY Tau as a function of time. This figure uses the same line definitions as the other surface density plots, including the magenta line to show the disk's current estimated age. As the disk ages, the pebble front moves outward, but it does not transition from from the 1st regime (as described in Lambrechts & Johansen 2014) to the 2nd and eventually 3rd regimes.

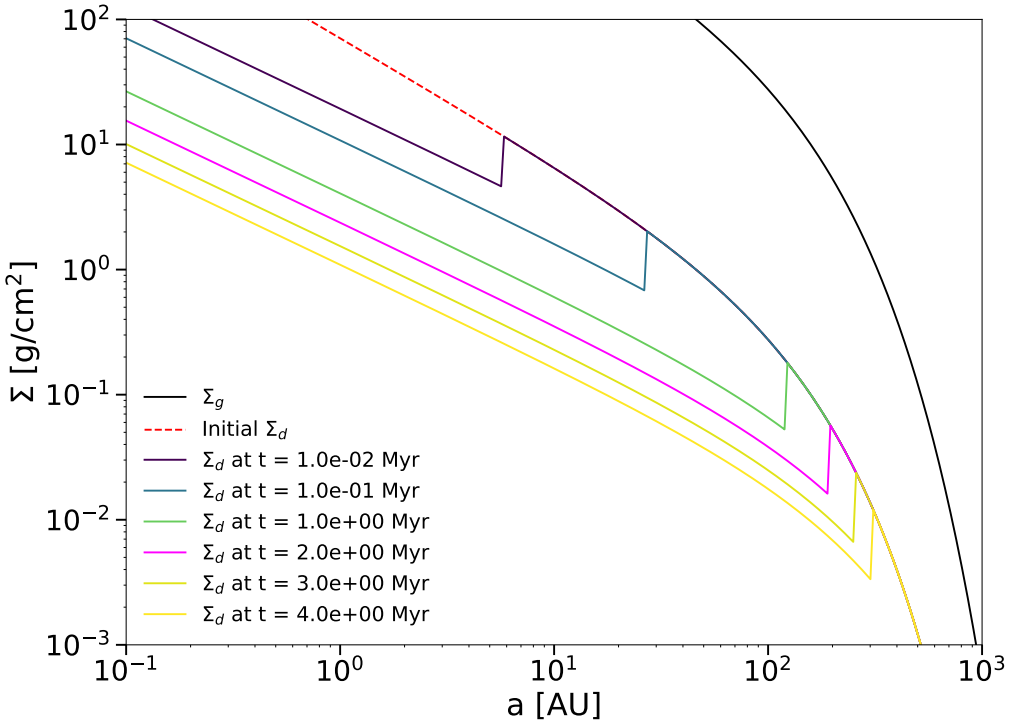

Figure 2.13: The surface density of the disk DoAR 25 as a function of time. The gaseous surface density is shown as a solid black line, and the initial solid surface density is shown as a dashed red line. The evolved solid surface density is then plotted for several times as the solid colored lines, including the magenta line to show the disk's current estimated age. This disk does not transition within the time-span tested, out to 4 Myr.

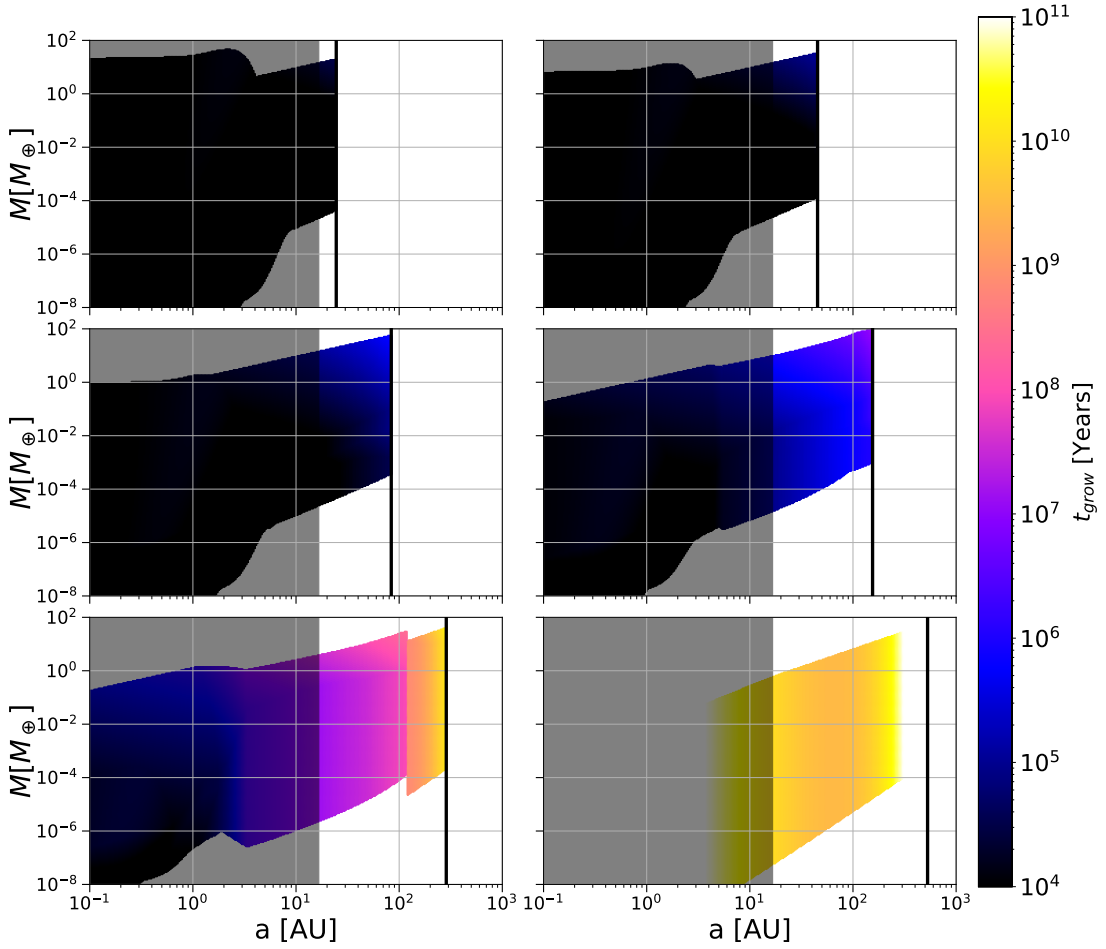

Figure 2.14: The particle growth time is shown as a function of both semi-major axis and core mass for the disk TW Hydra at six different times through the disk's lifetime (100,000 years, 250,000 years, 630,000 years, 1.6 Myrs, 4 Myrs, and 10 Myrs from top left to bottom right). The shaded region shows where the disk is fragmentation dominated, and our maximum particle size prescription does not apply. The bottom edge of this growth region is defined as the minimum mass where traditional pebble accretion is active, while the top edge is set as the flow isolation mass for these protoplanetary cores.

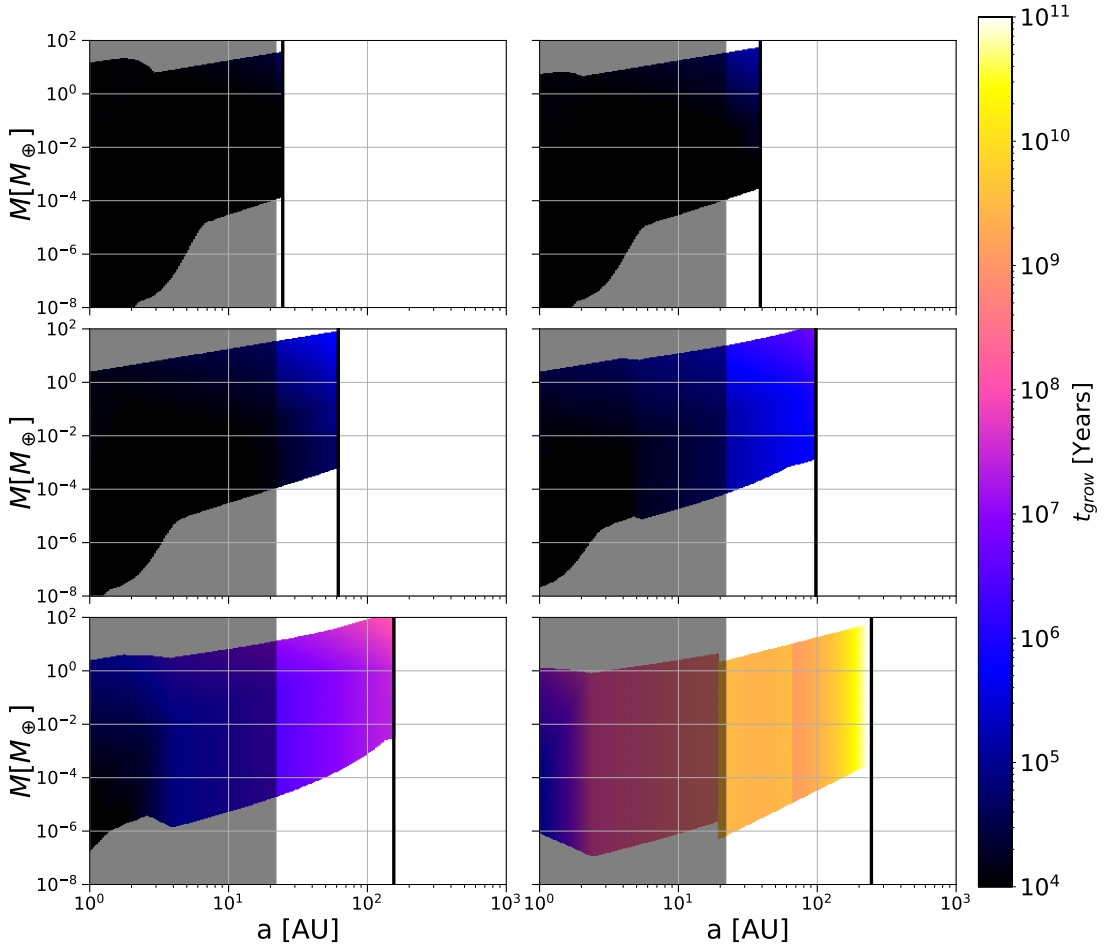

Figure 2.15: The particle growth time is shown as a function of both semi-major axis and core mass for the disk DR Tau at six different times through the disk's lifetime (100,000 years, 200,000 years, 400,000 years, 800,000 years, 1.6 Myrs, and 3.1 Myrs from top left to bottom right). As with the other growth time figures, the shaded region shows where the disk is fragmentation dominated, and our maximum particle size prescription does not apply. Notice how much the growth time extends in the fifth and sixth panels, where the disk has transitioned to the 2nd and then 3rd regime.

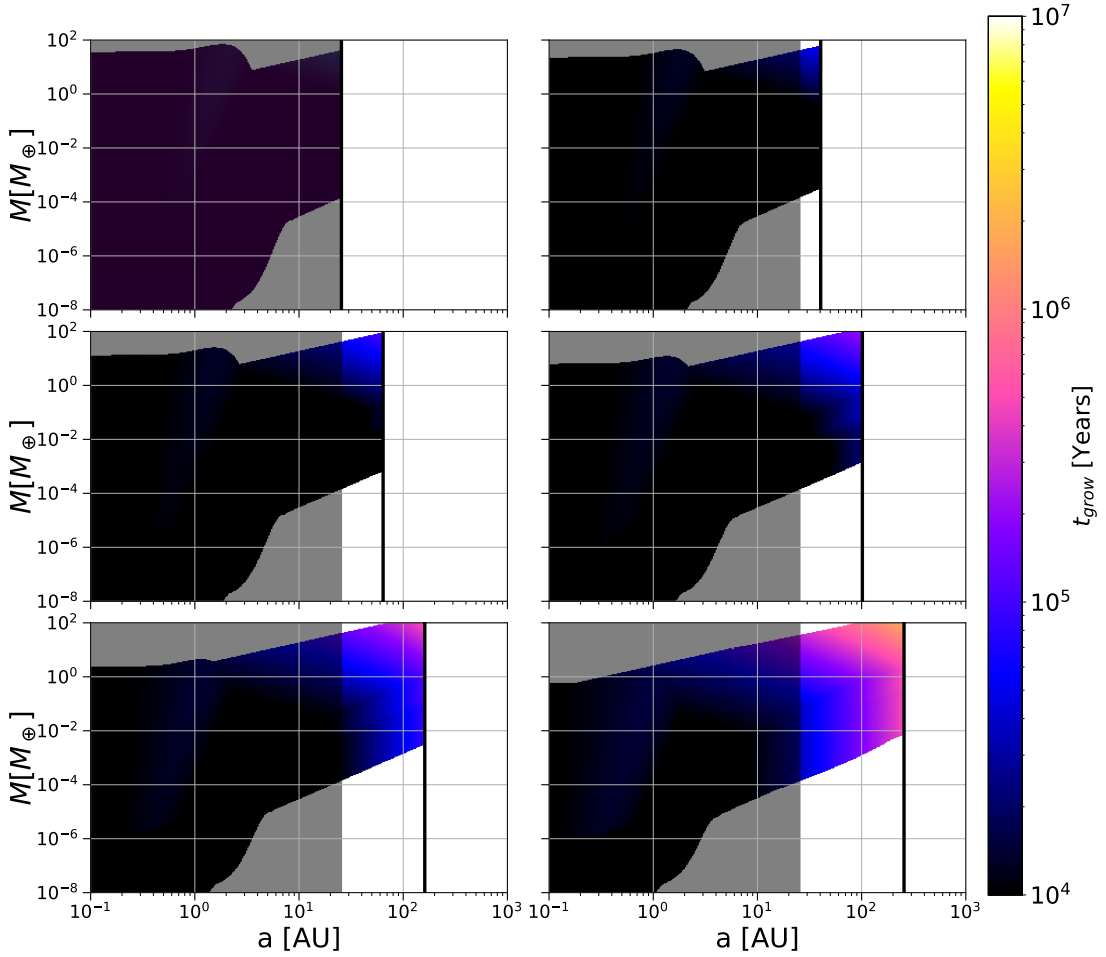

Figure 2.16: The particle growth time is shown as a function of both semi-major axis and core mass for the disk AS 209 at six different times through the disk's lifetime (100,000 years, 200,000 years, 400,000 years, 800,000 years, 1.6 Myrs, and 3.1 Myrs from top left to bottom right). The shaded region shows where the disk is fragmentation dominated, and our maximum particle size prescription does not apply. Because this disk does not transition out of the 1st regime, it maintains the potential for growing planetesimals to their flow isolation mass throughout its lifetime.

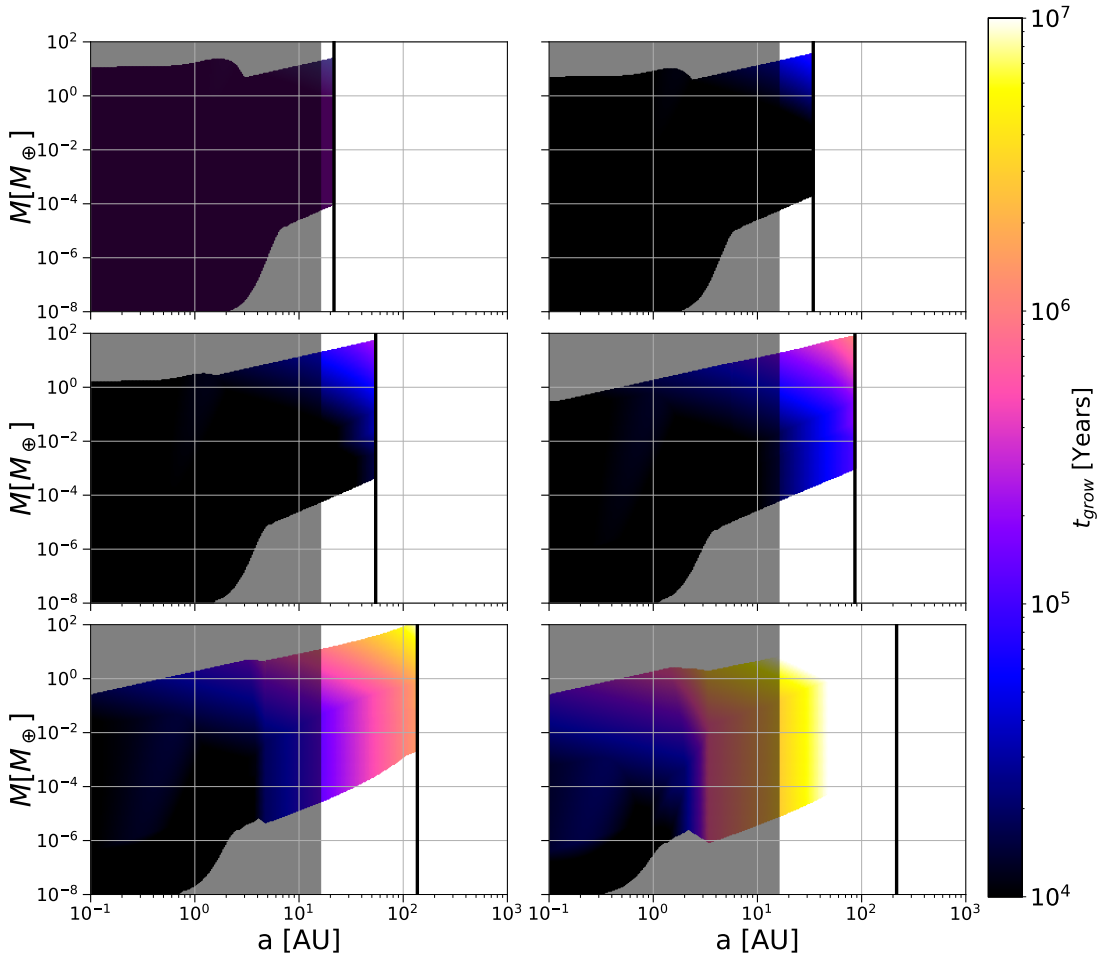

Figure 2.17: The particle growth time is shown as a function of both semi-major axis and core mass for the disk FT Tau at six different times through the disk's lifetime (100,000 years, 200,000 years, 400,000 years, 800,000 years, 1.6 Myrs, and 3.1 Myrs from top left to bottom right). The shaded region shows where the disk is fragmentation dominated, and our maximum particle size prescription does not apply. As with the other disks which stay in the 1st regime, FT Tau can grow planetesimals to their flow isolation mass throughout its lifetime. However, in practice the solid surface density falls considerably in the disk's later years, making growing planetesimals to their flow isolation masses rather unlikely.

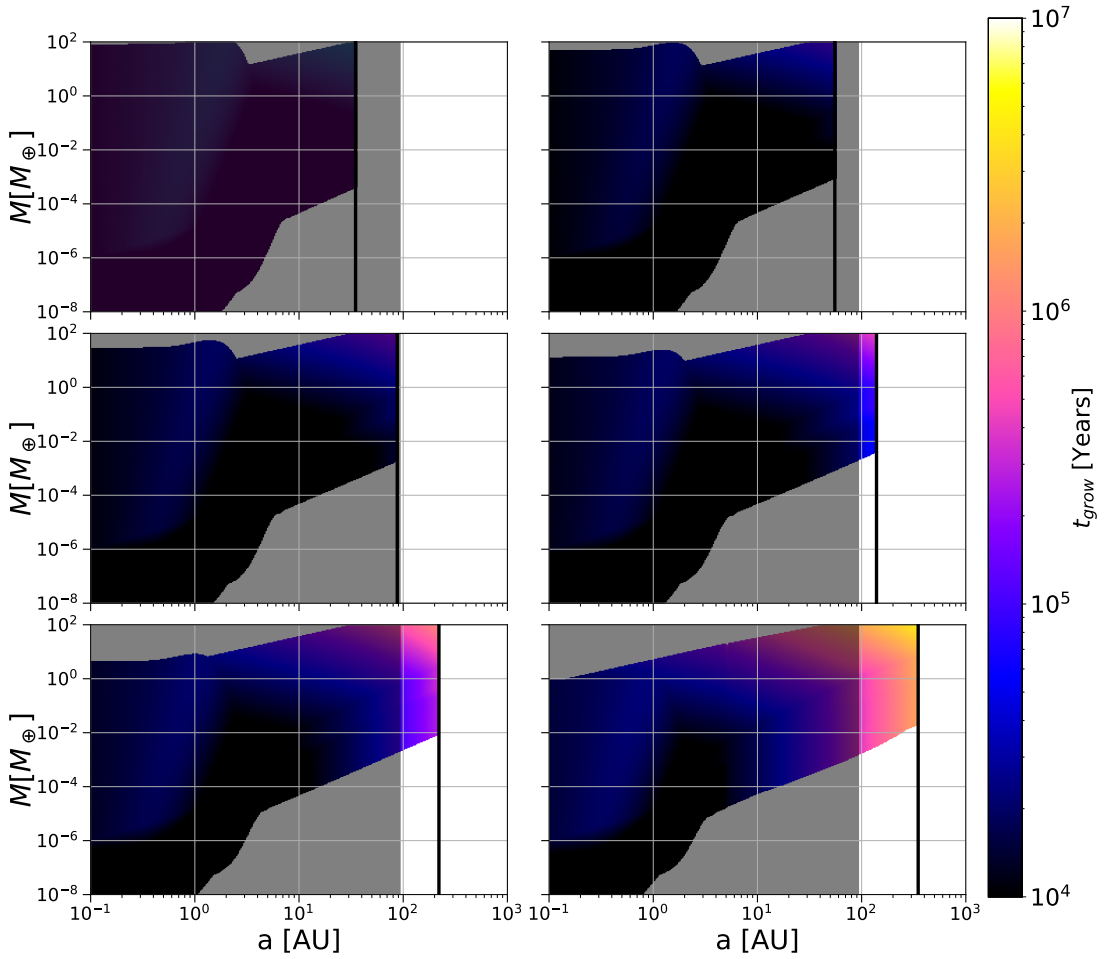

Figure 2.18: The particle growth time is shown as a function of both semi-major axis and core mass for the disk HD 163296 at six different times through the disk's lifetime (100,000 years, 220,000 years, 480,000 years, 1 Myr, 2.3 Myrs, and 5 Myrs from top left to bottom right). The shaded region shows where the disk is fragmentation dominated, and our maximum particle size prescription does not apply. Though this disk never leaves the 1st regime, its solid surface density does eventually fall to the point that growing additional planetesimals to their flow isolation masses is quite unlikely (see the fifth and sixth panels).

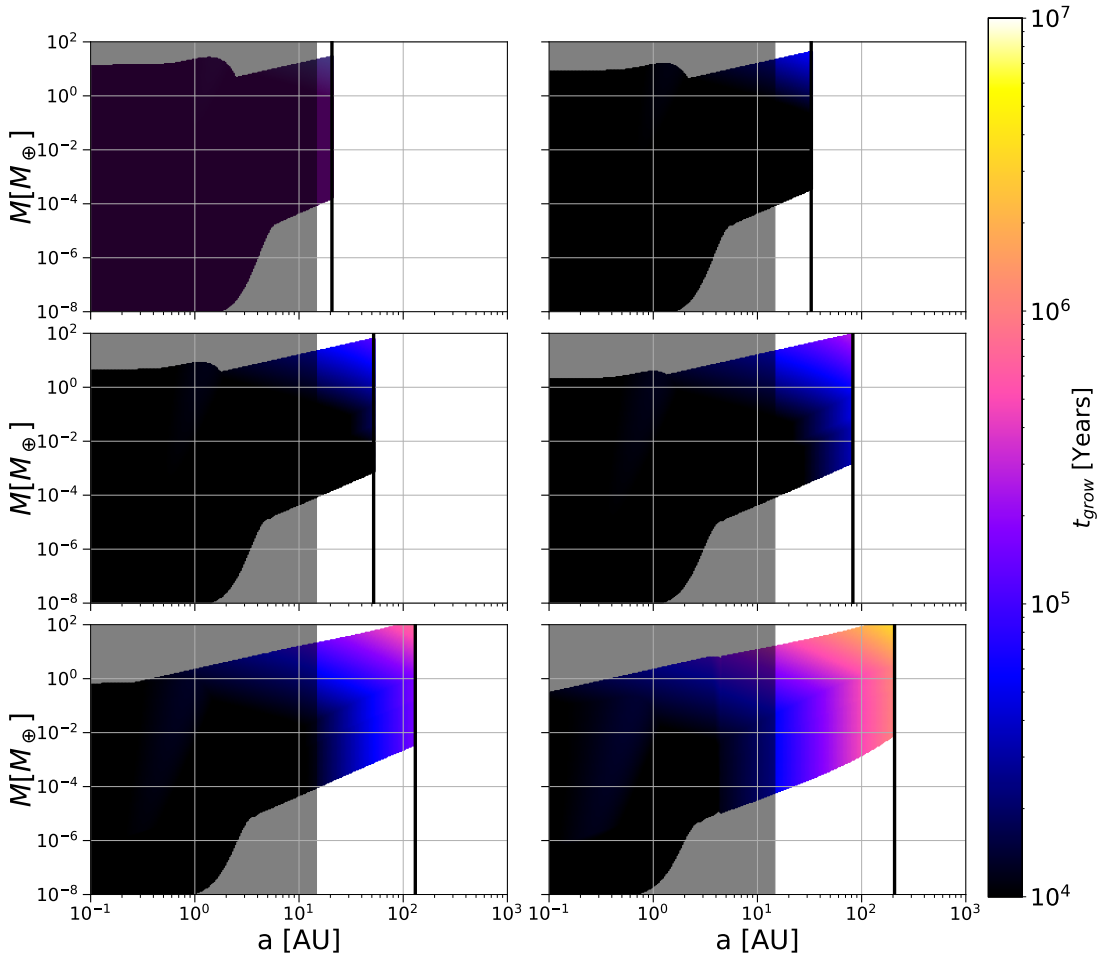

Figure 2.19: The particle growth time is shown as a function of both semi-major axis and core mass for the disk CY Tau at six different times through the disk's lifetime (100,000 years, 200,000 years, 400,000 years, 800,000 years, 1.6 Myrs, and 3.1 Myrs from top left to bottom right). The shaded region shows where the disk is fragmentation dominated, and our maximum particle size prescription does not apply. As with several other of the disks in this sample, this disk never leaves the 1st regime, but it does see a significant falloff in solid surface density, particularly in the sixth panel shown here. This makes it hard to imagine planetesimals continuing to grow their flow isolation mass 3 Myrs into the disk's lifetime.

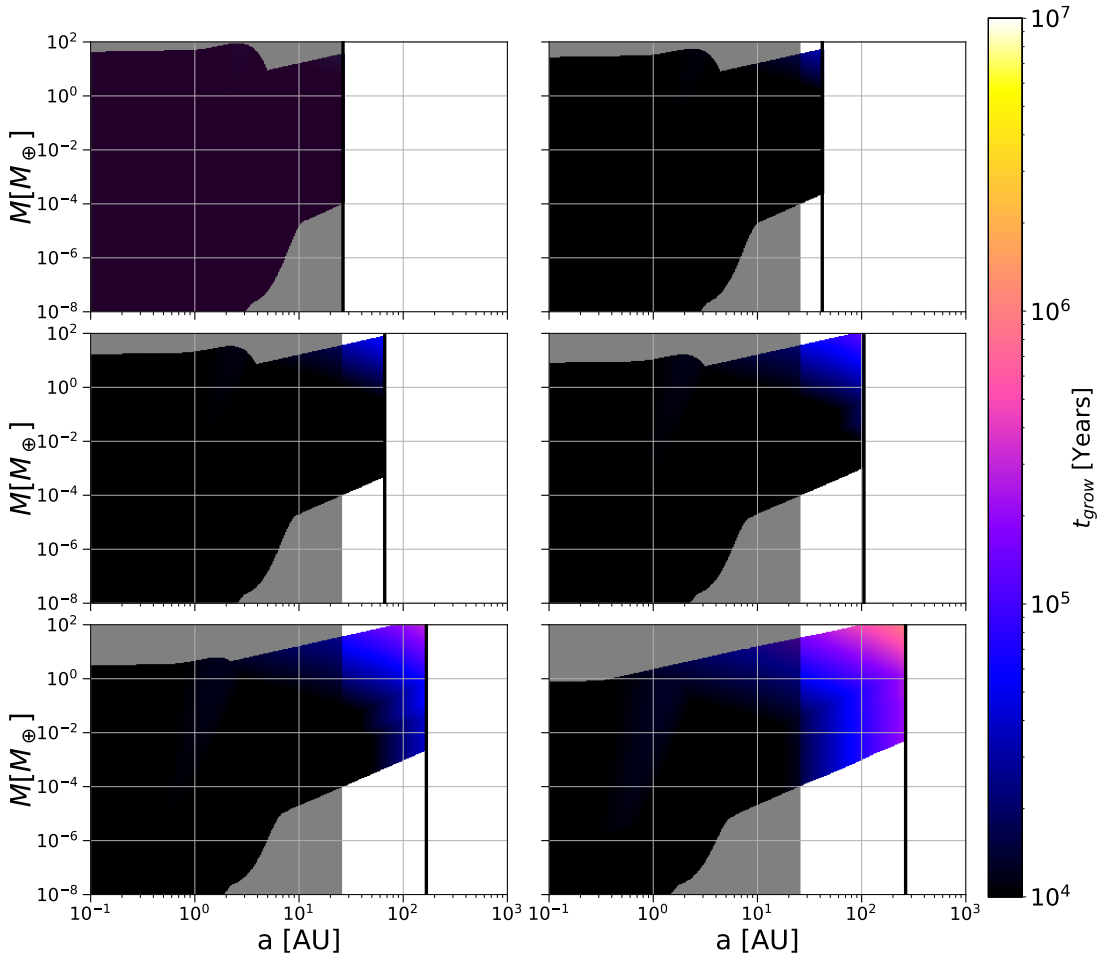

Figure 2.20: The particle growth time is shown as a function of both semi-major axis and core mass for the disk DoAr 25 at six different times through the disk's lifetime (100,000 years, 200,000 years, 400,000 years, 800,000 years, 1.6 Myrs, and 3.1 Myrs from top left to bottom right). The shaded region shows where the disk is fragmentation dominated, and our maximum particle size prescription does not apply. This disk does not transition out of the 1st regime, and also maintains a high enough solid surface density for several Myrs that it is possible that some planetesimals may grow to their flow isolation masses even late in the disk's lifetime.

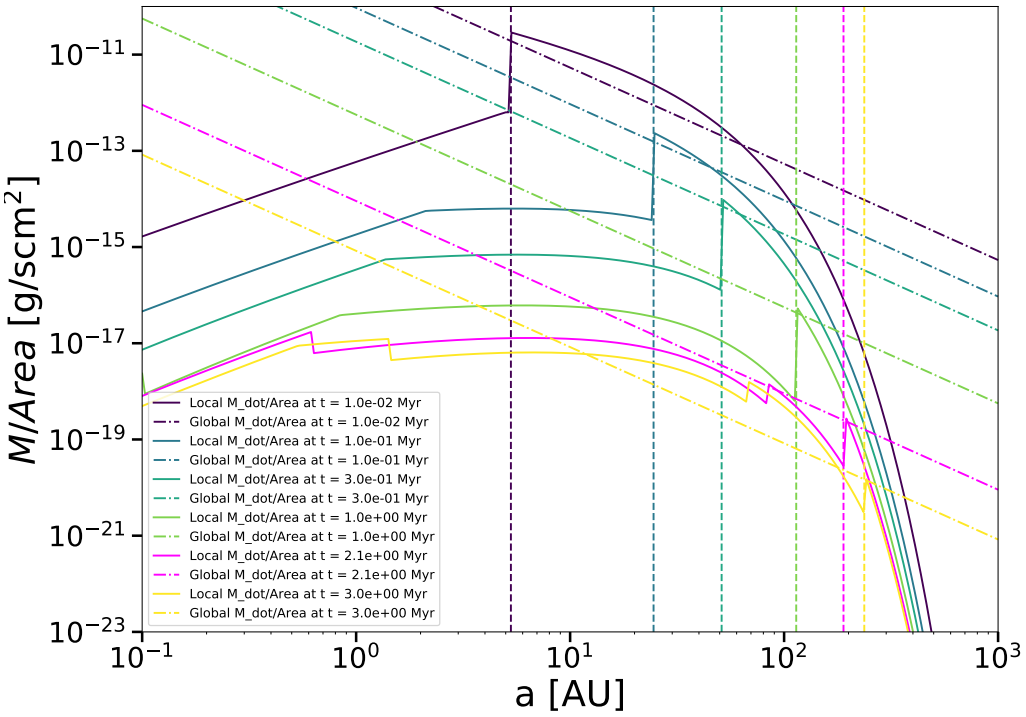

Figure 2.21: The $\dot{M}$ per area of the disk DR Tau as a function of time. As the disk ages, the drifted $\dot{M}$ per area decreases, eventually allowing the disk to transition, here at 2.15 Myr. This disk's age estimates vary from 0.1 to 3 Myr, but we estimate the age as 1 Myr, shown in magenta. This would imply that the disk has not yet transitioned, but will soon.

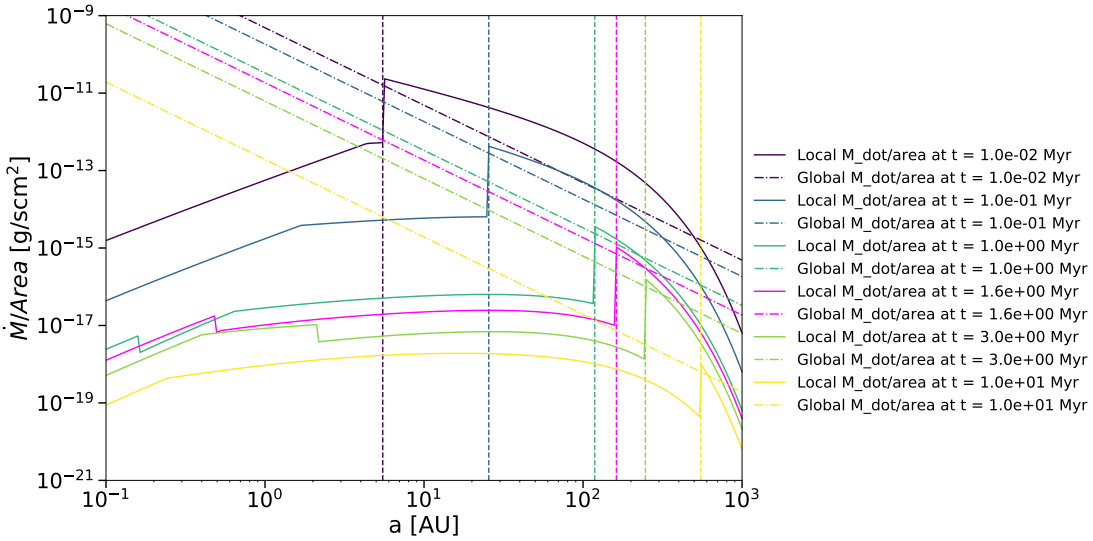

Figure 2.22: The $\dot{M}$ per area of the disk AS 209 as a function of time. As the disk ages, the drifted $\dot{M}$ per area decreases, but not quickly enough to fall below the grown $\dot{M}$ per area. This prevents the disk from transitioning to the 2nd and 3rd regimes, as TW Hydra and DR Tau do. The magenta line shows the disk's current estimated age.

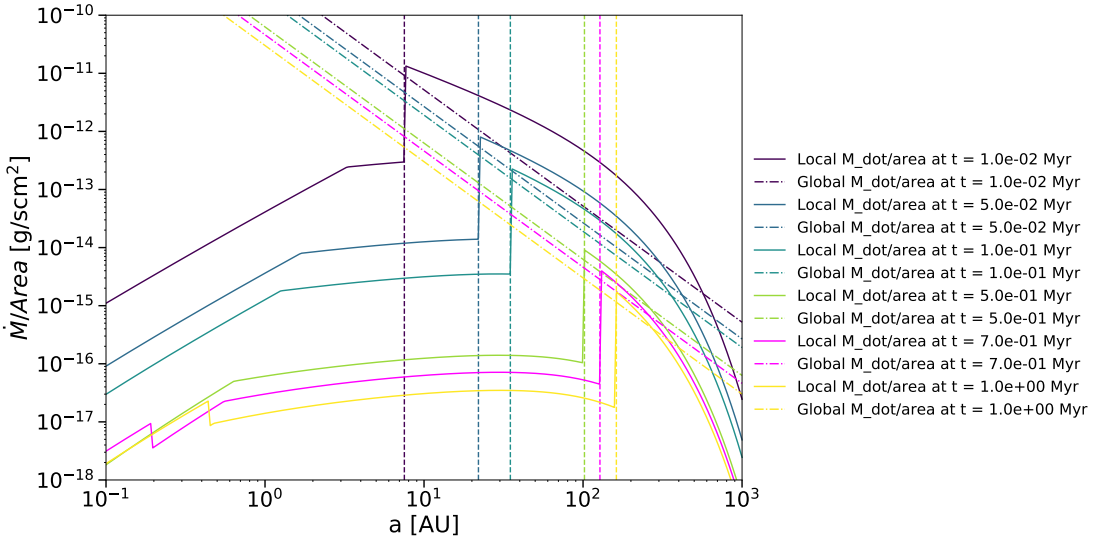

Figure 2.23: The $\dot{M}$ per area of the disk HD 163296 as a function of time. As the disk ages, the drifted $\dot{M}$ per area decreases, but not quickly enough to fall below the grown $\dot{M}$ per area. This prevents the disk from transitioning to the 2nd and 3rd regimes, as TW Hydra and DR Tau do. The magenta line shows the disk's current estimated age.

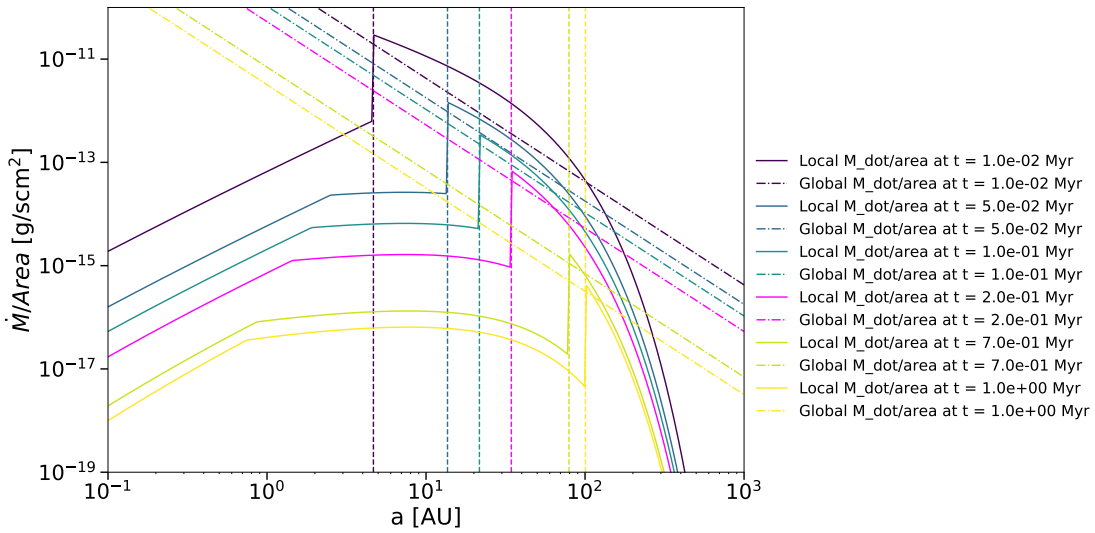

Figure 2.24: The $\dot{M}$ per area of the disk FT Tau as a function of time. As the disk ages, the drifted $\dot{M}$ per area decreases, but not quickly enough to fall below the grown $\dot{M}$ per area. This prevents the disk from transitioning to the 2nd and 3rd regimes, as TW Hydra and DR Tau do. The magenta line shows the disk's current estimated age.

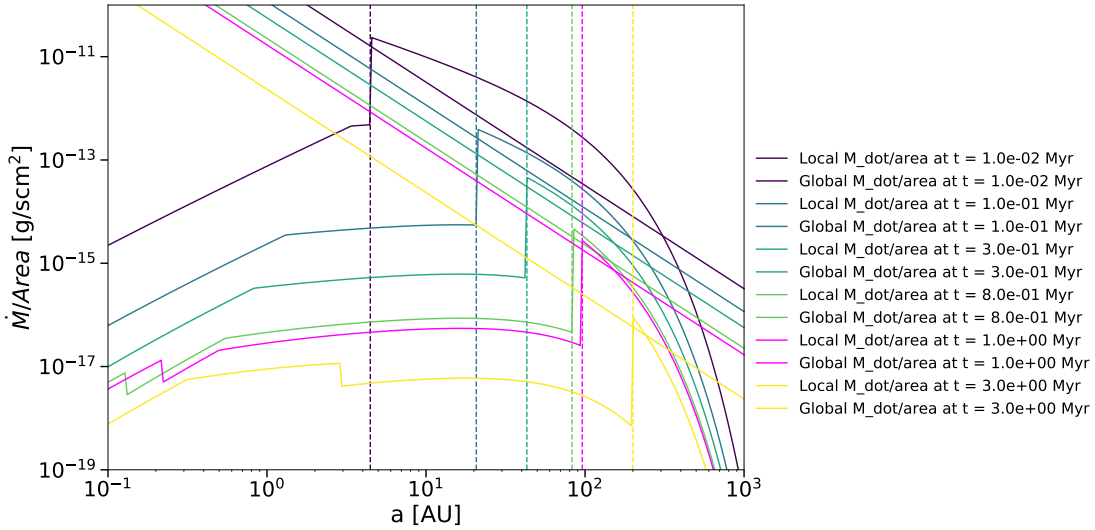

Figure 2.25: The $\dot{M}$ per area of the disk CY Tau as a function of time. As the disk ages, the drifted $\dot{M}$ per area decreases, but not quickly enough to fall below the grown $\dot{M}$ per area. This prevents the disk from transitioning to the 2nd and 3rd regimes, as TW Hydra and DR Tau do. The magenta line shows the disk's current estimated age.

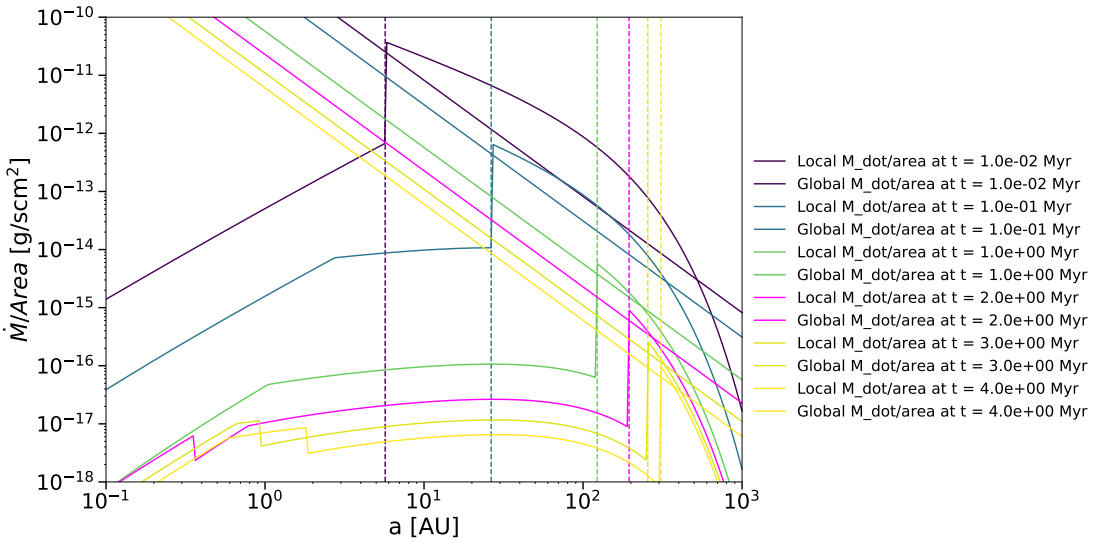

Figure 2.26: The $\dot{M}$ per area of the disk DoAr 25 as a function of time. As the disk ages, the drifted $\dot{M}$ per area decreases, but not quickly enough to fall below the grown $\dot{M}$ per area. This prevents the disk from transitioning to the 2nd and 3rd regimes, as TW Hydra and DR Tau do. The magenta line shows the disk's current estimated age.

see little evidence for variation in this parameter. Note that the flow isolation mass is interestingly independent of the overall surface density normalization.

To show the strength of the flow isolation mass's dependence on disk temperature and location in the disk, we plot each in Figures 1 and 1. For each of these figures, we use values of the disk DR Tau as fiducial, with $M_* = 0.8 M_\odot$, $T_0 = 121K$, and $t_{\rm disk} = 1Myr$.

2. Parameters which affect growth time

The overall disk mass in solid particles is the parameter which has the largest effect on overall normalization for planetary growth times in our pebble accretion model. The more mass that is available in dust or other solid particles, the shorter planetary growth times become. As one can see in our plot of t_{grow} for each disk,

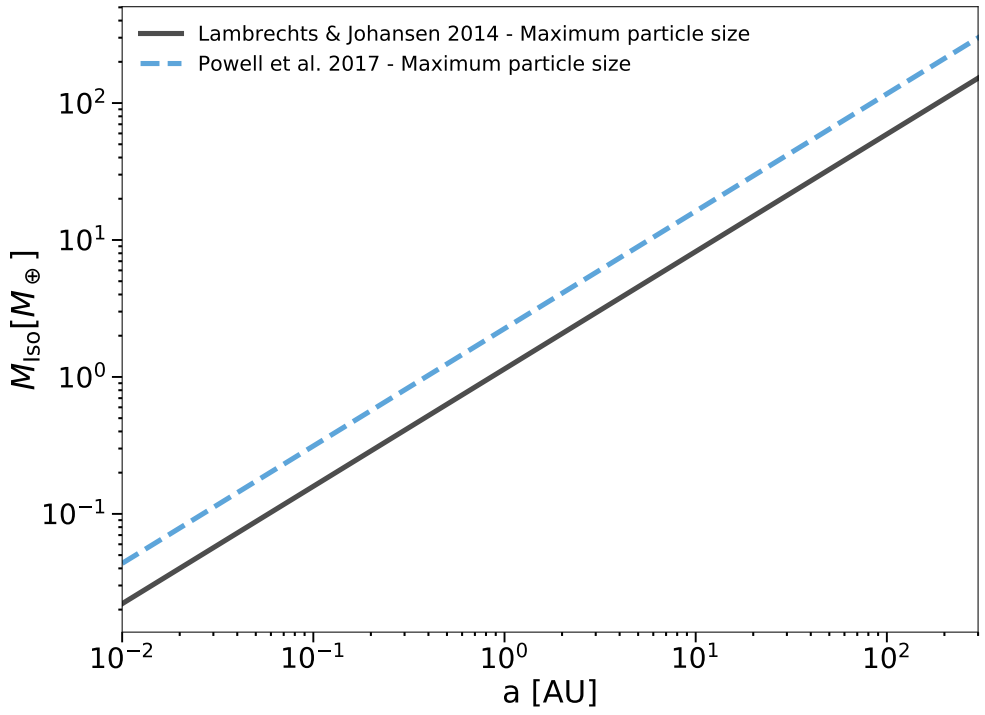

Figure 2.27: This is a plot of flow isolation mass versus semi-major axis, for both the maximum particle sizes.

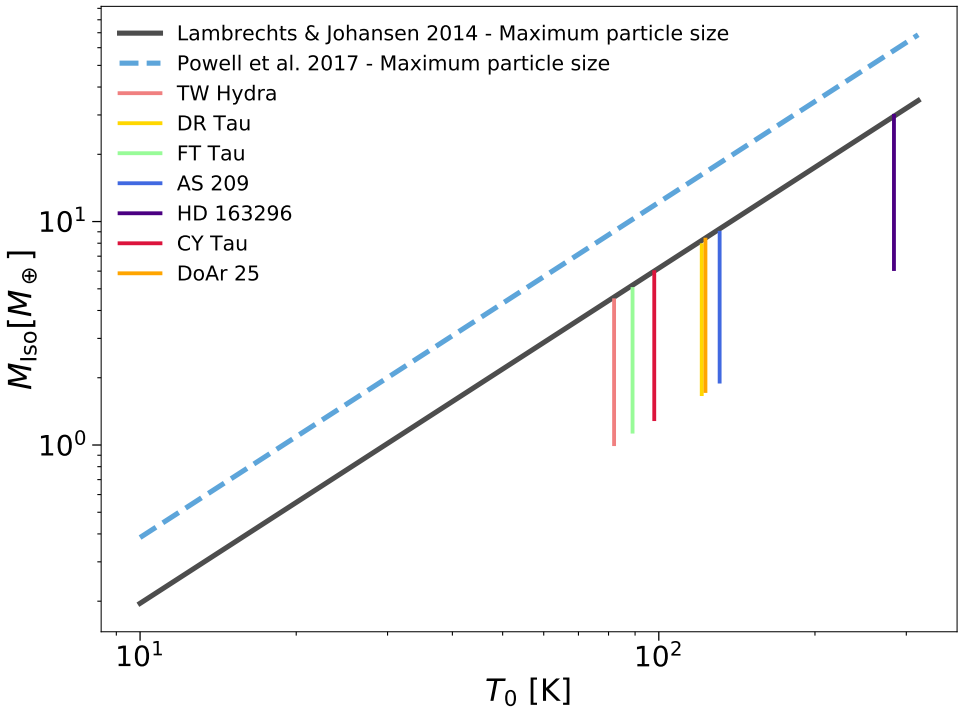

Figure 2.28: This is a plot of flow isolation mass versus temperature normalization, for both the maximum particle sizes. We assume a semi-major axis of 10 AU for this figure. The T_0 values are shown for each object in the sample as vertical lines. The temperature across each disk is modeled as $T = T_0 \left(\frac{a}{AU}\right)^{-3/7}$.

as the disk ages, its solid surface density falls, extending the growth times for planetesimals of all masses. We previously noted the fall in surface density and rise in growth time when a disk moves from the 1st regime to the 2nd and 3rd, but this change is present even within a given disk regime as well. This is especially apparent in the t_{grow} plots for disks which do not transition from this 1st disk regime (every disk in the sample except TW Hydra and DR Tau).

This falling growth efficiency means that, for disks which do transition from the 1st to 2nd and 3rd regimes, essentially all solid body planet formation must occur before this transition occurs. This $t_{\text{Transition}}$ can serve then as a sort of last call for forming solid planetary cores. After a protoplanetary disk transitions, one can expect its existing planetesimals to grow significantly only via gas accretion.

2.4 Discussion and Conclusions

2.4.1 Primary Result and Implications

By combining careful modeling of particle drift and growth in protoplanetary disks and flow isolation, we have derived a simple prescription for the expected final solid mass of planets formed in these disks. Dependent only on a few parameters, including the age of the disk, the initial dust-to-gas ratio, and the semi-major axis of our budding planet, this model carefully tracks the surface density and maximum particle size in these disks, translating it into a final planet mass. We implement two different models for maximum particle size in our disks, based on Lambrechts & Johansen (2014) and Powell et al. (2017). We expect disks to transition between these two models as the

disks evolve, and the particle supply for the largest particles changes.

We describe the important role that the pebble front plays in setting how a protoplanetary disk evolves, and the particles within it grow. Using this understanding along with our modeling of the small particle supply, both drifted and grown, we define three regimes which a disk may pass through. In the 1st regime, the largest solid particles are largely drifted in from the pebble front, and overall surface density is initially high. Over time, as the solid surface density decreases, and the pebble front moves outward, the supply of solid particles from the pebble front falls such that it overtaken by solid particles grown relatively in situ. At this time, the disk transitions to the 2nd regime, and the solid particles sizes are modeled in a new way. This occurs first near the pebble front, drifting inwards, as the pebble front "bounces back" and the disk is further drained of solids. Lastly, the disk transitions to the 3rd regime when the pebble front hits the inner edge of the disk and the entire disk is modeled in a manner based on Powell et al. (2017).

To estimate the relative efficiency of planetary growth via pebble accretion in each of these three regimes, we compare the disk lifetime to the growth times for planetesimals in Figure 2.2.2. The growth efficiency is much higher in the 1st and 2nd regime than the 3rd, thanks to the reduced solid surface density in the 3rd regime as dust drifts into the star. For this reason, we can use the time of transition from the 1st regime ($t_{\text{Transition}}$) as a rough end of the era of planetesimal formation. Planetesimals which exist at the start of the 2nd regime may continue to grow as long as the disk sticks around, but new planetary scale cores are unlikely to form after this point.

We apply our disk and pebble accretion models to a sample of seven protoplanetary disks, generating surface densities, maximum particle sizes and estimated planetesimal growth times for each. Of the seven disks we examine, just two (TW Hydra and DR Tau) ever transition from the 1st disk regime (where Lambrechts & Johansen (2014) largely applies) to the 2nd and 3rd disk regimes (where Powell et al. (2017) are dominant). In every disk however, the solid body surface density falls with time, making it increasingly difficult to grow planetesimals via pebble accretion. For each protoplanetary disk we examine, are relatively poorly constrained. For this reason, we present our results for each disk across a wide range of possible ages.

2.4.2 Estimates in the model

One aspect of the disk on which our model depends relatively strongly is the pressure profile of the disk, as expressed through the parameter η. As a reminder, $\eta = \frac{\partial \log P}{\partial \log a}$, and can often be approximated as $\eta \approx \frac{c_s^2}{2v_{kep}^2}$, which we use for the entirety of this study. This measure of the pressure profile is especially important as it determines the maximum particle size when the Epstein drag law applies in the 1st disk regime. Additionally, η also determines the surface density in the 1st disk regime when the maximum particle size is in the Stokes drag law.

A follow-up study may examine the role of η more closely, and see whether a numerical approach to more exactly calculate η has an appreciable effect on the particle sizes and surface densities to significantly affect the results of this study.

2.4.3 Conclusions

In this chapter, we model the dynamics and growth of small solids throughout protoplanetary disks, to learn about how, when and where planets form. By modeling the drift and growth of these small solids, we determine the overall solid surface density for each protoplanetary disk along with the maximum particle size through the disk's evolution. We use this information to generate pebble accretion growth rates for injected planetesimals in each of these disks, finding regions and times of particularly rapid growth. Two of these disks which we examine transition from a disk regime in which their largest particles are supplied by drift to one in which the largest particles are instead primarily grown in situ. After transitioning, these disks show much lower solid surface densities, making it very difficult to see these disks continuing to grow planetesimals.

In our work throughout this chapter, we have focused on a singular drag law to define the dynamics of our pebbles, the Epstein drag regime. In future works, one could expand this model to include the Stokes and Ram drag regimes as well, which generally apply to larger particles. Additionally, one could link the disk and pebble accretion modeling presented in this chapter to numerical simulations of protoplanetary disks, such as those performed by Birnstiel et al. (2012) and collaborators. This could supply us with checks on our maximum particle sizes and surface densities, allowing us to make more informed statements about exactly what size and type of planets we expect to form in observed protoplanetary disks.

Chapter 3

Gas Assisted Growth of Small Planetesimals

3.1 Introduction

In the prior chapter, we introduce and describe our disk evolution and pebble accretion models. We use these models to examine planetary growth conditions in a sample of disks, learning how early planetesimals need to form to create the exoplanetary demographics which we observe. In this chapter, we apply the same models to a new regime of parameter space to understand the effects of gas-particle interactions on the smallest solids in a disk. In comparison to classical accretion, pebble accretion typically has the largest increase in growth efficiency thanks to the expansion of the cross section for growth. This expanded cross section decreases as you lower the mass of the larger solid body in the interaction, until it eventually falls to the physical cross section of

the solid. This is traditionally thought of as a lower mass limit for pebble accretion. However, as explained in the previous chapter, pebble accretion also determines the relative velocity during particle collisions, thanks to the gas-particle interactions. This effect on the relative velocity continues even below the masses at which the cross section for interaction becomes simply the physical cross section. In this chapter, we examine this effect to learn how gas drag affects growth rates for solid particles, down to very small particle sizes.

First, we present our existing model, and the changes which we made to expand the region of applicability. These are presented in Section 3.2. We then apply this model with our disk model to estimate growth times for a wide variety of solid particle sizes in Section 3.3, just as we did in the prior chapter. Here, however, rather than focusing on a planetesimal core mass, we examine particle pairs down to the cm-scale. We find several interesting regions for rapid growth, each of which we examine and explain. For these small particle interactions, the relative velocity of collision between particle pairs is the determining factor in whether growth, bouncing, or fragmentation occur. For this reason, we model the relative velocity using a Maxwellian probability distribution, and examine the behavior not only at the average velocity, but also at the bottom 10% level. In this way, we can learn about growth events which are relatively rare, but still common enough to impact the final solid particle masses in the disk. Final thoughts and suggestions for future work are found in Section 3.4.

3.2 Pebble Accretion Model

3.2.1 Review of Model from Rosenthal et al. 2018

As in Rosenthal et al. (2018), Rosenthal & Murray-Clay (2018), and Chapter 2, we employ an order of magnitude model in which we consider two bodies in our disk. The larger of these, the planetesimal or "core" has traditionally been large enough that its orbital velocity is unaffected by the gas, keeping the orbit Keplerian. In this chapter we will modify that assumption, allowing the large body to also experience gas drag.

The 2nd party in this interaction is the so called pebble. So named because of their small size, in this chapter we instead allow them to vary by more than 14 orders of magnitude. These smaller bodies are generally more affected by gas drag than their larger counterparts, and, because of this velocity difference, come into frequent growth encounters with their larger brethren. Because the sizes of each body are so important to the gas interactions, we perform every calculation for an individual particle size, even though a variety of particle sizes are likely present in the disk.

Gas has a variety of impacts on a particle accreting onto a larger body. The drag from the gas may slow the small particle relative to the large, allowing for a more gentle collision, more favorable for growth. However, depending on the particle sizes, involved, it may instead inhibit growth, by preventing the two particles from colliding at all. To determine which of these occurs, we need to first define a few relevant radii. The stability radius $R_{\rm stab}$ is the smallest radius at which a particle may stably orbit a larger body. Outside of this radius, a particle will be sheared away from the larger body by interactions with the gas or the star, while inside, it will inspiral into the larger body.

We calculate this radius by matching the force from gas drag on the smaller particle with the gravitational force from the larger body, shown in Equation 3.2.1. The Bondi radius, R_{Bondi}, on the other hand, is an approximate estimate of the size of proto-atmosphere around a larger body. It is calculated as the point at which the sound speed of the gas matches the escape velocity of the larger body, shown in Equation 3.2.1.

$$R_{\text{stab}} = \sqrt{\frac{GMm}{F_D}} \tag{3.1}$$

$$R_{\text{Bondi}} = \frac{GM}{{c_s}^2} \tag{3.2}$$

where M is the mass of the larger body, m is the mass of the smaller particle, F_D is the drag force on the smaller particle, and c_s is the sound speed in the gas.

By comparing these two radii, we can determine which of the two gas effect may be occurring. If the stability radius exceeds the Bondi radius, particles can orbit without entering the larger body's proto-atmosphere. This allows these particles to continually feel gas drag, losing kinetic energy relative to the larger body until eventually it falls below larger body's capture energy. The gas drag then causes the smaller body to fall into the larger. We determine when this occurs by comparing the work done by gas drag on a particle during an interaction to its relative kinetic energy. When the work exceeds the energy, the particle is accreted, but when it falls short, the particle escapes.

If the Bondi radius is instead the larger quantity of the two, the gas dynamics inside the proto-atmosphere are now crucial to understanding the smaller particle's trajectory. Because the proto-atmosphere is roughly at rest relative to the larger body which it surrounds, gas drag on the smaller particle can now prevent accretion. We again compare the work done by gas drag to the particle's relative kinetic energy, but now have the opposite result. Here, if the work exceeds the energy the particle comes to rest relative to the gas, following the flow of gas around the larger body, escaping. Only if the energy exceeds the work done by gas drag can the smaller particle plow through the proto-atmosphere and still collide with the larger body.

We calculate growth times in our model using Equations 3.2.1 and 3.2.1. This nicely breaks the problem into three parts, to which we can apply our disk and small particle models. We define growth time as

$$t_{grow} \approx \frac{m}{\dot{m}} \tag{3.3}$$

where m is the mass of the larger body, and where the mass accretion rate $\dot{m}$ is defined as

$$\dot{m} \approx \rho_{\text{solids}} \sigma v_{rel} \tag{3.4}$$

where ρ_{solids} is the disk's density in solids, σ is the cross section for interactions, and v_{rel} is the relative velocity between interacting particles.

To determine the density of small particles encountered, we find ρ_{solids} using

our disk model presented in Chapter 2. This model allows us to calculate the surface density in solids, which we employ here, in Equation 3.2.1.

$$\rho_{\text{solids}} = \frac{\Sigma_d}{H_d} \tag{3.5}$$

$$= \frac{\Sigma_d}{H_{gas}} \sqrt{\frac{\alpha}{St}} \tag{3.6}$$

$$= \frac{\Sigma_d \Omega}{c_s} \sqrt{\frac{\alpha}{St}} \tag{3.7}$$

where Σ_d is the solid surface density, H_d is the scale height for solid particles, H_{gas} is the scale height for gas, and St is the Stokes number for maximum particle size.

The cross section for particle interactions is dependent on the sizes of the Bondi and stability radii, as well as the various scale heights of the disk. The full details of this calculation can be found in Rosenthal et al. (2018), but we provide a short summary here. The accretion cross section is split into two parts, accretion radius (size along r-axis) and accretion scale height (size along z-axis). We present rough formulae for each in Equations 3.2.1 and 3.2.1.

$$R_{\text{Acc}} = max(R_{\text{stab}}, R_{\text{Bondi}}) \tag{3.8}$$

where R_{Acc} is the accretion radius, R_{stab} is the stability radius, and R_{Bondi} is the Bondi radius. The accretion scale height H_{Acc} is then calculated as

$$H_{\rm Acc} = min(R_{\rm Acc}, H_p) \tag{3.9}$$

$$H_p = max(\sqrt{\frac{\alpha}{St}} H_g, H_{KH}) \tag{3.10}$$

$$H_{KH} = \frac{{H_g}^2}{a} min(1, St^{-1/2}) \tag{3.11}$$

where H_g is the gas scale height, and a is the orbital distance to the star. A full explanation for these expressions can be found in Rosenthal et al. (2018), which we will not reproduce here.

Lastly, we calculate the relative velocity between particles following Youdin & Lithwick (2007) and Ormel & Cuzzi (2007). This method uses only the two particles' sizes (as their Stokes numbers) and the gas properties to determine their relative velocity. Here, we reproduce equations 16 and 21(d) from Ormel & Cuzzi (2007), as we use these to calculate our relative velocity

$$v_{\rm rel} = v_{\rm gas} \Bigg(\left[t_k + \frac{{t_1}^2}{1+t_k} \right]_{t_\eta}^{t^*_{12}} + \frac{t_2 - t_1}{t_1 + t_2} \left[\frac{{t_1}^2}{1+t_k} \right]_{t*_{12}}^{t_L} + \left[t_k + \frac{{t_2}^2}{1+t_k} \right]_{t_\eta}^{t^*_{12}} + \frac{t_1 - t_2}{t_1 + t_2} \left[\frac{{t_2}^2}{1+t_k} \right]_{t*_{12}}^{t_L} \Bigg)^{1/2} \tag{3.12}$$

$$\frac{2}{3} \frac{t*_{12}}{t_s} (\frac{t*_{12}}{t_s} - 1)^2 - \frac{1}{1 + \frac{t*_{12}}{t_s}} = -\frac{1}{1 + \frac{t_L}{t_s}} \tag{3.13}$$

where t_k is the integrated variable, t_1 and t_2 are the Stokes numbers of the larger and smaller particles respectively, t_L is the largest eddy turnover time (set to $\frac{1}{\Omega}$), t_η is the smallest eddy turnover time (set to $\frac{t_L}{\sqrt{Re}}$), Re is the Reynolds number, and t_s is the stopping time of the largest particle.

3.2.2 Changes to the model

Here, we present the changes to the pebble accretion model since the last published work presenting it, Rosenthal et al. (2018). The changes to the model can be divided into three types of changes: those focused on the planetesimal core's dynamics, adjustments to the surface density (following 2), and changes to allow the code to utilize a distribution of velocities.

First, we modify our code to allow for planetesimals to move on non-keplerian orbits. Particles move at sub-keplerian velocities thanks to gas drag, but sufficiently large particles have enough momentum that they are nearly unaffected by this drag. To demonstrate this velocity deviation from Keplerian, we plot it against particle mass in Figure 3.2.2. This deviation becomes significant enough to matter for cores with a core mass of $10^{-15} M_\oplus$ ($R_{\rm core} \approx 100$ m) or less. We also adjust our calculation of the Wind Shearing radius (Perets & Murray-Clay 2011) to include the drag force on both the larger and smaller particle involved in an accretion event.

Next, we update the way that our solid surface density is calculated. As explained in Chapter 2, we follow the work of Powell et al. (2017) and Lambrechts et al. (2014), to calculate the maximum particle size and solid surface density. Our disks naturally shift from the regime described in Lambrechts et al. (2014) to the regime

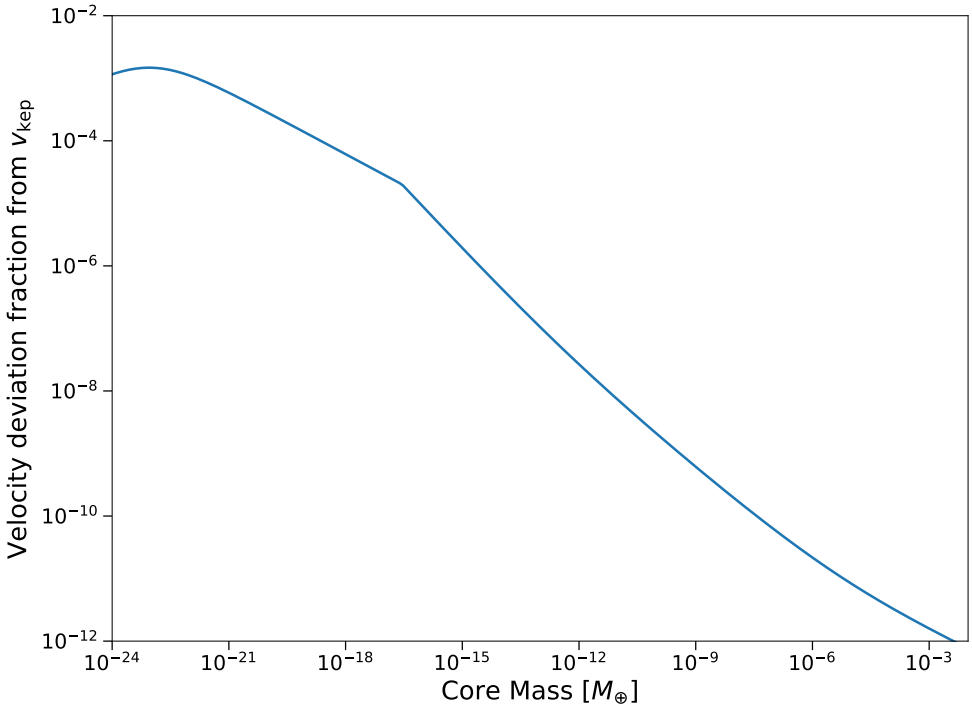

Figure 3.1: The velocity deviation from Keplerian, at a = 10 AU. For the smallest masses, this deviation can be significant.

described in Powell et al. (2017). In each of these two regimes, we use two assumptions to derive the maximum particle size and solid surface density. First, the assumption that the largest particles in the disk have equal drift and growth times is common across the disk regimes. In the regime where we follow the method of Lambrechts et al. (2014), our additional constraint comes from requiring disk continuity, as the surface density in this regime is forced by the particles drifting in from the outer edges of the disk. In the regime which follows the method of Powell et al. (2017), in contrast, the additional constraint comes from setting the drift and growth times equal to the age of the disk. See Chapter 2 for a more detailed explanation of these disk regimes and the transition between them.

Lastly, we implement a probability distribution for the relative velocities between colliding particles. This change is important for a number of reasons. First, the mean relative velocity for these interactions is often quite close to the velocity required to fragment the particles interacting. By using a full probability distribution for the velocities of these particles, we are able to capture interactions with a large probability of growth, which would instead lead to fragmentation if we only use the mean of the distribution. Additionally, the velocity distribution allows a small fraction of particles which are ordinarily moving too quickly to liberate their kinetic energy through gas interactions to still be accreted, thanks to the slower tail of the velocity distribution. By making these three big changes to our model, we expand the parameter space where our model applies, allowing us to examine the effects of gas on particle down to below the meter-scale.

3.3 Rapid Growth Regions

3.3.1 Small planetesimal cores

Having modified and expanded our model to work with smaller planetary cores, we now apply the model, and examine the growth times and flow isolation masses which we predict. After evolving the model presented first in Rosenthal et al. (2018) with the changes described in Section 3.2.2, we can now change the lower radius limit of applicability from around 10^7 cm to below the meter-scale barrier of 10^3 cm. At these new scales, we find that gas-assisted growth can still aid in the growth of budding planetesimals, though in different ways than they do for larger planetesimals. Whereas gas assists in planetesimal growth for higher mass planetesimals (above 10^7 cm) by increasing the cross-section for accretion, at smaller scales it instead contributes to growth by slowing particles so that they can collide without fragmenting. This is true with the exception of a small stip of parameter space, where similarly sized particles are rapidly accreted, thanks to a gas enhanced collision cross-section.

Small cores seem to grow most easily (collide without fragmenting) from like sized particles. This is because the dominant source of relative velocity for particle pairs is usually the Keplerian shear, caused by the different orbital velocities of two particles which interact with the gaseous disk differently (Ormel & Cuzzi 2007). Assuming a Dohnyani size distribution (Dohnanyi 1969), the vast majority (around 95%) of the solid disk mass will be in particles that are roughly the same size. In Figure 3.3.1, we use our model to estimate growth times for pairs of particles. This figure nicely breaks down into regions, which we explain below. Figure 3.3.1 gives a graphical representation

of each of these regions.

For each figure where we predict growth times for planetesimals, we have used the disk TW Hydra as our fiducial disk, to give us both gas and solid surface densities. This disk has a stellar mass of $M_* = 0.8 M_\odot$, a temperature normalization of $T_0 = 82K$, and a gas surface density normalization of $\Sigma_{g,0} = 175 \frac{g}{cm^2}$. We have presented these growth times assuming that a disk age of $t_{\rm disk} = 0.8 Myr$.

The primary effect of varying turbulence levels which we see in Figure 3.3.1 is to change the regions of parameter space where pebble accretion is active. Growth times only change by very small amounts, but increasing the level of turbulence cause the parameter space on the upper right of the figure (smaller protoplanetary cores accreting increasingly like-sized neighbors) to shrink, removing this channel for particle growth.

Whereas varying the turbulence levels in our test disks has little effect on the growth times for particle pairs, the same cannot be said for varying the orbital location in the disk. As particle pairs move further out in the disk, the growth times extend, making it increasingly difficult to rapidly grow planetesimals.

Having presented the growth times for a wide size range of particle pairs, we now explain the different regions of the figure, and the types of growth occuring in each. First, we have the triangle in the top left of the figure, which represents the traditional pebble accretion regime. Here we have large particles (planetesimal sized) rapidly accreting much smaller particles (down to size ratios of 10^{-12}). This region's barriers are defined on the bottom left by the location where $R_{\rm Bondi} = R_{\rm stab}$, and on the bottom right by the location where the smaller particle's relative kinetic energy is

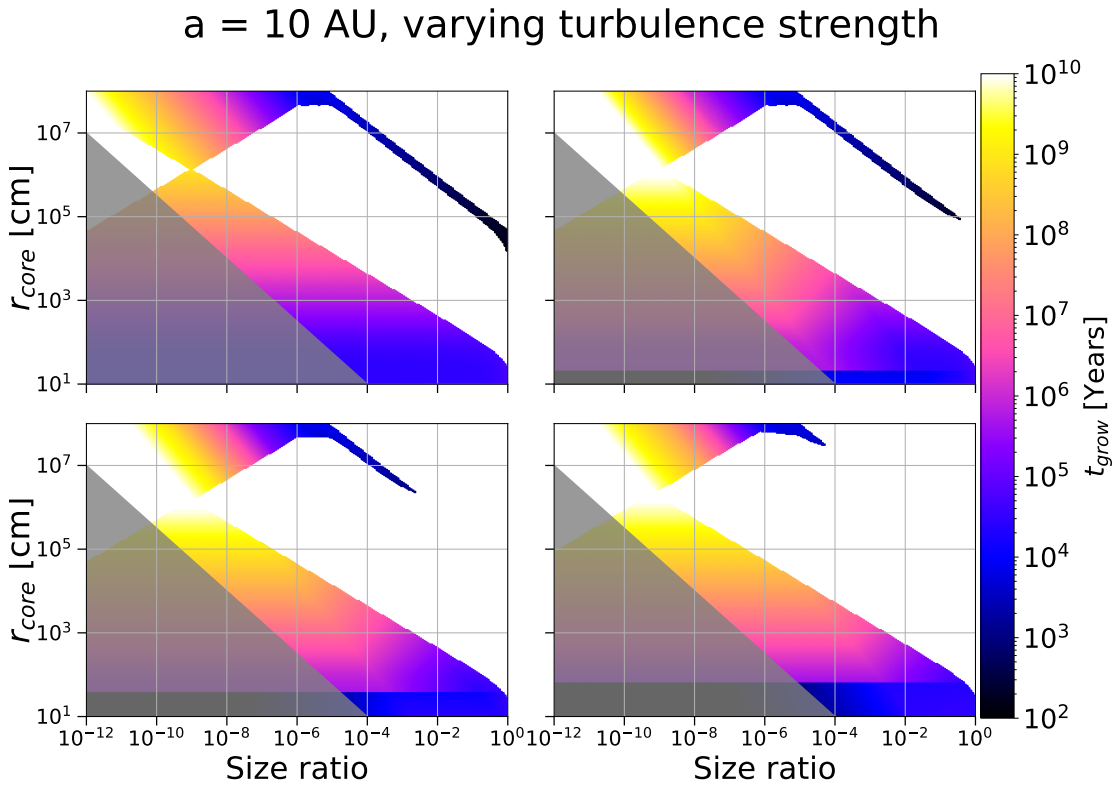

Figure 3.2: The growth times for planetesimals in a sample disk, as a function of particle pair sizes. The y-axis is the planetary core radius, while the x-axis is the size ratio, which is the ratio of the smaller particle radius to the larger particle radius. The four panels (top left to bottom right) show a laminar disk, low turbulence ($\alpha = 10^{-5}$), middling turbulence ($\alpha = 10^{-4}$), and high turbulence turbulence ($\alpha = 10^{-5}$). The region which is greyed out represents growth via particles smaller than the initial ISM grain sizes of 10^{-5} cm, and so we ignore it. Notice how the tail of particularly rapid growth is eaten away by increasingly high levels of turbulence. For each of the growth time plots in this chapter, the assumption is that the entire disk surface density is contained in the particle size under consideration.

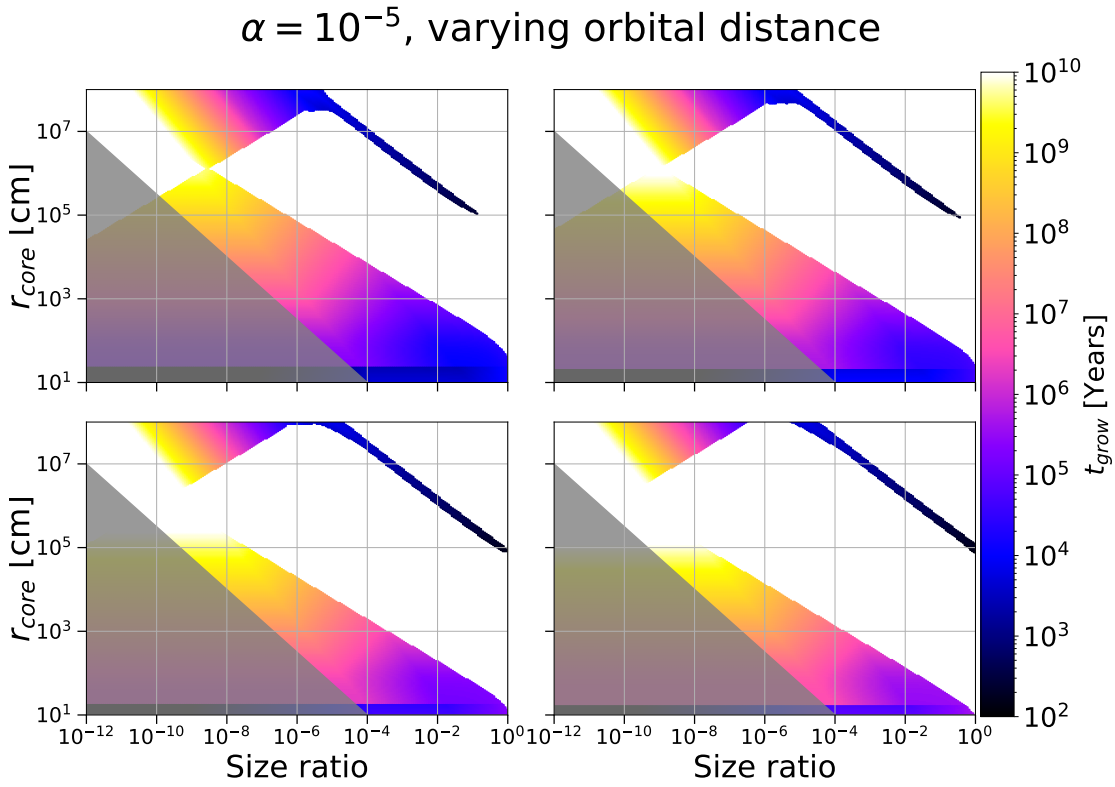

Figure 3.3: The growth times for planetesimals in a sample disk, as a function particle pair sizes. The four panels (top left to bottom right) show a disk at 5, 10, 30, and 50 AU respectively. As with the other growth plots, the greyed out region represents particles smaller than the initial ISM grain sizes, and so it is ignored.

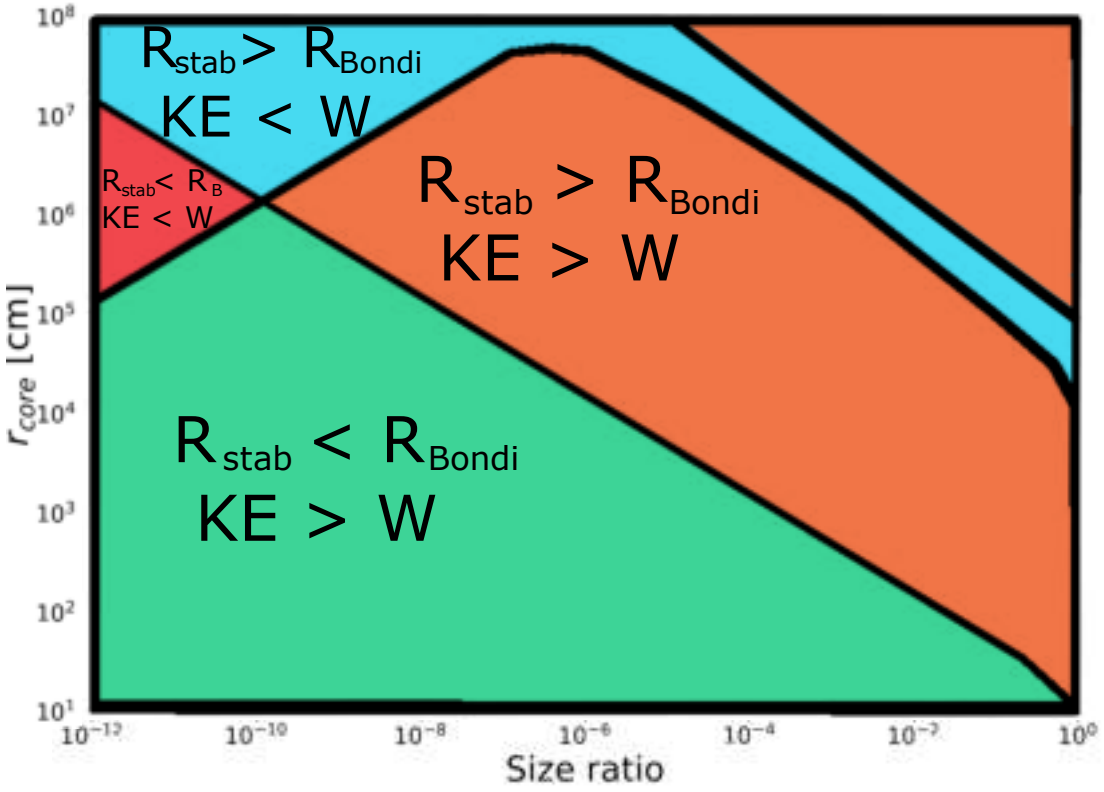

Figure 3.4: The regions of growth for the growth time figures included in this chapter. Blue indicates where traditional pebble accretion is active, and green indicates where pebbles are accreted, but not through the traditional pebble accretion methods. That is, in this region the gas-particle interactions only modify the relative velocity of interactions, while leaving the cross section unchanged. Red indicates where all growth is forbidden by the flow isolation mass, while orange indicates where pebble accretion is forbidden due to energy considerations but traditional gas free core accretion is still possible.

matched by the work done by gas drag on that particle. To the left of this triangle (where the figure is white), particles have less kinetic energy than work done, and $R_{\text{stab}} < R_{\text{Bondi}}$. These particles come to rest with respect to the gas, but the gas flows around the outside of the proto-atmosphere, letting them escape accretion, which is known as flow isolation. To the bottom-right of this triangle, pebble accretion is also off, as here particles have more kinetic energy than the work done by gas drag they experience, and the larger bodies have $R_{\text{stab}} > R_{\text{Bondi}}$. Here, the particles do not lose enough energy from gas drag to fall in sufficiently close to hit the larger body. In this case however, the gas does prevent all types of accretion, still allowing traditional gas free core accretion to occur.

Next, let's focus on the region of extremely rapid growth in the top right of this figure. This strip of very rapid growth which traces from the top-center to the lower-right shows a parameter space where pebble accretion is able to massively reduce the growth times for particle pairs. This is especially true for like-sized particles at lower sizes, where particles can be rapidly grown from just above meter scales to planetesimal sizes extremely rapidly. As mentioned in Figure 3.3.1, this region is largest in the fully laminar disk, and increasingly high levels of turbulence cause this region to less and less important.

Last, there's the triangle at the bottom of the figure. Here, the large bodies have $R_{\text{stab}} < R_{\text{Bondi}}$, and the small particles' kinetic energies exceed the work done by gas drag during their encounter. Here, particles are able to plow through the gas into the larger body's proto-atmosphere until it can inspiral and collide. This region,

extending down to very small particles, shows how we can extend our modeling of growth via pebbles to new scales. As mentioned in Figure 3.3.1, in this regime, the gas interactions modify the inter-particle velocities, but leave the cross sections for interactions unchanged.

3.3.2 The effect of velocity dispersion and gas turbulence

These regions of rapid growth, combined with the reality of a sea of particles with a wide distribution of relative velocities, slowed by their interactions with the gaseous disk, should allow enough large solids to collide with their like-sized partners at favorable velocities, growing past the meter-scale barrier. We model the effect of this distribution of relative velocities by drawing our velocities from a Maxwell-Boltzmann distribution, with its mean set by the combined laminar and turbulent velocities of each pair of particles. In figure 3.3.2, we show the relative velocities for a wide range of particle size, assuming the mean velocity. In figure 3.3.2, in contrast, we present the lowest 10% of these velocities, demonstrating that particles down to the meter scale can occasionally collide with relative velocities slower even than our most conservative estimate for their fragmentation velocity of $1\frac{m}{s}$.

To further illustrate the benefits of this velocity distribution, we remake Figures 3.3.1 and 3.3.1, now instead using the bottom 10% velocity. This allows us to see the benefits of this lower velocity, particularly on expanding the parameter space of possible growth. In Figure 3.3.2, we see how this lower velocity expands the parameter space over which the strip of rapid growth is viable. This suggests a path towards rare solid particle growth through interactions with similarly sized particles. In Figure 3.3.2,

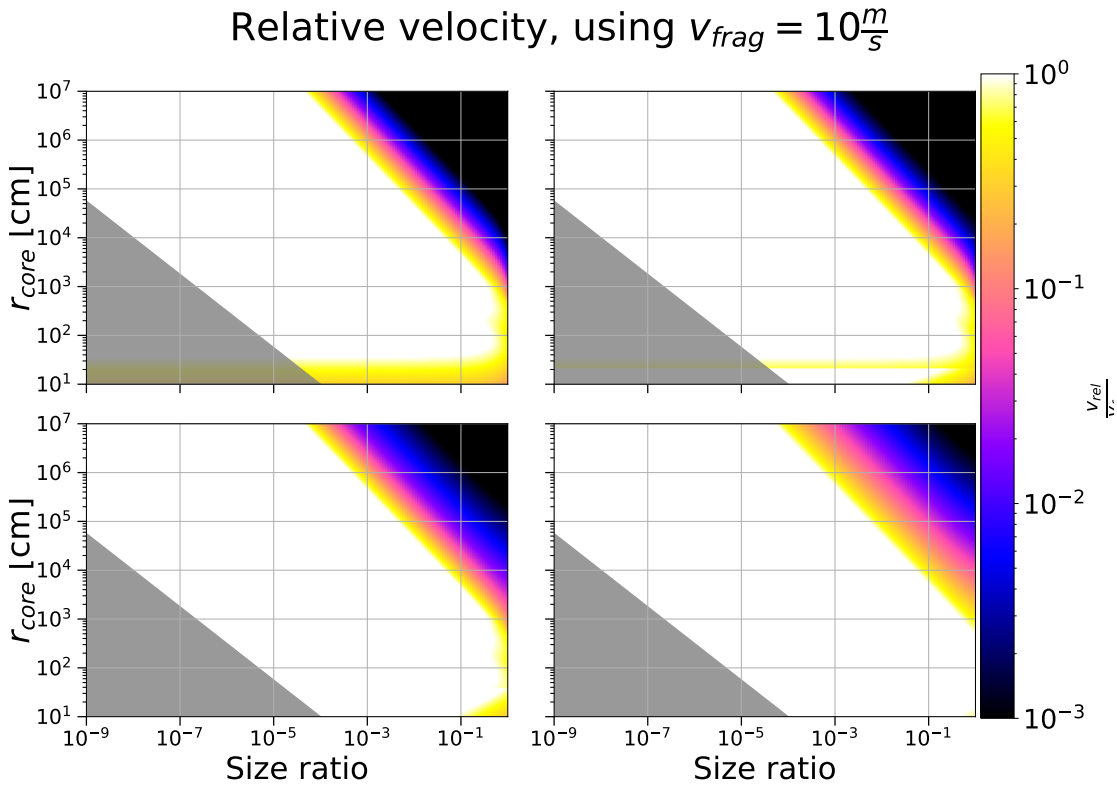

Figure 3.5: The relative velocity for planetesimal growth, divided by a fragmentation velocity of $v_{\text{frag}} = 10\frac{m}{s}$, at a = 10 AU. Note that this fragmentation velocity is only truly applicable for relatively similarly sized particles. The four panels (top left to bottom right) show a laminar disk, low turbulence ($\alpha = 10^{-5}$), middling turbulence ($\alpha = 10^{-4}$), and high turbulence turbulence ($\alpha = 10^{-5}$), and the greyed out region represents growth by particles smaller than the initial dust sizes which we assume ($10^{-}5$ cm). This figure shows that the similarly sized particle pair interactions are unlikely to lead to fragmentation.

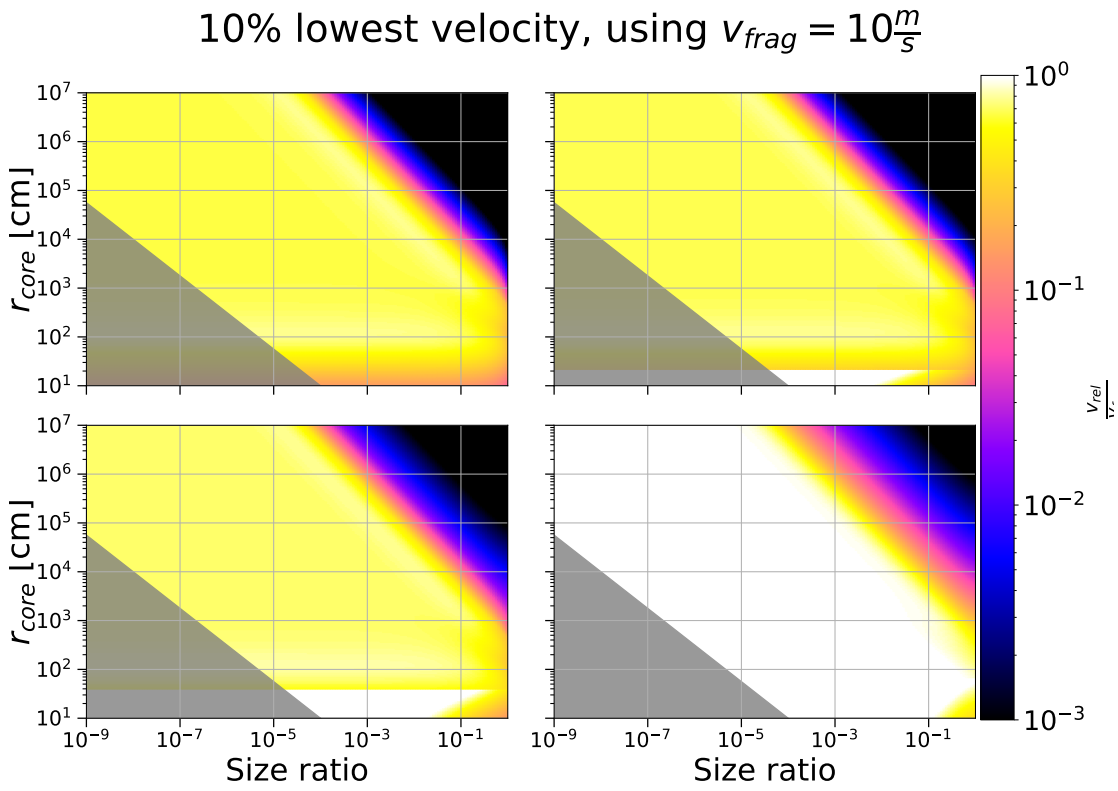

Figure 3.6: The 10% lowest relative velocity planetesimal growth (assuming a Maxwellian velocity distribution), at a = 10 AU. As with the other relative velocity figure, the four panels (top left to bottom right) show a laminar disk, low turbulence ($\alpha = 10^{-5}$), middling turbulence ($\alpha = 10^{-4}$), and high turbulence ($\alpha = 10^{-3}$), and the greyed out region represents growth by particles smaller than the initial dust sizes which we assume ($10^{-}5$ cm). With these lower velocities, it is clear that particle collisions of any size ratio should lead to growth rather than fragmentation.

we see the effect of this lower velocity particularly in the outer disk. Whereas previously moving outwards in the disk only slowed growth, here we see how it maintains the possibility of growth through similar sized particles all the way out to 50 AU. For each of these plots using the bottom 10% relative velocity, we reduce our solid surface surface density by a factor of 10 (increasing our growth time by a factor of 10), as only 1 in 10 interactions will have this favorable low velocity.

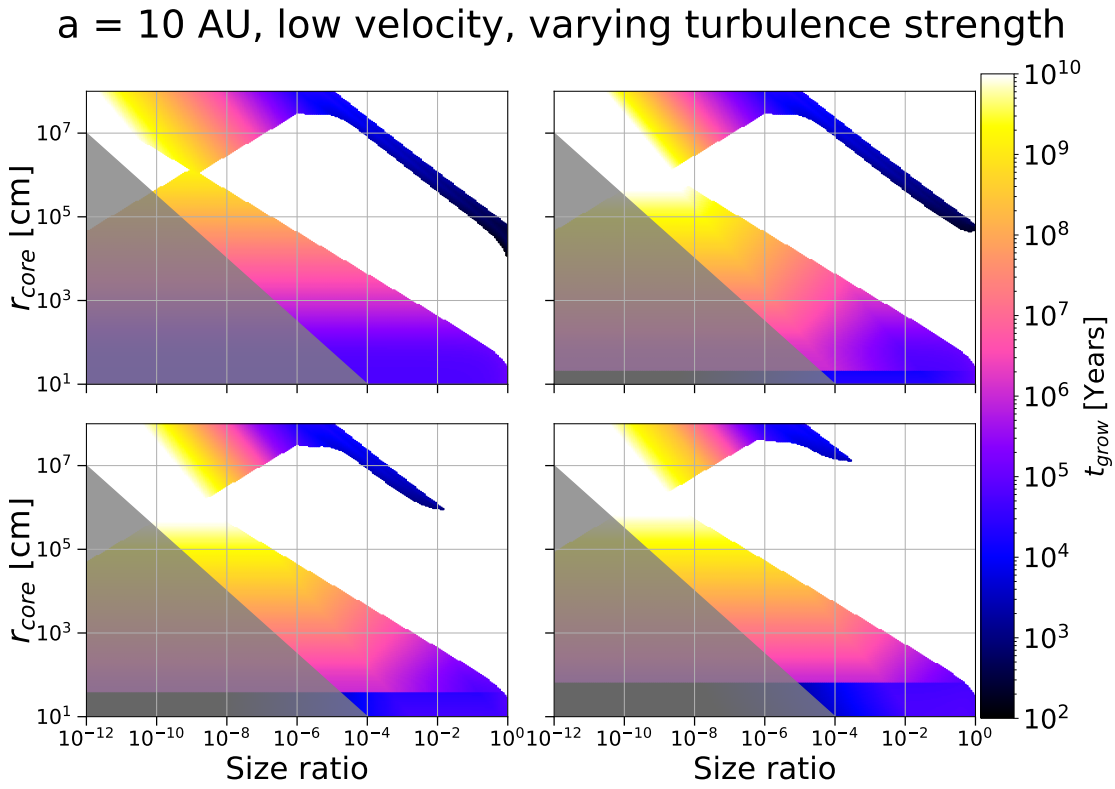

Figure 3.7: The growth times for planetesimals, at a = 10 AU as function of particle pair sizes. Unlike the first two growth time figures, this one uses the 10% lowest relative velocities, drawn from a Maxwellian velocity distribution. As before, the four panels (top left to bottom right) show a laminar disk, low turbulence ($\alpha = 10^{-5}$), middling turbulence ($\alpha = 10^{-4}$), and high turbulence turbulence ($\alpha = 10^{-5}$), and the greyed out region represents growth by particles smaller than the initial dust sizes which we assume ($10^{-}5$ cm). Note how the lower velocity significantly expands the parameter space where the strip of rapid growth is active.

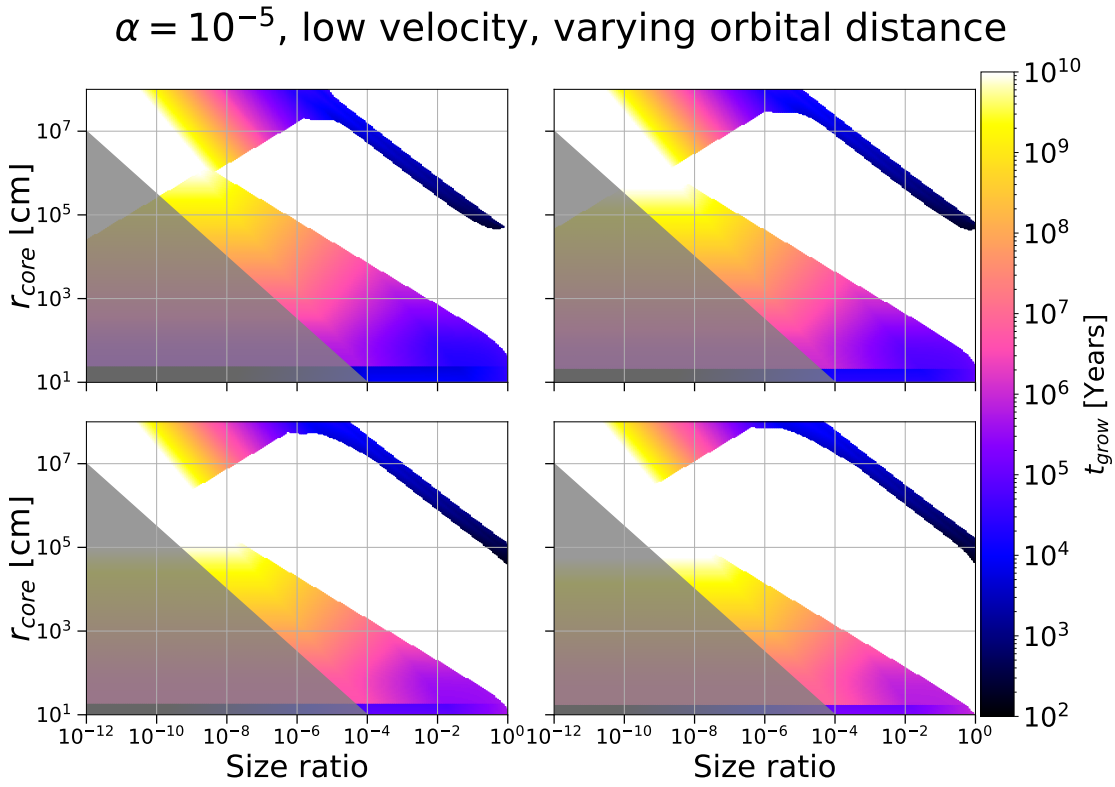

Figure 3.8: The growth times for planetesimals, where $\alpha = 10^{-5}$ as a function of particle pair sizes. Just as with the figure above, this figure uses the 10% lowest relative velocities, drawn from a probability distribution. The four panels (top left to bottom right) show a disk at 5, 10, 30, and 50 AU respectively, and the greyed out region represents growth by particles smaller than the initial dust sizes which we assume ($10^{-}5$ cm). The lower velocity has a dramatic impact here, maintaining the viability of the strip of rapid growth all the way out to 50 AU.

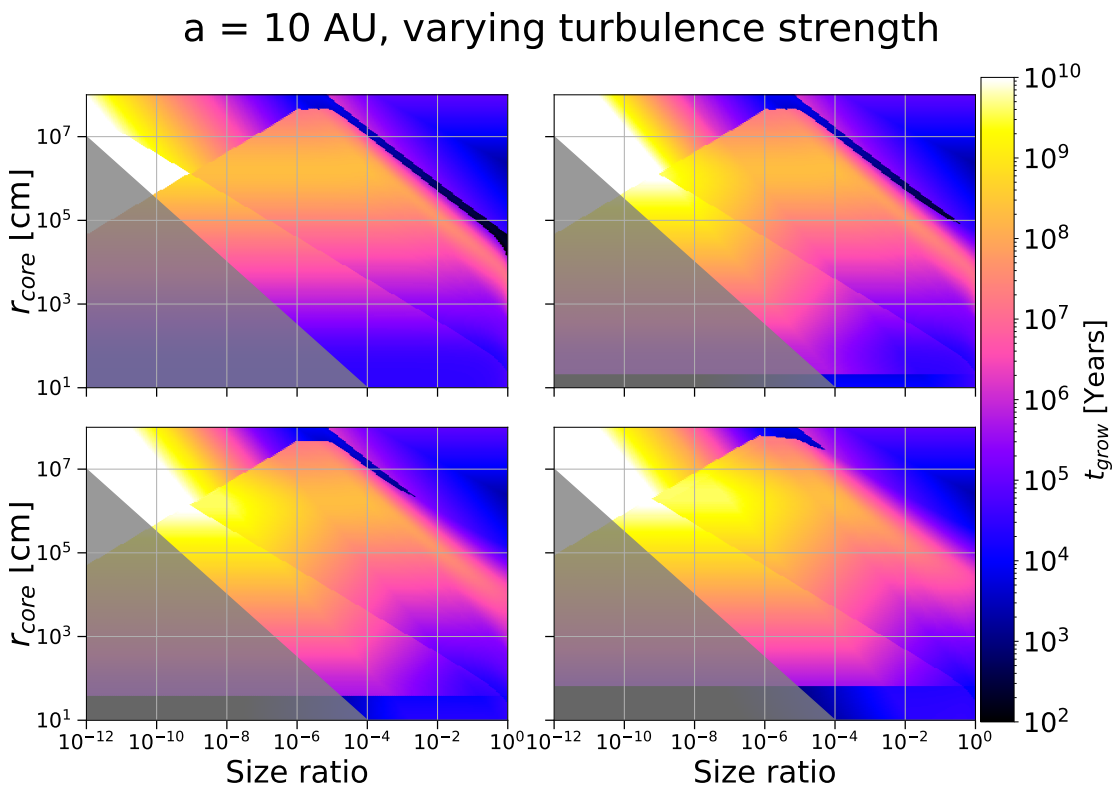

Figure 3.9: The growth times for planetesimals, at a = 10 AU as a function of particle pair sizes. Unlike the other growth time figures, in this figure we include growth time estimates for gas free core accretion, where it allowed by the model. The four panels (top left to bottom right) show a laminar disk, low turbulence ($\alpha = 10^{-5}$), middling turbulence ($\alpha = 10^{-4}$), and high turbulence turbulence ($\alpha = 10^{-5}$), and the greyed out region represents growth by particles smaller than the initial dust sizes which we assume ($10^{-}5$ cm).

Finally, we add in our estimated growth times for classical gas-less core accretion where it is allowed, in Figure 3.3.2. We fill in the regions which were indicated in orange in Figure 3.3.1 with this classical core accretion.

3.4 Results and Conclusions

In this chapter, we have applied our model to a new range of particle sizes, extending our considerations of pebble accretion to new ranges. At these smaller sizes, the gas interactions always will modify the relative velocity of particles during interactions, but it will not always expand the collision cross sections. For the large growth region we identify in green in Figure 3.3.1, the collision cross section collapses to the physical size of the particle. Only in the small strip of favorable accretion in the top right of that figure will gas interactions also expand the cross section for accretion, giving extremely rapid growth. We also demonstrate how the use of a velocity distribution can ensure that growth is possible even with particle size pairs which would otherwise not result in growth. These results suggest that pebble accretion needs to continue to be explored down to the smallest scales available in protoplanetary disks.

Taken together, these results indicate that the particles in the low velocity tail of the probability distribution might allow larger particles to grow past the meter-scale barrier. In this case, we would expect planetesimal cores to grow in a layered manner, with particles in only a small range of sizes being accreted at a time, and the core accreting larger particles as it grows. This prediction is consistent with recent experimental results analyzing particle sizes on the surface of asteroids (e.g. Hayabusa2).

3.4.1 Future work

As we suggested in the previous chapter, this work would benefit greatly from coupling to a more advance particle evolution code. With a particle evolution code to

supply us with particle sizes, we could use this work to predict growth rates, which could then be verified with the numerical model. Additionally, a more thorough examination of the role of turbulence, beyond the Kolmogorov model, could provide more insight into growth at these small scales.

In order to validate the prediction that we may grow past the meter-scale barrier with rare favorable accretion events, we would also want to repeat this study with more precision. This chapter and the last rely on order of magnitude models, but this prediction merits a more exact approach in the future, to both verify and refine the prediction.

Chapter 4

Constraining Type Iax Supernova Progenitor Systems with Stellar Population Age-dating

4.1 Introduction

Type Iax supernovae (SNe Iax) are a class of peculiar SNe which share some characteristics with Type Ia SNe, but appear to be physically distinct (Foley et al. 2013). SNe Iax are also known as SN 2002cx-like SNe, after the prototypical object of the class (Li et al. 2003; Jha et al. 2006; Jha 2017). These SNe are principally characterized by their low luminosities (as compared to SNe Ia), low photospheric velocities, a lack of a secondary maximum in near-IR bands (Li et al. 2003), and their unique late-time spectra (e.g., Jha et al. 2006; Foley et al. 2016). In contrast to SNe Ia, SNe Iax reach

their peak brightness in optical bands before they do in the near-IR.

SNe Iax are the most common type of peculiar SN, occurring at roughly 30% the rate of SNe Ia (Foley et al. 2013; Miller et al. 2017). This, along with their observational similarities with SNe Ia, means that investigating the physical properties of these supernovae is extremely helpful to understanding SNe Ia. The comparably low photospheric velocities of SNe Iax makes line identification easier, allowing for precise measurements of the explosion in these events, which can help us to understand the physics involved in both SNe Iax and Ia. This will be crucial as we look to improve our knowledge of SNe Ia in order to continue to perform precision cosmology. Despite decades of study of SNe Ia, the identity of the binary companion to the SN Ia progenitor is still unknown. By first learning about the progenitor system for SNe Iax, we may be able to shed some light on this long-standing problem.

As compared to typical SNe Ia, SNe Iax are also inferred to have much lower explosion energies (Branch et al. 2004), and lower ejecta masses (Foley et al. 2013) (though this has been debated for some members of the class, e.g., Sahu et al. 2008, Stritzinger et al. 2015, Yamanaka et al. 2015). Additionally, SNe Iax tend to have a layered structure in their ejecta, similar to SNe Ia. In contrast to SNe Ia, however, there is evidence of Ni mixing in at least two SNe Iax, further from the center than in standard SNe Ia (Jha et al. 2006; Phillips et al. 2007; Stritzinger et al. 2015). Finally, at least six SNe Iax show cobalt in their near-IR spectra (Kromer et al. 2013; Stritzinger et al. 2014, 2015; Tomasella et al. 2016). Taken together, these properties suggest that SNe Iax may be the result of the partial deflagration of a white dwarf (WD) (e.g. Foley

et al. 2010a; Kromer et al. 2013; Fink et al. 2014; Magee et al. 2016).

SNe Iax host galaxies are also markedly different from SNe Ia host galaxies. While the SNe are nearly always found in late-type galaxies, there is one example (SN 2008ge) of a SN Iax in an S0 galaxy (Foley et al. 2010b). Lyman et al. (2013) and Lyman et al. (2018) find evidence of star forming regions near the sites of most SNe Iax, suggesting a young progenitor age at the time of explosion for these events. Additionally, SNe Iax seem to preferentially occur in metal-poor regions of their host galaxies (Lyman et al. 2018). This is quite different from the metallicity of the explosion sites for SNe Ia, instead matching quite closely with the sites of SNe Ib, Ic, II, and IIb. Though the metallicities of the explosion sites for SNe Iax and core-collapse SNe are similar, they appear quite different from those of low-redshift long gamma-ray bursts (LGRBs; Levesque et al. 2010). This is particularly interesting, as the most popular core collapse model for SNe Iax is the "fallback SN" model (Valenti et al. 2009; Moriya et al. 2010), which are theorized to occur alongside LGRBs (Heger et al. 2003; Della Valle et al. 2006). Thus the divergent metallicity distributions of SNe Iax and LGRBs suggest that SNe Iax may not be "fallback" core-collapse SNe.

The physical origin of SNe Iax is still uncertain, but the leading models suggest that they are the result of binary interactions between a carbon-oxygen WD and a He-star companion (Foley et al. 2013; Jha 2017). These interactions seem to result in an incomplete deflagration (sub-sonic nuclear burning, Phillips et al. 2007) of the WD which may not completely unbind the star (e.g., Jordan et al. 2012; Kromer et al. 2013; Fink et al. 2014; Long et al. 2014; Magee et al. 2016). The low luminosities,

velocities, and ejecta masses measured from these events together give strong indirect evidence for a WD progenitor system (Foley et al. 2009, 2010a). Additionally, the Ni mixing observed in some SNe Iax ejecta can be most easily explained by a turbulent deflagration in a WD (Röpke 2005). Despite the mounting evidence for this model, there remain several unresolved issues. Specifically, the incomplete deflagration model struggles to reproduce the observed lower luminosity SNe Iax, such as SNe 2008ha and 2010ae (Kromer et al. 2013; Fink et al. 2014) It has also been argued (Kromer et al. 2015) that SN 2008ha spectra are indicative of poorly mixed ejecta, in contrast to brighter SNe Iax. Well-mixed ejecta are a hallmark of partial deflagration models, making SN 2008ha particularly confusing. Additionally, at least two SNe Iax (SNe 2004cs and 2007J) have He lines in their spectra, which is difficult to reproduce with the WD and He-star binary model (Fink et al. 2014).

For the WD He-star binary progenitor model for SNe Iax, it is expected that the circumstellar environment will be enriched by pre-SN mass loss, either from winds from the He donor star, or from non-conservative mass transfer. Once the WD explodes, the interaction between the blast wave and the circumstellar material should power X-ray and radio emission (Chevalier & Fransson 2006; Immler et al. 2006; Russell & Immler 2012; Margutti et al. 2012, 2014). Though X-ray emission has not yet been detected from any SNe Iax, Liu et al. (2015) use X-ray upper limits from seven SNe Iax (Russell & Immler 2012) to constrain their pre-SN mass loss rates. In comparing theoretical pre-SN mass loss rates to the observed X-ray upper limits, they find broad agreement between these upper limits and single degenerate models for SNe Iax, across a variety of

models for the X-ray emission. However, using only these upper limits, they are unable to distinguish between a WD He-star binary progenitor and a WD main sequence star binary.

The WD He-star binary model for SNe Iax has also been tested with pre-explosion *Hubble Space Telescope* (*HST*) imaging of the locations of SN 2008ge (Foley et al. 2010b), SN 2008ha (Foley et al. 2014), SN 2012Z (McCully et al. 2014a), and SN 2014dt (Foley et al. 2015). These works use precision astrometry to align pre-explosion images with ground-based images of the SN. The authors then perform photometry on the pre-explosion images at the site of the explosion to probe the progenitor system just before explosion. In doing so, they find an upper bound on the progenitor mass for SN 2008ge (assuming a massive star progenitor), find an upper bound on the age of the SN 2008ha progenitor system, and resolve the likely progenitor system of SN 2012Z. Foley et al. (2015) find no progenitor system for SN 2014dt down to quite deep limits ($3-\sigma$ limits of $M_{F438W} > -5.0$ mag and $M_{F814W} > -5.9$ mag), making the interpretation of SN 2014dt as a core-collapse event less likely. While these limits rule out most Wolf-Rayet star models, there are some Wolf-Rayet star models which remain below the detection limits. In all four cases, the results show consistency with the WD and He-star model, though the large photometric errors involved prevent them from ruling out other models with high certainty.

The likelihood of observing a WD progenitor in pre-explosion imaging of SN Iax explosion sites is quite low, due to the inherent low luminosity of WDs as compared to their mass donor companion. However, analyzing the host environments of SNe (in

pre or post-explosion imaging) has been quite successful in extracting information on the progenitors of Type Ib, Type Ic, and Type II SNe (e.g., Maíz-Apellániz et al. 2004; Badenes et al. 2009; Kuncarayakti et al. 2013a,b). One such method uses resolved stellar populations near the SNe to constrain the age of the SN progenitor (or SN remnant) (e.g., Gogarten et al. 2009; Murphy et al. 2011; Jennings et al. 2012; Williams et al. 2014; Jennings et al. 2014). In this method, it is assumed that the resolved stellar population and the progenitor itself formed nearly simultaneously, in a single burst of star formation. This method of aging stellar populations to measure time between star formation and explosion – known as the delay-time – for SNe has only been effective for SNe with relatively short delay times, as typical open cluster velocity dispersions are large enough that stellar positions are no longer correlated after a few hundred million years (Bastian & Goodwin 2006; Lada 2010). Every model for SNe Iax predicts a delay-time distribution (DTD) with non-zero probability down to below 100 Myrs, so it is reasonable to apply this method to measure SNe Iax delay times.

In the WD progenitor model for SNe Iax, explosions occur at the Chandrasekhar mass, and the quickest binary channel for a carbon/oxygen (C/O) WD is to accrete helium from a He star companion (Hachisu et al. 1999; Postnov & Yungelson 2014). The stable mass transfer rate can be high for helium accretion, and Claeys et al. (2014) show that this channel dominates the thermonuclear SN rate between 40 Myr and 200 Myr (above which traditional SNe Ia dominate). This has been observed in several binary population synthesis studies (Ruiter et al. 2009, 2011; Wang et al. 2009a,b; Meng & Yang 2010; Piersanti et al. 2014; Liu et al. 2015). Liu et al. (2010)

present a model (originally intended to explain a different kind of system) that begins with a 7 $M_\odot$ + 4 $M_\odot$ binary system that undergoes two phases of mass transfer and common envelope evolution, before resulting in a 1 $M_\odot$ C/O WD + 2 $M_\odot$ He star. As the He star evolves, it again fills its Roche lobe and begins stable mass transfer onto the white dwarf that could lead to the SN Iax. The high accretion rate involved in this process mean that total delay time is dominated by the stellar evolution timescale of the secondary, giving short expected delay times for these models.

In this work, we employ Bayesian Monte Carlo methods to fit isochrones to the stellar populations around SNe Iax, in order to accurately measure the DTD of this class of SNe. With a sample of nine SNe Iax, we constrain the ages of these systems at the time of explosion.

Li et al. (2018) examine the location of SNe Iax in their host galaxies, and find that they tend to occur at much larger projected radii as compared to SNe Ia. The authors perform a Kolmogorov-Smirnov test to compare the fractional host galaxy fluxes at the explosion sites for SNe Iax, SNe Ia, and SNe Ib/Ic. They find strong evidence that SNe Ia and SNe Iax are drawn from different populations, while also finding that they cannot reject the hypothesis that SNe Iax and SNe Ib/Ic are drawn from the same fractional host galaxy flux distribution. Taken together with the metallicity information, this suggests that the delay-time for SNe Iax might be much more similar to those of core-collapse SNe than the delay-times measured for SNe Ia.

This chapter is structured in the following way. In Section 4.2, we describe the observations used in this study, and the methods to extract photometry of the stellar

populations near each SN. In Section 4.3, we detail the Bayesian Monte Carlo methods used to probabilistically determine the ages of these stellar populations. We discuss the particulars of each SN individually in Section 4.4, describing the priors used in the fit and the resulting posterior distributions. In Section 4.5, we discuss the overall properties of the measured DTDs for this sample of SNe Iax, and describe how our results compare to theoretical models for this class of SN.

4.2 Observations and Data Reduction

4.2.1 Sample Selection

Our sample is composed of all SNe Iax with HST imaging of their host galaxies that can sufficiently constrain the age of the stellar population at the SN position. Four SNe in the sample (SNe 2008ge, Pignata et al. 2008; 2008ha, Foley et al. 2009; 2010ae, Pignata et al. 2010; and 2010el, Monard 2010) were specifically targeted for this purpose as part of *HST* program GO-12999. At the time of that program, these were the four closest SNe Iax (all with $D \lesssim 20$ Mpc) where we expected to be able to resolve individual stars in the images. These four objects were observed with the Advanced Camera for Surveys Wide Field Channel (ACS/WFC), with the F435W, F555W, F625W, and F814W filters. These bands were chosen because they provide good colors for observing broad spectral types, and their spectral range enables one to correct for extinction due to dust in the local environment.

In the time since 2013, we have searched the *HST* archive for other SNe Iax with high quality data (wide spectral range and long exposures) of their stellar neigh-

borhoods. This search added SNe 2008A (GO-11590: Jha, S.), 2011ay (GO-15166: Filippenko, A.), 2012Z (GO-10497: Riess, A.; GO-10711: Noll, K.; GO-10802: Riess, A.; and GO-13757: Jha, S.), 2014ck (GO-13029: Filippenko, A.), and 2014dt (GO-13683: Van Dyk, S.; GO-14779: Graham, M.) to our sample. Two of these objects have ACS/WFC imaging, with SN 2012Z imaged in the F435W, F555W, and F814W bands, and SN 2008A imaged in the F555W, F625W, and F775W bands. SN 2011ay and SN 2014ck each have Wide Field Camera 3 (WFC3) imaging, in the F555W and F814W bands, and the F625W and F814W bands, respectively. Additional imaging of SNe 2010el was added in this search (GO-13364: Calzetti, D.; GO-13816: Bentz, M.; GO-14668: Filippenko, A.; and GO-15133: Erwin, P.). Finally, our 2015 follow-up *HST* program for SN 2008ha (GO-14244: Foley, R.) provided additional imaging in the F435W and F814W filters.

Our complete sample of SNe Iax contains all observed SNe Iax within 35 Mpc, for which *HST* host galaxy imaging is deep enough to find strong constraints on progenitor age. In addition, two more distant SNe (2008A and 2011ay) are included in the sample, thanks to the abundance of *HST* imaging of their host galaxies. In these cases, the images are generally deeper and the SNe are isolated, allowing us to apply our analysis method to these data. SNe 2008A, 2008ge, 2008ha, 2010ae, 2010el, 2011ay, 2012Z, 2014ck, 2014dt compose our sample. The complete list of data can be found in Table 4.1. Of these, previous works have found constraints on the progenitors of SNe 2008ge, 2008ha, and 2012Z. These constraints were achieved through pre-explosion *HST* imaging of the sites of SNe 2008ge (Foley et al. 2010b) and 2012Z (McCully et al. 2014a),

and post-explosion imaging of the site of SN 2008ha (Foley et al. 2014), with claims of detections of either the remnant, or the probable donor star for both SN 2008ha and SN 2012Z.

Note that for host galaxy distances which are measured using redshift, we assume $H_0 = 73.24 \pm 1.74$ km Mpc^{-1} s^{-1} (Riess et al. 2016). The distances to each object, as well as the methods with which these distance were measured, can be found in Section 4.4. Additionally, the Milky Way reddening is assumed to follow the extinction maps of Schlafly & Finkbeiner (2011), using $R_v = 3.1$ (Cardelli et al. 1989). This reddening is applied to all simulated data to match the observations.

4.2.2 Data Reduction

To build catalogs from the *HST* observations, we use a custom pipeline written primarily in `Python`[1]. The pipeline initially registers the astrometry to a ground-based image which has a wider field of view than the *HST* images. The World Coordinate System (WCS) from the ground-based image is considered to be the global astrometric solution. This stage typically produces a precision of $\sim 0.05''$ which corresponds to roughly one *HST* pixel for ACS.

Ground Based Data

We use ground based images for astrometric alignment of the *HST* images of SNe 2010ae, 2010el, and 2011ay. The *HST* images of SN 2011ay are aligned to photometry from the 1.2 m telescope at the F. L. Whipple Observatory (Foley et al.

[1] https://github.com/cmccully/snhst

2013). Images of SNe 2010ae and 2010el were obtained on 2011 March 6 UT with the IMACS spectrograph (Dressler et al. 2011) on the Magellan Baade 6.5 m telescope, roughly 1 year after discovery for each SN. For SN 2010ae, we obtained two 120-second dithered pairs of 1×1-binning images in *griz*. SN 2010el had similar observations, except we obtained three images in *irz*.

The images were reduced using the `photpipe` data-reduction pipeline (Rest et al. 2005, 2014). All CCD images are de-biased, trimmed, and masking was applied to bad pixels and columns. The mask is propagated through all subsequent reduction stages. All science images are flat-field-corrected using dome flats. The transformation between the local image pixel coordinate system and the FK5 World Coordinate System is dominated by optical distortions that are well described by a low-order polynomial in radius from the field center. We determined these polynomial terms from images of dense field using the IRAF task `msctpeak`. The distortion terms were then used in combination with the IRAF task `msccmatch` to derive a WCS solution for each image, with 2MASS as the reference catalog. Finally, we used the astrometric solution and the SWarp (Bertin et al. 2002) package to re-sample each image to a common pixel coordinate system using a flux-conserving, Lanczos-windowed sinc kernel. The fully reduced images were then used as the astrometric reference for the *HST* images. These astrometric solutions yield a precision of $\lessapprox 0.15''$.

HST Data

In this study, we align to other HST images for SN 2008A (McCully et al. 2014a), SN 2008ge (Foley et al. 2010a), SN 2008ha (Foley et al. 2009), SN 2012Z (Mc-

Cully et al. 2014b), SN 2014ck (Tomasella et al. 2016), and SN 2014dt (Foley et al. 2015). For these objects, the precision is better than 0.05″ (one *HST* pixel).

After solving for the global WCS, we refine the registration between individual exposures, starting from the flat-fielded frames from the MAST archive[2]. For ACS and WFC3, we use the FLC frames that have been corrected for charge-transfer inefficiency (CTI) using the pixel-based method (Anderson & Bedin 2010). Cosmic rays are rejected from the individual frames using `Astro-SCRAPPY`[3] before the registration process to alleviate false positives in the catalog matches. After doing a coarse registration between *HST* visits by hand, the pipeline uses TweakShifts from `Drizzlepac`[4] (STSCI Development Team 2012) to refine the offsets between frames.

Once the registration is completed, we combine the exposures using `Astrodrizzle` adopting standard values for the parameters[4]. We include the cosmic-ray step in `Astrodrizzle` to do final cosmic-ray rejection. For cases that we have more than 4 individual exposures in the same filter for a target, we subsample the pixel grid and decrease the drizzle pixel coverage fraction to 0.8.

To build the final catalogs, we run `DOLPHOT`, a modified version of HSTPhot (Dolphin 2000), using the drizzled image as a coordinate reference. `DOLPHOT` runs on the individual flat fielded frames and stacks the photometry to produce the final catalog, including all point sources across the entirety of each image. We again use the CTI-corrected FLC frames for ACS and WFC3/UVIS. For WFPC2, we use the CTI correction built into `DOLPHOT`. `DOLPHOT` includes its own image registration stage which

[2] https://archive.stsci.edu/
[3] https://github.com/astropy/astroscrappy
[4] https://drizzlepac.stsci.edu

generally produces a scatter of $\sim 0.01''$. Finally, we inject artificial stars using DOLPHOT to estimate the brightness limit of our images.

4.2.3 Star Selection

Using the DOLPHOT output from the image combined across filters, we apply the recommended cuts in sharpness (¡0.3), roundness (¡1), and crowding (¡0.1), along with a minimum signal-to-noise ratio of 3.5. Though this removes most non-stellar detections, there remain a number of clusters and bright clumps of gas which are selected as stars by DOLPHOT. As such, for each region surrounding a SN, every detected source within the region is checked by eye to ensure that it has a point spread function indicative of a single stellar source. This allows us to remove gas clumps from our catalogues.

As the human eye struggles to distinguish distant clusters from stars in the galaxy under examination, another method is used to make this distinction. Aperture photometry is performed using IRAF in order to determine a concentration parameter for each source (Chandar et al. 2010). The concentration parameter gives the difference in measured F555W (or a similar band) magnitude between when a 3 pixel aperture is used, and when a .5 pixel aperture is used. By separating on this concentration parameter, as detailed in Chandar et al. (2010), we remove the extended sources from our sample, leaving us with only sources that have a high likelihood of being stars.

In order to check that this cut on the concentration parameter does not bias the results of this study, the full analysis is performed without computing the concentration parameter. While this new analysis does give slightly different values of delay-time for an individual SN, the delay-time distribution for all of the objects together is qualitatively

similar to that of the standard analysis. This indicates that the concentration cut is not biasing our results, so we follow the literature, and use the analysis with a concentration cut for the remainder of this study.

4.3 Isochrone Fitting Method

In order to determine the age of a supernova progenitor in in post-explosion host galaxy images, we assume a star formation history (SFH) characterized by a dominant star formation event for the region in which the progenitor system formed. We also assume a typical scale within which we can reasonably expect nearly every star examined to have a shared SFH. Past work has indicated that this radius is anywhere from 50 pc to 200 pc (Bastian & Goodwin 2006; Eldridge et al. 2011; Williams et al. 2014; Foley et al. 2014; Maund & Ramirez-Ruiz 2016; Maund 2017, 2018). To account for this uncertainty, we consider all stars within a 200 pc projected on-sky radius of the SN position, weighting the stars according to their probability of being associated with the SN.

To estimate the probability of association as a function of on-sky distance, we build a probability distribution as follows. We first assume a flat initial distribution of stars within 100 pc of the SN, to represent the cluster at the time of formation. We then assume a velocity dispersion of 0.65 km/s (Geller et al. 2009), multiplied by the age of the cluster (in this case the delay-time being tested), to model the cluster spreading out over time. To "apply" this spreading effect to the initial flat distribution, we convolve the two distributions. This convolution of the two distributions gives us a rough probability

of association with the SN as a function of projected physical distance. This probability function is used to weight the stars within 200 pc, with the higher probability stars receiving a higher weight in the fitting scheme. We fit a single stellar population model to each of these populations.

Geller et al. (2009) quotes a velocity dispersion for clusters of 0.65 ± 0.10 km/s. To account for this uncertainty, we run our complete analysis using dispersions of 0.55 km/s, 0.65 km/s, and 0.75 km/s. Each of these choices ultimately leaves the final PDF in delay time largely unchanged. For this reason, we use the median value of 0.65 km/s in all the analyses that follow.

Maund (2017) uses a similar technique to age the stellar population around the positions of 12 Type IIP SNe. In that chapter, however, they fit to multiple stellar populations for each SN, allowing for multiple bursts of star formation in the SFH. In this study, we choose to only fit a single stellar population around each SN, as the errors in magnitude and color for our detected stars are large enough that fitting to multiple populations would result in overfitting.

4.3.1 Color Magnitude Diagrams

To date the regions around the SNe, we use the magnitudes and colors derived using `DOLPHOT` to place each star on a color magnitude diagram (CMD). We then overplot the `MIST` synthetic photometry isochrones (Paxton et al. 2011, 2013, 2015; Dotter 2016; Choi et al. 2016), corrected for distance, metallicity, and extinction. We test isochrones in the age range $10^{6.5}$ to $10^{8.5}$ years. These isochrones assume single stellar evolution, and standard rotation ($\frac{v}{v_{\rm crit}} = 0.4$). For metallicity and extinction, we test the 2-σ range

from our priors. One sigma errors in distance and internal (host galaxy) reddening are propagated through to color and magnitude, added in the appropriate way and displayed in CMDs as shaded regions.

One limitation of our method is that we use isochrones for single stellar models, even though we expect that the stellar populations which we are examining will feature both single and binary stellar systems. To resolve this, one could perform a similar analysis to ours, using binary stellar models, such as those presented by the Binary Population and Spectral Synthesis (BPASS) group (Eldridge et al. 2017). This is unlikely to have a major effect on the results of this study, as we focus on the brightest stars in the region surrounding a SN. These brightest stars see minimal differences between single and binary stellar models, with the primary differences arising from color changes, rather than overall luminosity. As magnitude plays a larger role than color in our fitting procedure, this should have only a minor effect on our results.

4.3.2 Isochrones

In order to fit the synthetic photometry isochrones to the detected stars accurately and with well understood errors, a hierarchical Bayesian framework is used to create a new statistic to measure the goodness of fit[5] between the isochrones and the detected stars. Monte Carlo methods are then used to translate this statistic into a probability that the stellar population was drawn from the isochrone. This is performed for each isochrone, generating a probability distribution for the data as a function of system age, metallicity, host galaxy extinction, and distance to host galaxy. The re-

[5] https://github.com/TTakaro/Type-Iax-HST

sulting probability distributions are then marginalized over three of these variables, to obtain a one dimensional probability distribution as a function of stellar population age.

Table 4.1: The list of observations used in this study. The data can be found here: http://dx.doi.org/10.17909/t9-qr61-xb59

SN Name	Host Galaxy	Distance (Mpc)	Instrument	Filters	Exposures per Filter	Total Exposure Lengths (sec)	Observation Date (UTC)
2008A	NGC 624	51.5 ± 11.0	ACS/WFC	F555W, F625W, F775W	6, 6, 4	3750, 3530, 2484	08/18/2009
”	”	”	WFC3/IR	F110W	12	8336	08/18/2009
2008ge	NGC 1527	17.37 ± 0.96	ACS/WFC	F435W, F555W	2	1168, 768	10/26/2012
”	”	”	”	F625W, F814W	2	844, 1244	”
2008ha	UGC 12682	21.3 ± 1.5	ACS/WFC	F435W, F555W	2	9068, 764	01/2013, 12/2015
”	”	”	”	F625W, F814W	2	840, 12058	”
2010ae	ESO 162.17	11.09 ± 1.02	ACS/WFC	F435W, F555W	2	1402, 1002	05/23/2014
”	”	”	”	F625W, F814W	2	1078, 1478	”
2010el	NGC 1566	5.63 ± 1.12	ACS/WFC	F435W, F555W	2	1168, 768	05/23/2013
”	”	”	”	F625W, F814W	2	844, 1244	”
”	”	”	WFC3/UVIS	F275W, F336W, F438W	3, 3, 3	2382, 1119, 965	09/2013, 07/2015
”	”	”	”	F555W, F814W	5, 5	1853, 1769	08/2017
2011ay	NGC 2315	87.4 ± 6.4	WFC3/UVIS	F555W, F814W	2	780, 780	01/20/2018
2012Z	NGC 1309	31.92 ± 0.88	ACS/WFC	F435W, F555W, F814W	8, 10, 10	9624, 12642, 12868	09/2006
2014ck	UGC 12182	24.32 ± 1.69	WFC3/UVIS	F625W, F814W	2	510, 680	02/22/2013
2014dt	Messier 61	19.3 ± 0.6	WFC3/UVIS	F275W, F438W	2, 20	858, 400	02/2017, 11/2014

In analogy to a Chi-squared fit, this statistic (which we will hereafter call IGoF for "Isochrone Goodness of Fit") measures the minimized magnitude difference in each filter between the stars detected and the isochrone under consideration. The magnitude difference in each filter is then summed in quadrature. Summing over each detected star, IGoF gives a total distance from the stars to the isochrone in n-dimensional magnitude space, where n is the number of filters. As described in the previous section, each star is weighted in IGoF according to its projected physical distance from the SN, and thus its likelihood of forming simultaneously with the SN progenitor system. This statistic was selected in part because of its qualitative similarity to a Chi-squared fit, allowing for relatively intuitive analysis.

The equation for IGoF is shown below.

$$\mathrm{IGoF} = \frac{\sqrt{\sum_i \mathrm{PhysDist}_i \cdot min(\sum_k (m_{ik} - m_{\mathrm{Iso.},k})^2)}}{\sum_i \mathrm{PhysDist}_i}, \tag{4.1}$$

$$\begin{aligned} \mathrm{PhysDist} = \mathrm{U}(min = 0\mathrm{pc}, max = 100\mathrm{pc}) \circledast \\ \mathrm{N}(\mu = 0, \sigma = 0.65 \frac{\mathrm{km}}{\mathrm{s}} \cdot \mathrm{Age}), \end{aligned} \tag{4.2}$$

where i specifies a given star, k specifies a given filter, m_{ik} is the magnitude of a given star in a filter, $m_{\mathrm{Iso},jk}$ is the magnitude drawn from the isochrone, adjusted for distance, milky way reddening, and host galaxy reddening. $\mathrm{PhysDist}_i$ is the weight given to the star i according to its physical distance from the SN. As detailed in section 4.3, this

weight is the convolution of a flat distribution, and a normal distribution, evaluated at the on-sky distance measured between star i and the SN. Because a cluster of stars disperse as the cluster ages, this weighting function will have a different shape at different ages. Thus, $\mathrm{PhysDist}_i$ is a function of two variables – the distance of the star from the SN (a measured constant) and the age of the cluster (a fit parameter).

To translate the measured value of IGoF for an isochrone into a relative probability that the observed stars match the isochrone, careful forward modeling is required. A set of artificial stars equal in number to the detected stars are generated from each isochrone, drawn from normal distributions in flux space using the characteristic flux error from the detected stars in the host galaxy image. These stars are given radial distances on the sky generated from the expected radial distribution of stars in a cluster of a given age. This is the same radial distribution used to weight the observed stars in the IGoF, and is solely dependent on the cluster age parameter (the isochrone age). An IGoF value is then measured for the set of artificial stars. This process is repeated 5000 times for each isochrone, until the histogram of IGoF values converges to a probability distribution. This probability density function (PDF) gives a probability of measuring a value of IGoF, given the chosen age, metallicity, and host galaxy reddening associated with the isochrone. Using this isochrone PDF, the values of IGoF measured from the data are translated into values of relative probability for each isochrone. These relative probabilities are then normalized to determine a relative probability distribution in age, metallicity and host galaxy extinction for each SN. We then marginalize over metallicity and host galaxy extinction in order to extract the one dimensional age distributions for

each object.

Further details of our method, including the likelihood function used in the isochrone fitting scheme are shown in Appendix 4.7.1.

4.3.3 False Star Tests and Photometric Completeness

To determine the completeness of our photometry, we perform false star recovery tests using the false star tool in `DOLPHOT`. For host galaxy image, we insert 50,000 stars with magnitudes covering the whole range of measured magnitudes, and with x-y positions covering the entirety of the region around the SN. Using the results of the false star runs in `DOLPHOT` and binning with 0.1 mag resolution, we calculate a recovery fraction as a function of magnitude for each host galaxy image. We then apply this recovery fraction to the artificial stars generated while calculating IGoF in the process mentioned above.

In several of the imaged SN host galaxies, no stars are detected within 200 pc of the SN position. In order to get an upper bound on the age of the progenitor star for these SNe, we use the recovery fraction calculated using false star testing. From this recovery fraction function, we determine a limiting magnitude of detection in the image, by requiring that 90% of inserted stars be recovered for each magnitude bin above our limiting magnitude. We then simulate the effects of a $50M_{\odot}$ open cluster (Lada 2010 find $50M_{\odot}$ to be the most common open cluster mass) at the position of the SN under consideration, drawing stars from a Kroupa Initial Mass Function (IMF) (Kroupa 2001) until we reach the total cluster mass. If any of these drawn stars have brightnesses above our limiting magnitude given the isochrone we are considering, we

rule out the associated age, metallicity, and reddening combination for this SN. By repeatedly performing this analysis for each isochrone, we establish a $3-\sigma$ lower bound on the age of each SN progenitor system for which we detect no nearby stars (SNe 2008A, 2008ge, and 2011ay).

4.4 Analysis of Individual Objects

The objects in our sample and the associated data used for this study are listed in Table 4.1.

4.4.1 SN 2008A

SN 2008A was discovered in NGC 624 (Nakano et al. 2008), at an estimated Tully-Fisher distance of 51.5 ± 11.0 Mpc (Theureau et al. 2007). For this object, we assume no host galaxy extinction, as the SN is located on the fringes of it's host galaxy (Lyman et al. 2018). The metallicity for this object is difficult to measure (Lyman et al. 2018), so we use solar metallicity as our prior (Asplund et al. 2009). For additional analysis of SN 2008A, see e.g., Milne et al. (2010), Hicken et al. (2012), McCully et al. (2014b), and Foley et al. (2016).

In our photometric analysis, we find no stars within 200 parsecs of the SN position. As such, we use the false stars method of `DOLPHOT` to set a lower limit on the delay time for this object. This analysis measures a minimum delay time for SN 2008A of $\mathrm{Age}_{08A} \geq 6$ Myr.

4.4.2 SN 2008ge

SN 2008ge was discovered in NGC 1527 (Pignata et al. 2008), at an estimated Tully-Fisher distance of 17.37 ± 0.96 Mpc (Tully et al. 2013). We assume no host galaxy extinction for this object (Foley et al. 2010b). For this object, we also use a solar metallicity prior (Jorgensen 1997).

In our photometric analysis, we find no stars within 200 parsecs of the SN position. As with SN 2008A, we use the false stars method of `DOLPHOT` to set a lower limit on the delay time for this object. From this analysis, we find $\mathrm{Age}_{08ge} \geq 18$ Myr.

4.4.3 SN 2008ha

SN 2008ha was discovered in UGC 12682 (Puckett et al. 2008), which has an redshift-derived distance of 21.3 ± 1.5 Mpc (Foley et al. 2014). Lyman et al. (2018) report a metallicity of $[\mathrm{Fe/H}] = -0.78 \pm 0.09$ in the region directly around the SN. Additionally, Foley et al. (2014) report no indication of host extinction in the region around the supernova. For more information on SN 2008ha, see e.g., Valenti et al. (2009), Foley et al. (2009), Pumo et al. (2009), Fryer et al. (2009), Foley et al. (2010a), Stritzinger et al. (2014), and Foley et al. (2016). Our analysis uses 16 stars in the vicinity of SN 2008ha to perform the isochrone fitting.

Using the measurement from Lyman et al. (2018) as a prior, metallicity is allowed to float between $[\mathrm{Fe/H}] = -0.50$ and -1.00. Our fitting algorithm returns a metallicity posterior which is slightly skewed towards solar metallicity, as compared to the prior. Our fits show no preference for any host galaxy reddening for the stars

around the SN, consistent with the literature (Foley et al. 2014). Finally, the posterior distribution for distance from observer to host galaxy nicely matches the prior distribution. This is true for all of the SN fit in this sample, and is thus not mentioned again. Marginalizing over metallicity, we measure the delay time for SN 2008ha of 52^{+13}_{-9} Myr. The full probability distribution in delay time is shown in Figure 4.1.

4.4.4 SN 2010ae

SN 2010ae was discovered in ESO 162-17 (Pignata et al. 2010), which is determined using the Tully-Fisher relation to be 11.09 ± 1.02 Mpc away (Tully et al. 2013). Lyman et al. (2018) report a metallicity of [Fe/H] $= -0.43 \pm 0.06$ in the region directly around the SN. A high (though uncertain) upper limit on host extinction of $E(B-V)_{\rm host} = 0.50 \pm 0.42$ mag is reported in the region around the supernova (Stritzinger et al. 2014). Additional information on SN 2010ae can be found in e.g., Foley (2013) and Foley et al. (2016). We find 11 stars in the vicinity of SN 2010ae, which we use for our isochrone fitting.

We use Gaussian priors for both metallicity and host-galaxy extinction. The posterior distribution in extinction is skewed towards low extinction values, with a strong preference for $E(B-V)_{\rm host} \leq 0.36$ mag. The posterior distribution in metallicity on the other hand is completely consistent with the prior distribution. Marginalizing over both metallicity and host-galaxy extinction, we find a delay time of 117^{+19}_{-29} Myr for SN 2010ae. The full probability distribution for the age of the progenitor is shown in Figure 4.2. The measured probability distribution in age has two peaks, one at 9 Myrs, the other at 110 Myrs. This is likely indicative of two separate stellar populations at

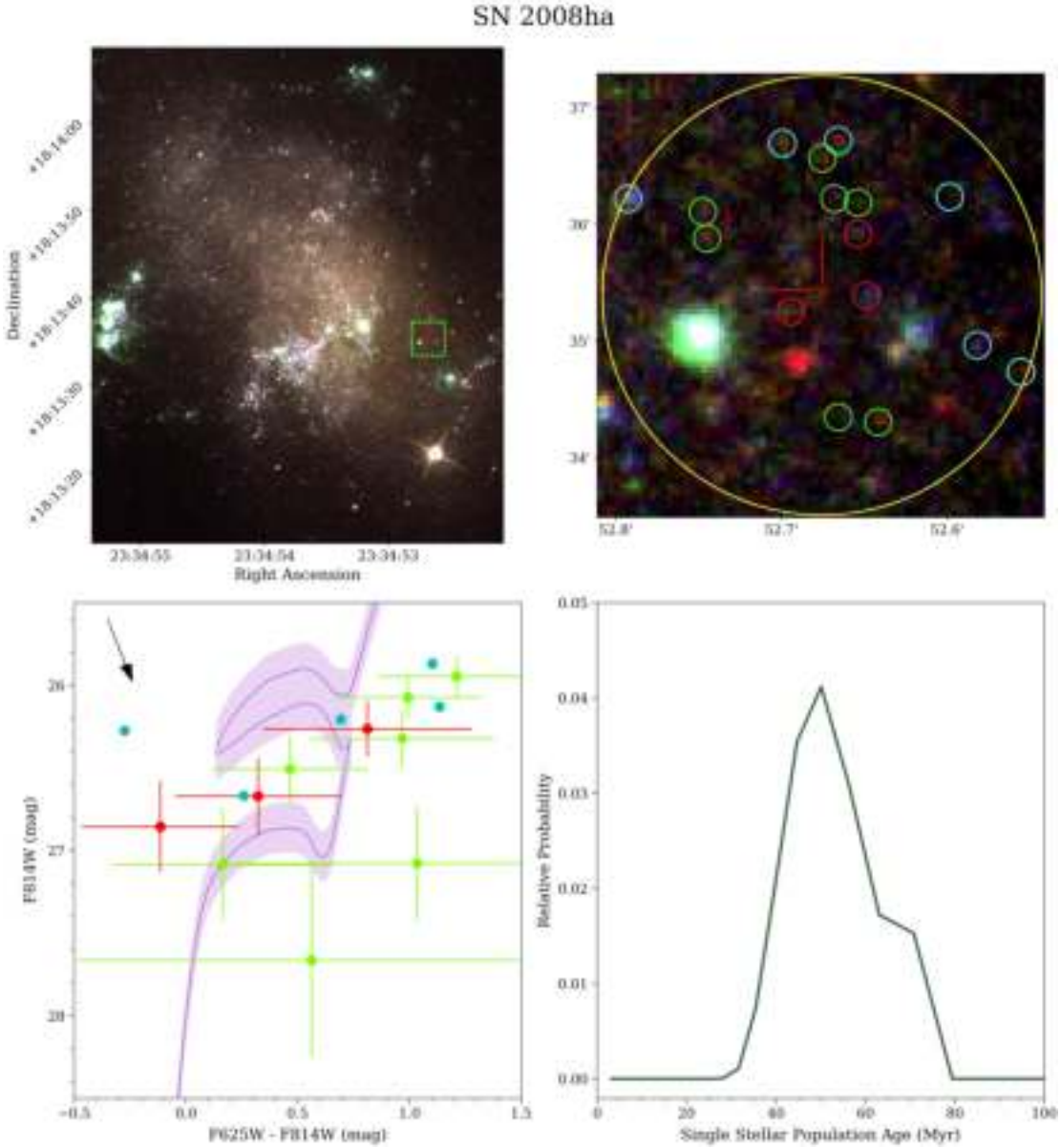

Figure 4.1: From left to right and top to bottom: a) UGC 12682 with a box with side lengths of 400 pc centered on SN 2008ha. b) The 200 pc radius around SN 2008ha, with the stars used in this study circled. Stars in red are closest to the SN position, followed by those in green, then those in blue. c) A color-magnitude diagram with each of the stars plotted, along with the isochrone for 50 Myr. Error bars are not shown for the blue stars, to avoid overcrowding the diagram. The reddening vector in the upper left shows the direction in which the isochrone would move if there were non-negligible host galaxy extinction. d) The probability distribution for the age of the SN 2008ha progenitor.

the explosion site of SN 2010ae, either of which may have been associated with the SN. Providing further evidence for two separate stellar population in the area is the preferred host galaxy extinction values for the isochrone fit. The younger peak favors high values for extinction, while the older peak favors lower values, indicating that the younger population is in the background as compared to the older, as its light passed through more dust. Additionally, the metallicity prior for this population likely slightly skews our analysis towards lower ages, as the prior comes from strong emission line ratios. This could serve to overstate the probability of the younger peak as compared to the older peak in our final PDF.

The probability distribution in delay time that we measure for this object is particularly illuminating, as it demonstrates that our method is able to recover the short delay times that we would expect from a WR progenitor scenario. The young stars around SN 2010ae are likely a stellar population that is unrelated to the SN progenitor, but our detection of this population indicates that our analysis pipeline is working correctly.

4.4.5 SN 2010el

SN 2010el was discovered in NGC 1566 (Monard 2010), at a Tully-Fisher distance of 5.63 ± 1.12 Mpc (Tully et al. 2013). Lyman et al. (2018) report a metallicity of [Fe/H] $= 0.16 \pm 0.07$ at the site of the SN. No precise measurement is available of the host galaxy extinction in the region around the SN, though a measurement of the extinction of the galaxy at large has been measured to be $E(B-V)_{\rm host} = 0.205$ mag (Gouliermis et al. 2017). We use 46 stars in the vicinity of SN 2010el to perform our

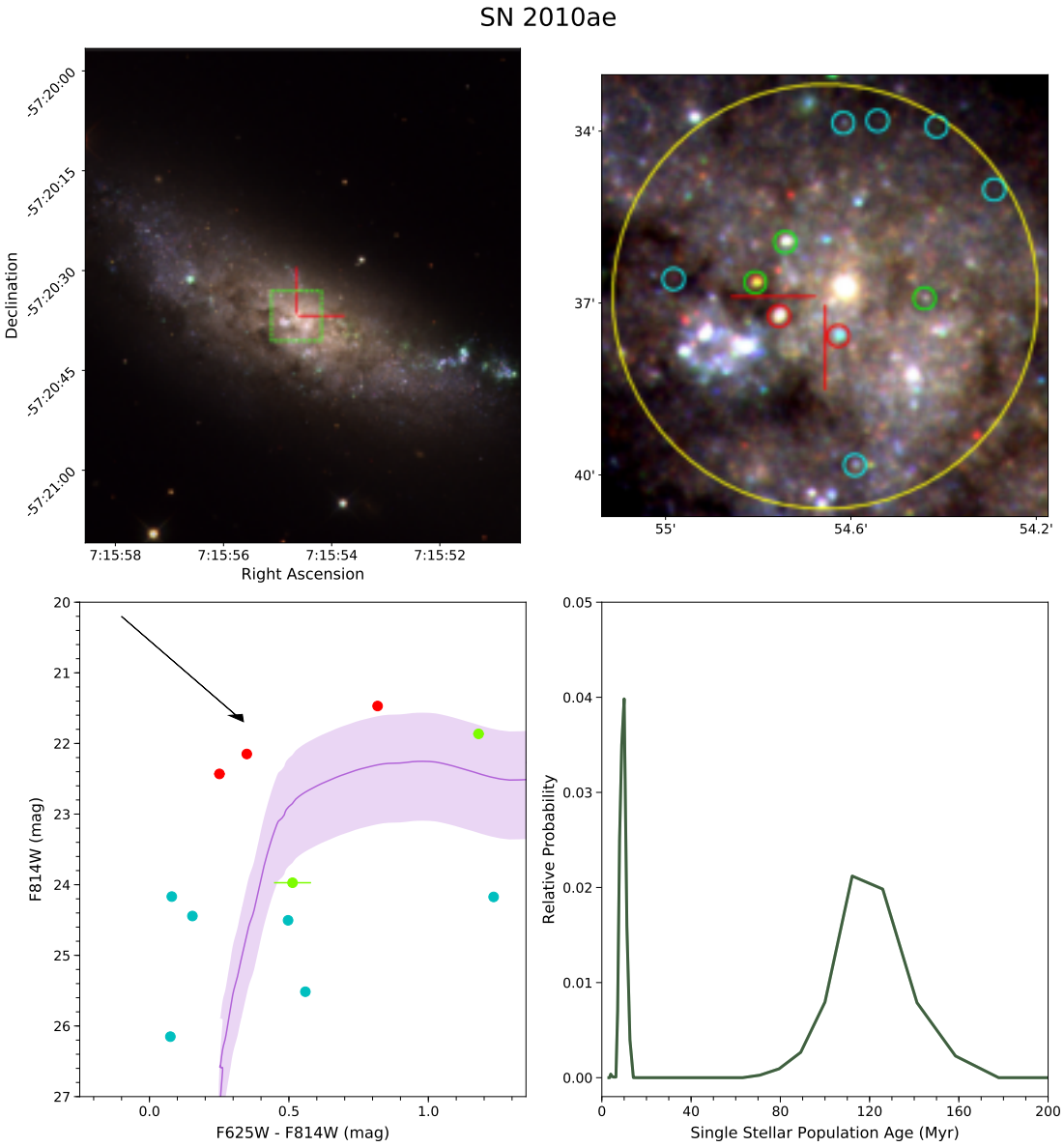

Figure 4.2: From left to right and top to bottom: a) ESO 162-17 with a box with side lengths of 400 pc centered on SN 2010ae. b) The 200 pc radius around SN 2010ae, with the stars used in this study circled. c) A color-magnitude diagram with each of the stars plotted, along with the median age isochrone of 116 Myr. Stars in red are closest to the SN position, followed by those in green, then those in blue. d) The probability distribution in age for the SN 2010ae progenitor.

isochrone fitting.

Though we analyse both ACS/WFC data and WFC3/UVIS data for this object, DOLPHOT is better able to identify stars in the ACS/WFC data. As such, our ACS/WFC data is far more discernining than the WFC3/UVIS data which we analyze. For this reason, the PDF in age for this object is determined from the ACS/WFC data. All of the analysis for SN 2010el that follows is based on this ACS/WFC data.

We use the metallicity estimate for the SN as a prior, while assuming a flat prior of $0 \leq E(B-V)_{\rm host} \leq 0.205$ mag for the extinction. Our posterior in metallicity is consistent with the prior, showing a slight preference towards higher metallicity. Our posterior in host galaxy extinction shows a strong preference for non-zero extinction, with the preferred value of $E(B-V)_{\rm host} = 0.205$ mag. When we marginalize over metallicity and host-galaxy extinction, we find a delay time of 53^{+5}_{-6} Myr for SN 2010el. The age probability distribution is shown in Figure 4.3.

4.4.6 SN 2011ay

SN 2011ay was discovered in NGC 2315 (Blanchard et al. 2011), to which we measure a distance of 87.4 ± 6.4 Mpc, derived from the galaxy's redshift (Miller & Owen 2001). Using the measured metallicity gradient for NGC 2315, we infer a metallicity of $[{\rm O/H}] = -0.19 \pm 0.20$ (Lyman et al. 2018). The SN has a relatively large offset from its host galaxy, with the SN occurring in a rather empty environment. As such, we assume no host extinction as our prior. For more detailed analysis of SN 2011ay, see White et al. (2015), Szalai et al. (2015), Foley et al. (2016), and Barna et al. (2017).

As with SN 2008A and SN 2008ge, in our photometry of NGC 2315, we find

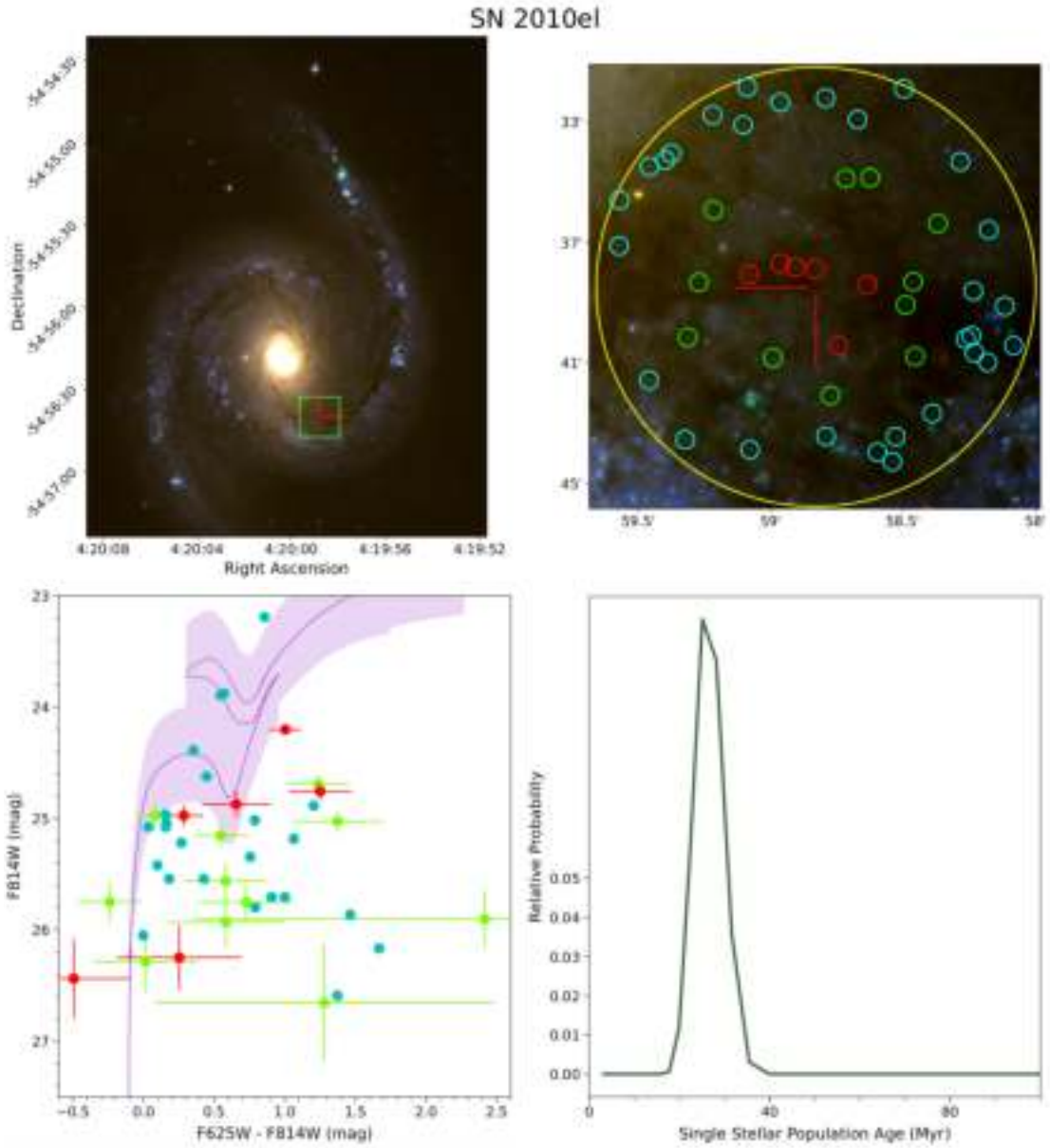

Figure 4.3: From left to right and top to bottom: a) NGC 1566 with a box with side lengths of 400 pc centered on SN 2010el. b) The 200 pc radius around SN 2010el, with the stars used in this study circled. c) A color-magnitude diagram with each of the stars plotted, along with the best fitting isochrone for 53 Myr. Stars in red are closest to the SN position, followed by those in green, then those in blue. d) The probability distribution in age for the SN 2010el progenitor.

no stars within 200 parsecs of the SN location. We perform the same false star tests as with these two objects, in the hope of getting a lower limit on the delay time. However, because of the great distance to NGC 2315, our method cannot rule out any of the isochrones considered in this study.

4.4.7 SN 2012Z

SN 2012Z was discovered in NGC 1309 (Cenko et al. 2012), which is determined to be 31.92 ± 0.88 Mpc away (Riess et al. 2016), using the Cepheid distance method. Lyman et al. (2018) report a metallicity of [Fe/H] $= -0.43 \pm 0.08$ at the site of the SN, in agreement with metallicity gradient that they measure. Host galaxy reddening is estimated to be $E(B-V)_{\rm host} = 0.07 \pm 0.03$ mag using Na I and K I doublets (Stritzinger et al. 2015). More information on SN 2012Z can be found in e.g., McCully et al. (2014a), Yamanaka et al. (2015), and Foley et al. (2016). We use 10 stars in the vicinity of SN 2012Z to perform our isochrone fitting.

Using these measurements as Gaussian priors, we fit for both metallicity and host galaxy extinction. In each case, the calculated posterior is consistent with the prior, showing a slight preference for metallicity and host reddening on the upper end of the ranges given in the literature. Marginalizing over metallicity and extinction, we measure a delay time of 61^{+13}_{-11} Myr for SN 2012Z. The full probability distribution in age is shown in Figure 4.4.

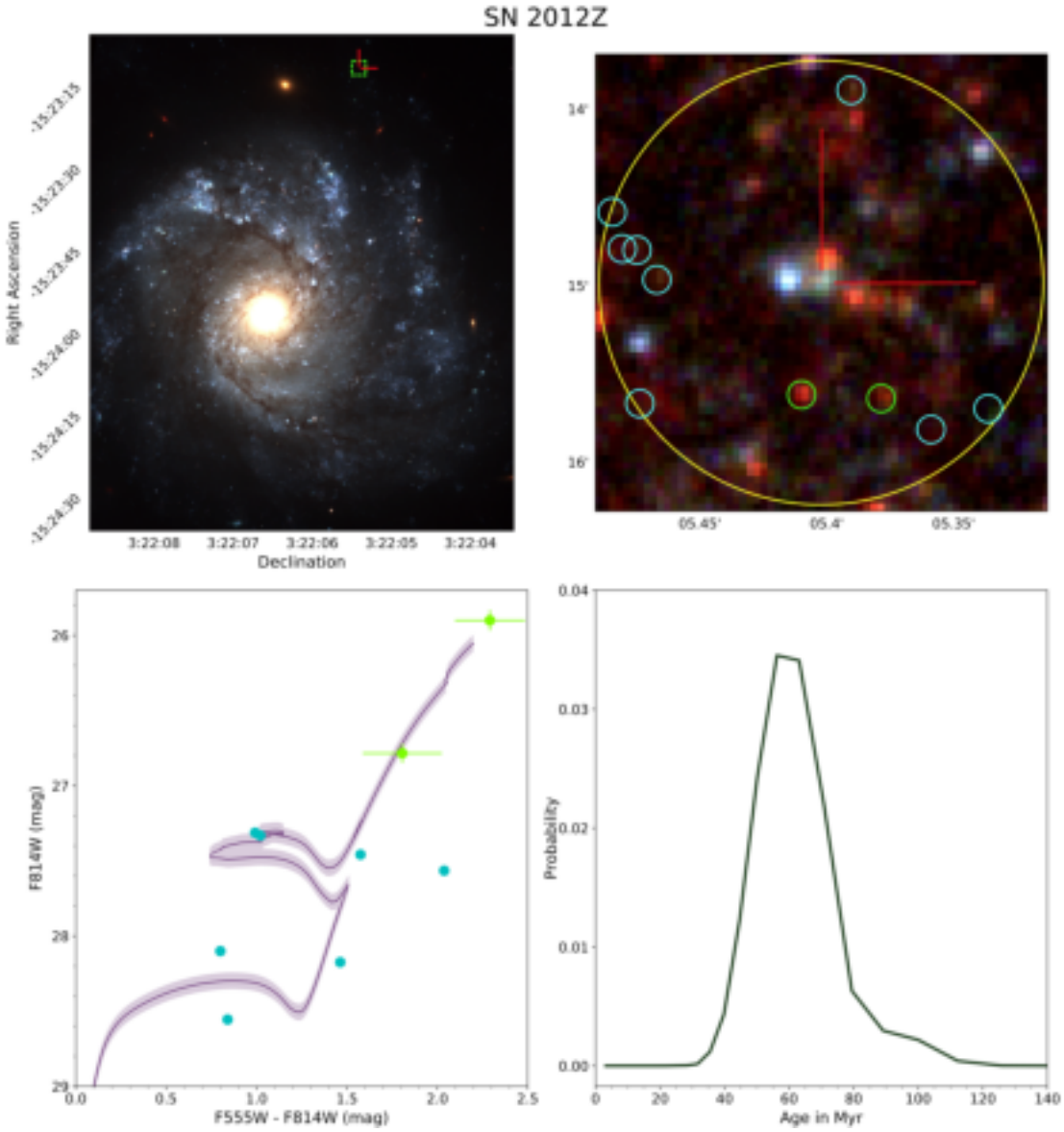

Figure 4.4: From left to right and top to bottom: a) NGC 1309 with a box with side lengths of 400 pc centered on SN 2012Z. b) The 400 pc box around SN 2012Z, with the stars used in this study circled. c) A color-magnitude diagram with each of the stars plotted, along with the isochrone for 56 Myr. Stars in red are closest to the SN position, followed by those in green, then those in blue. d) The probability distribution in age for the SN 2012Z progenitor.

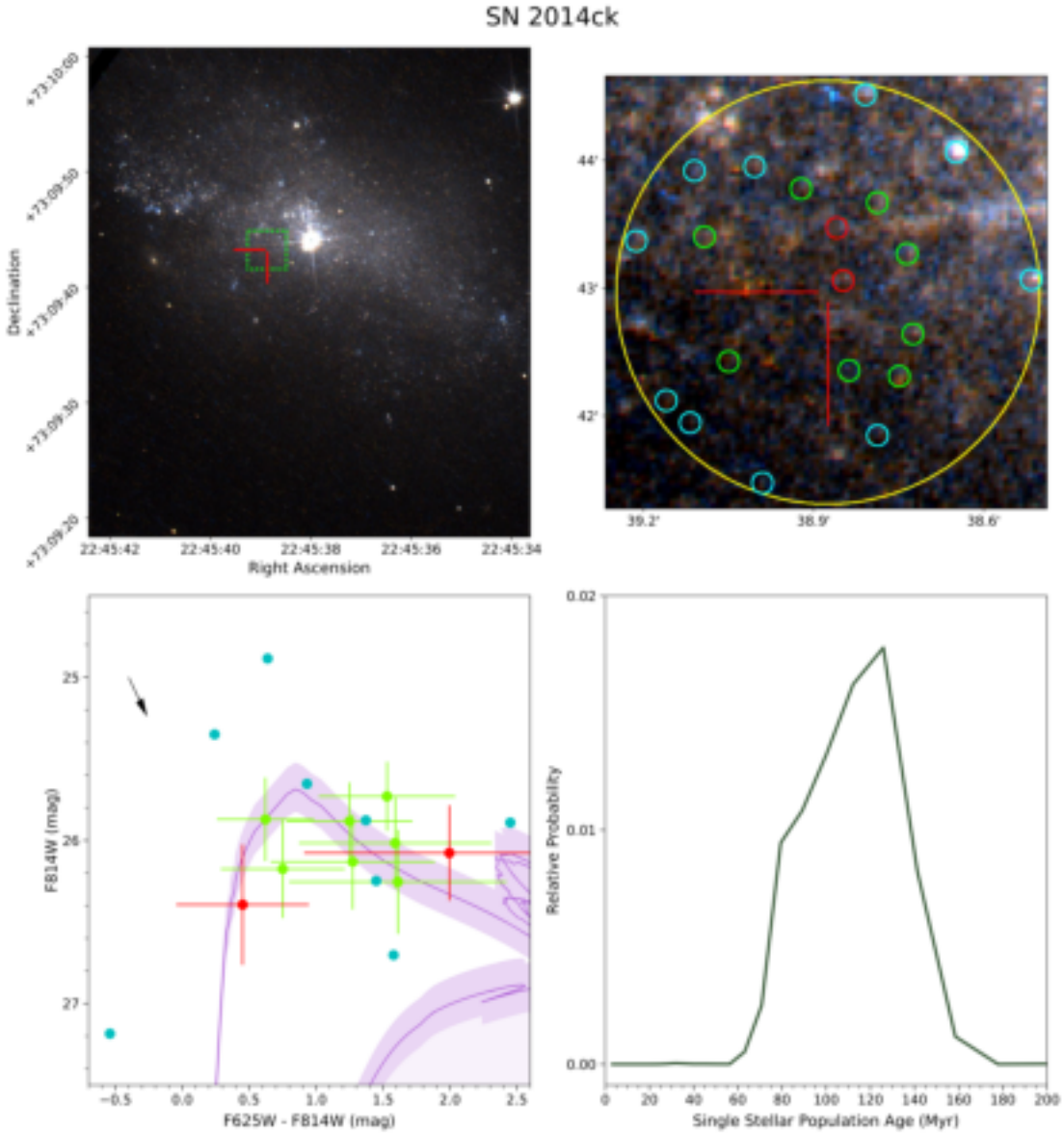

Figure 4.5: From left to right and top to bottom: a) UGC 12182 with a box with side lengths of 400 pc centered on SN 2014ck. b) The 200 pc radius around SN 2014ck, with the stars used in this study circled. c) A color-magnitude diagram with each of the stars plotted, along with the isochrone for 113 Myr, corresponding to the median of the distribution. Stars in red are closest to the SN position, followed by those in green, then those in blue. d) The probability distribution in age for the SN 2014ck progenitor.

4.4.8 SN 2014ck

SN 2014ck was discovered in UGC 12182 (Masi et al. 2014), which is determined to be 24.32 ± 1.69 Mpc away (Tomasella et al. 2016), based on its redshift. Taddia et al. (2015) report a metallicity of [Fe/H] $= -0.51 \pm 0.26$ at the site of SN 2006fp, which is also located in UGC 12182, at roughly the same projected distance from the galaxy nucleus. The host galaxy extinction is estimated to be $E(B-V)_{\rm host} \leq 0.05$ mag, determined using the Na I absorption line (Tomasella et al. 2016). We use 20 stars in the vicinity of SN 2014ck to perform our isochrone fitting.

These measurements are used as priors, with the metallicity and host galaxy extinction then fit and the posterior in metallicity and extinction measured. Our posterior in metallicity is peaked around the same value as the prior, though with noticeably thinner tails, indicating that our data show a strong preference for [Fe/H] $= -0.51$. Our data also indicate no preference for higher extinction, showing consistency with $E(B-V)_{\rm host} = 0$ mag. Marginalizing over both metallicity and extinction, we measure a delay time of 113^{+21}_{-25} Myr for SN 2014ck. The full age probability distribution is shown in Figure 4.5.

4.4.9 SN 2014dt

SN 2014dt was discovered in Messier 61 (Ochner et al. 2014) at a distance of 19.3 ± 0.6 Mpc (Rodríguez et al. 2014) from our Milky Way galaxy. Lyman et al. (2018) report a metallicity of [Fe/H] $= 0.16 \pm 0.07$ at the explosion site of SN 2014dt, in rough agreement with the metallicity of [Fe/H] $= -0.01$ reported in Foley et al. (2015). Foley

et al. (2015) also report no indications of host-galaxy reddening at the site of the SN. We adopt these as priors for our fit.

Our method finds no likely stars within 200 pc of the SN. Performing the false star analysis described in Section 3.3, we are unable to confidently rule out any ages that we test.

4.5 Discussion

4.5.1 Summary of Data Used in Analysis

Our final analysis relies on seven SNe, including five with full probability distributions in delay-time. These five SNe are SN 2008ha, SN 2010ae, SN 2010el, SN 2012Z, and SN 2014ck. To find the populations around these SNe, we use 16, 11, 46, 10, and 20 stars respectively. The two SNe for which we have useful lower limits on delay-time are SN 2008A and SN 2008ge.

4.5.2 Verification of Fitting Method

As mentioned earlier, the probable progenitor star for SN 2012Z has previously been detected (McCully et al. 2014a), while a progenitor search for SN 2008ha has yielded strong limits on the delay time for this object (Foley et al. 2014). In Foley et al. (2014), the authors also fit Padova isochrones to the stars directly surrounding the probable remnant of SN 2008ha, to measure an approximate delay-time for the SN. They find a 1-σ confidence interval on the age of the system of 55^{+13}_{-10} Myr. Using our isochrone fitting method, we find a 1-σ confidence interval of 52^{+13}_{-9} Myr, in excellent

agreement with the literature. In McCully et al. (2014a), the authors similarly fit isochrones by eye to the stars surrounding the possible progenitor of SN 2012Z, deriving a best fitting age range of 10 - 42 Myrs. With our analysis, we find a 1-σ confidence internal of 61.0^{+13}_{-11} Myr. This disagreement is only at the $\sim 1\sigma$ level and likely comes from the fact that McCully et al. (2014a) used several sources in close proximity to the SN in their fit, which our analysis rejects as being too extended to confidently classify as stars. Our fit instead relies on sources which are further from the SN, but which are more likely to truly be stars. This new preference for higher ages now strongly suggests that SN 2012Z is not consistent with a WR progenitor system.

4.5.3 Comparisons Between Objects

We check for correlations between delay time and peak luminosity, and between delay time and metallicity (as (Liu et al. 2015) suggest). Our peak luminosities are taken from the Open Supernova Catalog (Guillochon et al. 2017), while our metallicities are the priors used for our fitting (citations listed above). For this check, we perform Pearson r-tests to measure the strength of a correlation (or anti-correlation) between our measured delay time and either metallicity or peak luminosity. We find r values very close to zero in each case, indicating no statistically significant correlations.

Though SN 2008ge is unique in its host galaxy characteristics, it does not appear to stand out in this study. Instead, we find that the lower limit which we measure from SN 2008ge is completely consistent with the measured DTDs of all but one of the SN in our study. The DTD for SN 2010ae is double peaked, showing two stellar populations. The older of these two populations is consistent with the lower

bound from SN 2008ge, though the younger population is not. Because of this broad agreement between SN 2008ge and the sample at large, for the purposes of this study SN 2008ge appears to belong to the class of "standard" SNe Iax. SN 2014ck has also been called an outlier among SNe Iax due to its observed properties (Tomasella et al. 2016). However our analysis does not find that its delay time in significantly different from the delay times of the rest of our sample.

4.5.4 SN 2014dt Progenitor Mass Limit

The false star tests that we perform for SN 2014dt give us a $3-\sigma$ magnitude limit of 24 mag in the F438W filter. Though this is not sufficient to rule out any isochrones that we test, it is sufficient to rule out single stars more massive than $19.5 M_{\odot}$ at the distance of the host galaxy of SN 2014dt. Using MESA single stellar evolution models of the appropriate metallicity, this roughly corresponds to a lower limit on the delay time for this particular object of 10 Myrs. Because this limit is not derived using the same methods as the rest of the study, we do not include the limit in the rest of the analysis.

4.5.5 Empirical Measurements

If we assume that all SNe Iax that we consider in this study share a progenitor channel, we can make strong statistical statements about the delay-time distribution of SNe Iax at large. The probability density function (PDF) for each SN, and the summed PDF (unnormalized for clarity in the figure) are shown in Figure 4.6. Taking only the SNe for which a full DTD can be measured (ignoring lower limits), we find a

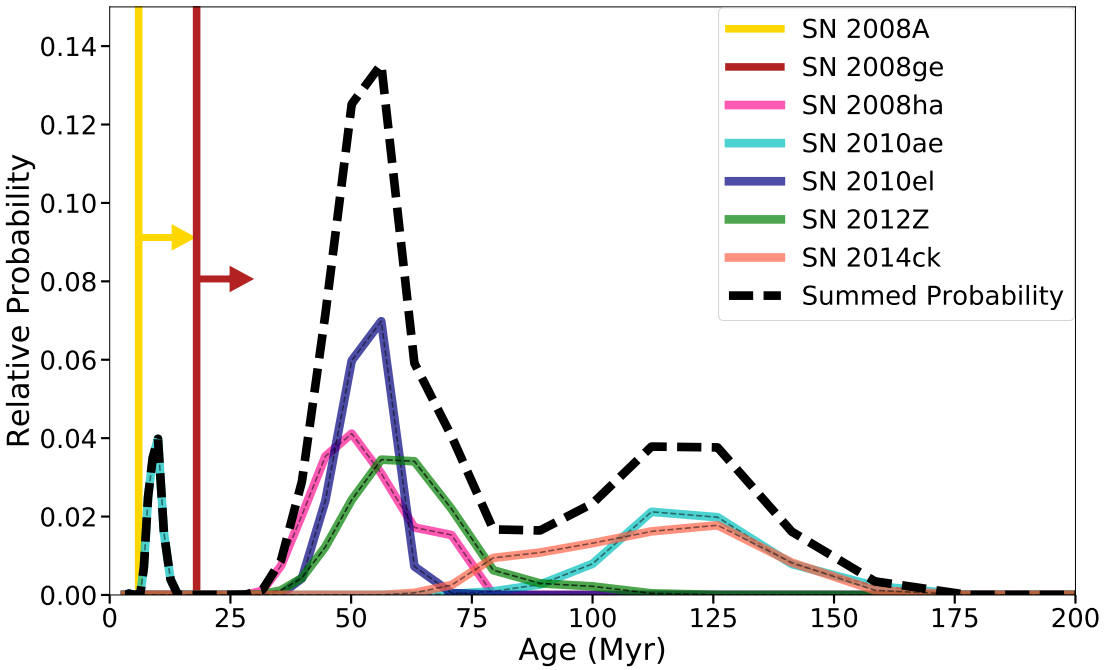

Figure 4.6: The probability density functions (PDFs) for each SN considered in this study. The "Summed Probability" is the sum of the PDF for each object in the study. As such, it is normalized to 5 (the number of objects in the sample with defined PDFs).

median delay time and $1-\sigma$ confidence interval of 63^{+58}_{-15} Myrs. The data show a strong preference for a delay time peaked near 55 Myrs, with the PDFs for three SNe peaking within 6 Myrs of 55 Myrs. SN 2014ck and SN 2010ae on the other hand, represent the long tail of the distribution to higher ages, with the medians of their DTDs at 113 Myr and 117 Myr respectively.

If we then draw groups of 5 SNe (the number of SNe Iax in the summed PDF) from our summed PDF and fit power-law decay models to the result in an MCMC fashion, we find the posterior distribution in Figure 4.7. This is done using `emcee` (Foreman-Mackey et al. 2013) with a flat prior on the cutoff age (0 to 100 Myr) and an inverse-gamma prior with a peak at -1 for the decay exponent. The resulting form of this power-law decay is then described by Equation 2.

$$p(t) = \begin{cases} 0 & t < a \text{ Myrs}, \\ t^{-b} & t >= a \text{ Myrs}. \end{cases} \tag{4.3}$$

The distributions of the cutoff age (labeled a) and the decay power (labeled b) are shown in Figure 4.7. The 1-sigma confidence intervals for each parameter are $40.83^{+7.85}_{-13.38}$ Myrs and $2.52^{+1.18}_{-0.81}$ respectively.

As seen in Figure 4.7, the distribution in cut-off age (a) is double peaked. This double peaked distribution is due to the double peaked measured DTD for SN 2010ae. The less probable, younger peak in a is due to the fit occasionally drawing an age from the younger peak of the SN 2010ae DTD, and trying to fit this alongside the

older ages from the other SNe. This could just be the result of a 2nd stellar population forming near the explosion site of SN 2010ae by chance, or it could be indicative of a heterogeneity in SNe formation channels. Repeating this study with a larger sample of SNe Iax – for instance, once many more are discovered by the *Large Synoptic Survey Telescope* (LSST) – would allow for one to answer this question one way or another.

4.5.6 Model Comparisons

In Valenti et al. (2009), Moriya et al. (2010), and Pumo et al. (2009), the authors suggest a core-collapse origin for at least some SNe Iax. These models predict a maximum delay time for SNe Iax of 6 to 10 Myrs (Fryer 1999; Heger et al. 2003). If we ignore the events with no nearby stars detected, we find just a 2% probability of at least one SN in our sample having a delay time of 10 Myr or less, strongly suggesting a long-lived progenitor channel for SNe Iax. Using only the analysis of SN 2008ge, we find a $3-\sigma$ minimum age of 18 Myrs, giving us strong evidence that SNe Iax are not produced by short-lived progenitors.

The WD He-star binary model for the progenitor systems of SNe Iax instead predicts a delay-time of roughly 30 Myrs and up, with an expected peak in probability at the lower bound delay-time, and a long tail up to much higher ages (Wang et al. 2014; Liu et al. 2015). The power law decay which we fit to the summed PDF above is a good parameterization of this expected DTD. The best-fit lower limit on delay-time for our data is $40.82^{+7.85}_{-13.38}$ Myrs, in excellent agreement with the model predictions.

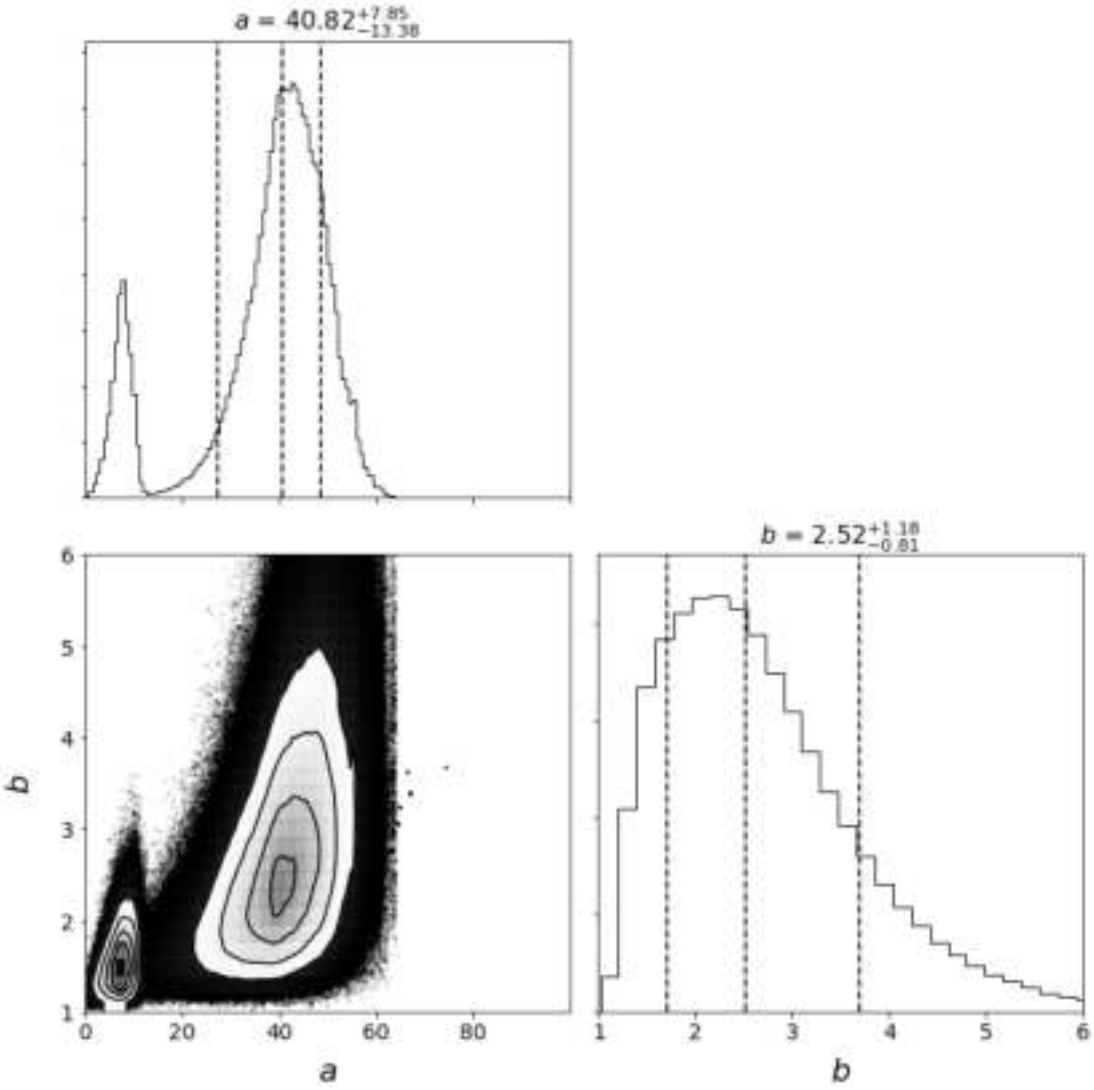

Figure 4.7: The distributions in each parameter used in the power law fit. Parameter a is the cutoff age, while parameter b is the decay power.

4.6 Conclusions

We have developed a new method to fit simulated photometry of stellar populations generated from `MIST` isochrones to broadband photometric measurements, weighted by distance from a cluster center. We then use this method to fit the stellar neighborhoods of nine SNe Iax. We employ Bayesian methods to generate probability distributions for the delay times for these nine objects. The probability distributions are shown in Figure 4.6. We find a 68% confidence interval for the delay time of our sample of 63^{+58}_{-15} Myrs. When fitting a power law to the overall probability distribution, we find a 68% confidence interval on the lower bound on the delay time of $40.83^{+7.85}_{-13.38}$ Myrs.

Taken together, this sample of SNe Iax provides the most precise measurement of the DTD for SNe Iax to date. The data strongly disfavor a fallback core-collapse origin for SNe Iax, instead showing consistency with a WD-He star binary progenitor model.

Acknowledgements

Based on observations made with the NASA/ESA Hubble Space Telescope, obtained from the Data Archive at the Space Telescope Science Institute, which is operated by the Association of Universities for Research in Astronomy, Inc., under NASA contract NAS 5–26555. These observations are associated with programs GO-12999 and GO-14244.

This chapter includes data gathered with the 6.5 meter Magellan Telescopes located at Las Campanas Observatory, Chile.

The authors would like to thank A. Skemer for his helpful advice in the design

of the Isochrone Goodness of Fit statistic used in this chapter. We also thank J. Maund and C. Kilpatrick for their helpful advice on using DOLPHOT. We thank R. Hounsell, and D. Kasen and L. Bildsten for their contributions to one of the two HST proposals that led to this chapter. We thank R. Chornock for assistance with the Magellan observations, and J.D. Lyman for his willingness to share data with us. We additionally thank A. Wasserman for his help with the final statistical analyses of the DTD, and J. Schwab for numerous helpful discussions. We also thank both of the referees who reviewed this chapter for their helpful and insightful comments. Finally, we thank R. Murray-Clay, without whose advice and patience this work would not have been possible.

The UCSC team is supported in part by HST programs GO-12999 and GO-14244, NSF grant AST-1518052, the Gordon & Betty Moore Foundation, the Heising-Simons Foundation, and by a fellowships from the David and Lucile Packard Foundation to R.J.F. This SN Iax research at Rutgers University is supported by NSF award 161545 and HST programs GO-11133, GO-11590, GO-12913, and GO-13757. M. Stritzinger is supported by a research grant (13261) from the VILLUM FONDEN.

4.7 Appendices

4.7.1 Additional Information on Isochrone Fitting

The likelihood function which we use in our isochrone fitting scheme is shown below.

$$\text{Like}(\text{Data}, D, R|\text{Iso.}) = \prod_i p(\text{star}_i, D, R|\text{Iso.}), \tag{4.4}$$

$$= \prod_i L_i, \tag{4.5}$$

$$L_i = \max(L_{ij}), \tag{4.6}$$

$$L_{ij} = \prod_k \frac{1}{\sqrt{2\pi\sigma_{ik}^2}} e^{-\frac{1}{2\sigma_{ik}^2}(m_{ik}-m_{\text{Iso},jk})^2}, \tag{4.7}$$

where D is distance from the observer to the host galaxy, R is host galaxy reddening, i specifies a given star, j specifies a given stellar mass in the isochrone, k specifies a given filter, m_{ik} is the magnitude of a given star in a filter, and σ_{ik} is the corresponding uncertainty. Additionally, $m_{\text{Iso},jk}$ is the magnitude drawn from an isochrone in a given filter for a given mass and adjusted for distance, Milky Way reddening, and host galaxy reddening. Our priors for host reddening (R) and distance (D) are normal distributions defined by measured values and uncertainties from the literature and described for each SN in Section 4.4.

The posterior distribution for an isochrone given a stellar population is then:

$$p(\text{Iso.}|\text{Data}) = \iint p(\text{Iso.}|\text{Data}, D, R) \cdot p(D) \cdot p(R) dD dR, \tag{4.8}$$

$$p(\text{Iso.}|\text{Data}, D, R) \propto \text{Like}(\text{Data}|\text{Iso.}, D, R) \cdot p(\text{Iso.}), \tag{4.9}$$

$$p(\text{Iso.}) = p(\text{Age}) \cdot p(\text{Metallicity}).$$

Here p(Age) and p(Metallicity) are the prior distributions in age and metallicity. Our prior in age is a log-flat distribution between $10^{6.5}$ and $10^{8.5}$ years. Our metallicity priors are normal distributions based on previous measurements in the literature, described in detail for each SN in section 4.4. sochrones are calculated for a grid of parameter values spanning the prior ranges and are fit to each stellar population. The posterior distribution for an isochrone is the relative probability that the stellar population being considered has a specific age, metallicity, distance from the observer (D), and host galaxy reddening (R), given the stellar data.

Our measured DTD for each SN is this posterior distribution, marginalized over metallicity.

$$p(\text{Age}|\text{Data}) = \int p(\text{Isochrone}|\text{Data}) p(Z) dZ, \tag{4.10}$$

where Z is metallicity.

4.7.2 Example of Isochrone Fitting

We will now walk through the process of fitting a set of isochrones to a data set of stars around a supernova. For this example, we will use SN 2008ha. As mentioned in

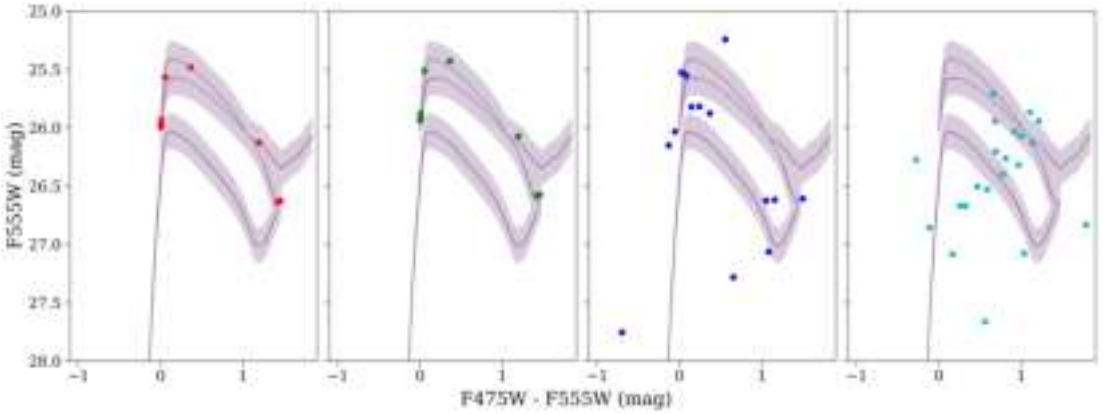

Figure 4.8: From left to right: a) The artificial stars drawn from the $10^{7.45}$ year isochrone with no errors. b) The artificial stars, with a distance error applied. c) The artificial stars, with both the distance error and the magnitude errors applied. d) The real stars for SN 2008ha, indicating general position in Color/Magnitude space.

Section 2, we run DOLPHOT on a set of HST images of the host-galaxy of SN 2008ha. We apply the recommended list of cuts on the data output in order to get a list of point sources in the image. This list is restricted to include only those stars which are within 200 pc projected on-sky distance from the SN, assuming a distance to the host-galaxy of 21.3 ± 1.5 Mpc. Clusters are removed using the method detailed in Section 2.3 in order to get our final list of stars which we will use for isochrone fitting.

The library of isochrones used in this study are logarithmically spaced in age, using 0.05 dex increments from $10^{6.5}$ to $10^{8.5}$ years. These isochrones are drawn using the median, $1-\sigma$, $2-\sigma$ metallicities of our prior, and adjusted for the internal reddening of the host-galaxy. We then construct a distribution to measure probability of a star forming with the SN progenitor, as explained at the beginning of Section 3. Now for each star in our data, we apply the weighting distribution evaluated at the distance of the star. We then find the minimum of the square root of the distance from the star to each isochrone, summed across all of the filters in the data. This process is completed for

each star in the data, summing the values measured for each star in quadrature. These values (different for each age, metallicity, and extinction) are our measured Isochrone Goodness of Fit (IGoF) values.

To convert the measured IGoF values to probability distributions in age, metallicity and host-galaxy reddening, we perform careful forward modelling. Stars are drawn from a Kroupa IMF, using the isochrone under consideration to convert the mass to a magnitude in each filter in our data, keeping each star if its associated magnitudes are above our observational limit. Once there are the same number of synthetic stars as real stars in the data, we apply a distance error to all of the synthetic stars together by drawing from a normal distribution with parameters determined by our distance prior. These stars are shown in the second panel of Figure 4.8. Magnitude errors are applied by drawing from a normal distribution for each star and filter, using the measured magnitude uncertainties as a function of magnitude which are derived from the data. These stars appear in the third panel of Figure 4.8. We now measure a value of IGoF, and repeat this process 5000 times for each isochrone, in order to get a probability distribution in IGoF for each isochrone. This PDF is used to relate our measured value of IGoF for the isochrone to a relative probability associated with the age, metallicity, and reddening of the isochrone.

The fourth panel of Figure 4.8 shows the real stars detected in the vicinity of SN 2008ha, to compare to the artificial stars which we draw from the isochrone. Note that the real data has higher dispersion than the artificial data because the real data likely features stars which were not born in the same star forming event as the SN

progenitor. These stars would have been drawn from isochrones of a different age, and hence would look like a bad fit for the isochrone we plot, whereas every artificial star is drawn from the same isochrone that is plotted.

In order to further verify our method, we generate false stars from our isochrone, applying characteristic errors to the stars and our observational sensitivities, and employ our method to recover the age and metallicity of the isochrone. The results of this effort are shown in Figure 4.9, Figure 4.10, and Figure 4.11. These figures have injected metallicities that correspond to the median from our prior ([Fe/H] $= -0.78$), while the injected ages are $10^{7.45}$, 10^{7}, and $10^{7.8}$ years. These tests are successful, as we recover the correct age as the approximate peak in each distribution. Note that each of these tests is performed with 15 stars, in order to match the data for SN 2008ha. For SNe around which we detect more stars (as in SN 2010el, for example), our method recovers the correct age with even higher precision.

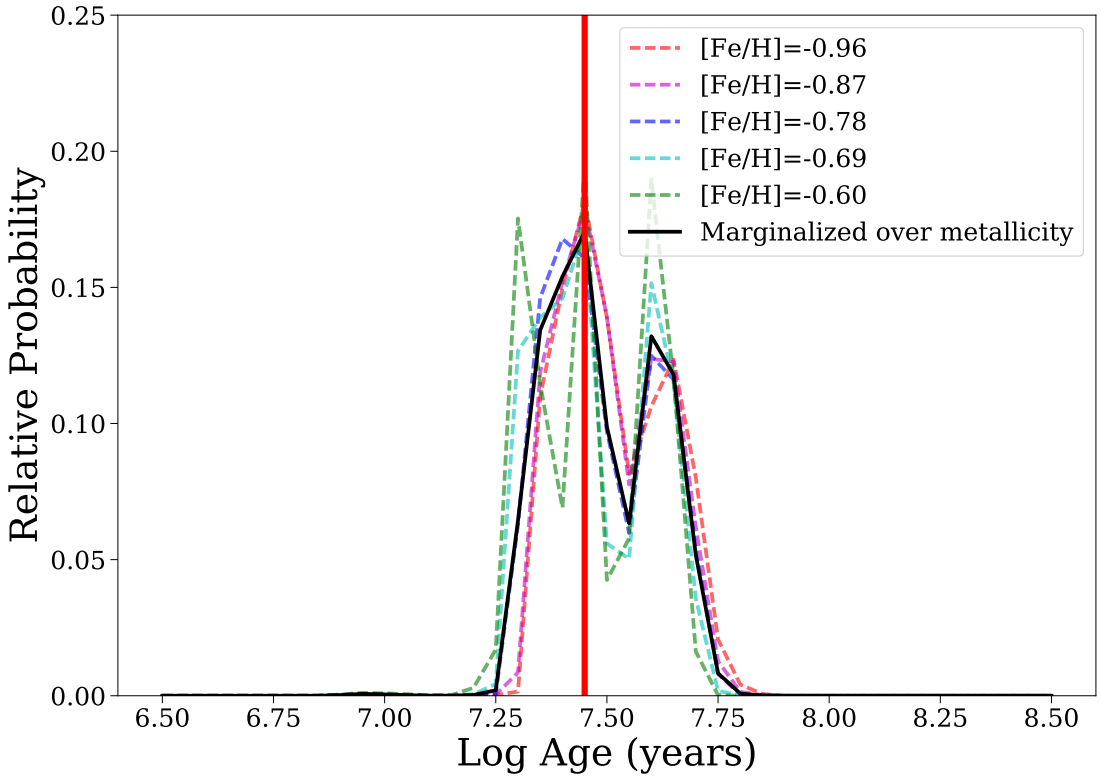

Figure 4.9: The probability distribution recovered from an injected age of $10^{7.45}$ years. The injected age is labeled with the vertical red line. The dotted lines show the recovered distributions for a variety of assumed metallicities, while the solid black line shows the distribution from marginalizing over the prior in metallicity.

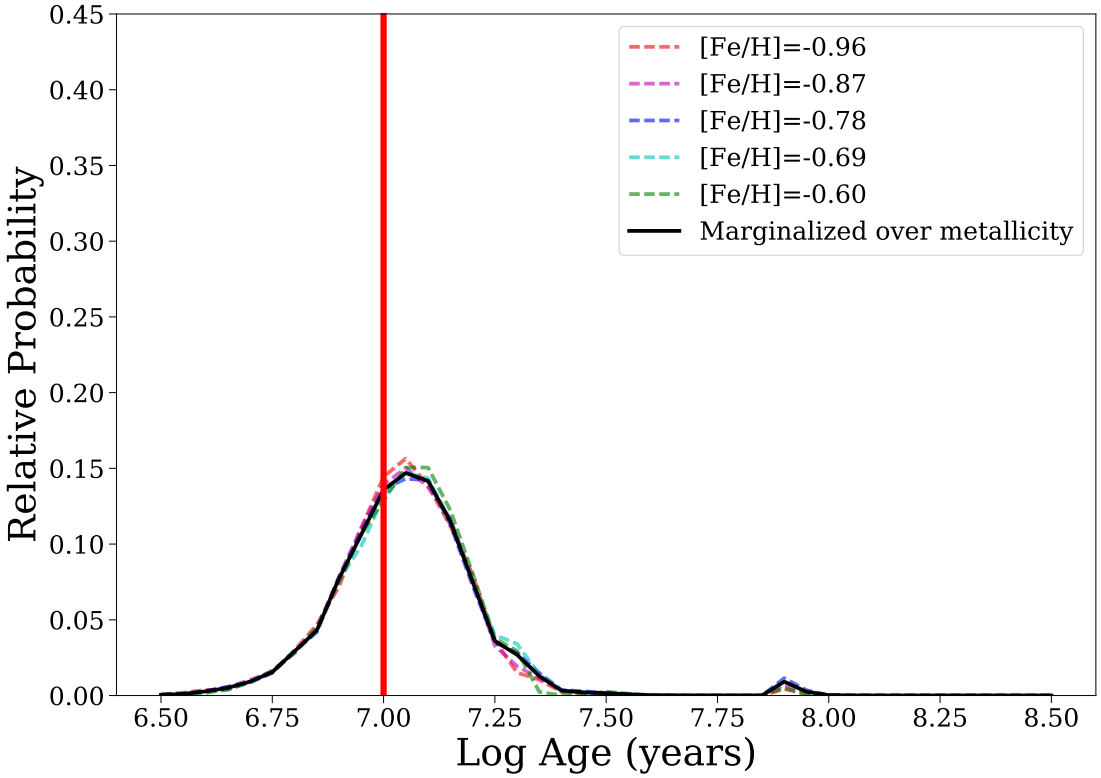

Figure 4.10: The probability distribution recovered from an injected age of 10^7 years. The injected age is labeled with the vertical red line. The dotted lines show the recovered distributions for a variety of assumed metallicities, while the solid black line shows the distribution from marginalizing over the prior in metallicity.

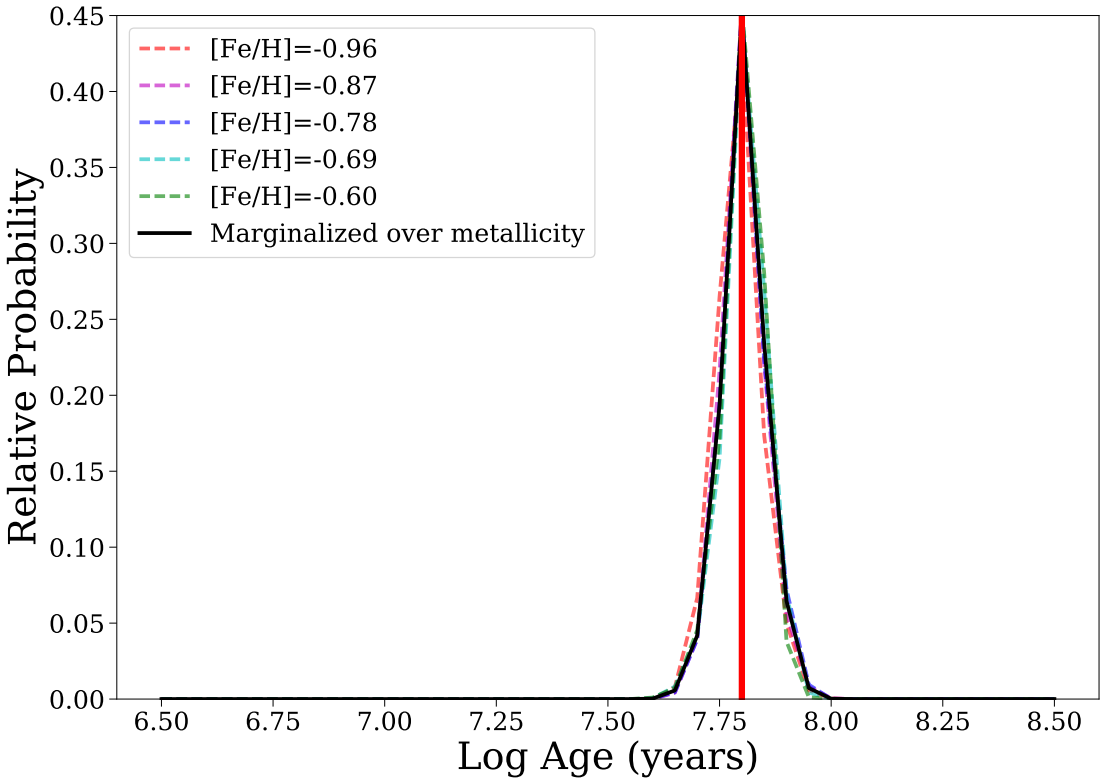

Figure 4.11: The probability distribution recovered from an injected age of $10^{7.8}$ years. The injected age is labeled with the vertical red line. The dotted lines show the recovered distributions for a variety of assumed metallicities, while the solid black line shows the distribution from marginalizing over the prior in metallicity.

Bibliography

Anderson, J., & Bedin, L. R. 2010, PASP, 122, 1035

Andrews, S. M., Hughes, A. M., Wilner, D. J., & Qi, C. 2008, ApJ, 678, L133

Asplund, M., Grevesse, N., Sauval, A. J., & Scott, P. 2009, ARA&A, 47, 481

Badenes, C., Harris, J., Zaritsky, D., & Prieto, J. L. 2009, ApJ, 700, 727

Barna, B., Szalai, T., Kromer, M., et al. 2017, MNRAS, 471, 4865

Bastian, N., & Goodwin, S. P. 2006, MNRAS, 369, L9

Batalha, N. M., Rowe, J. F., Bryson, S. T., et al. 2013, ApJS, 204, 24

Beckwith, S. V. W., Henning, T., & Nakagawa, Y. 2000, in Protostars and Planets IV, ed. V. Mannings, A. P. Boss, & S. S. Russell, 533

Beitz, E., Güttler, C., Blum, J., et al. 2011, ApJ, 736, 34

Bertin, E., Mellier, Y., Radovich, M., et al. 2002, in Astronomical Society of the Pacific Conference Series, Vol. 281, Astronomical Data Analysis Software and Systems XI, ed. D. A. Bohlender, D. Durand, & T. H. Handley, 228

Bertout, C., Siess, L., & Cabrit, S. 2007, A&A, 473, L21

Birnstiel, T., Klahr, H., & Ercolano, B. 2012, A&A, 539, A148

Bitsch, B., Izidoro, A., Johansen, A., et al. 2019, A&A, 623, A88

Bitsch, B., Morbidelli, A., Johansen, A., et al. 2018, A&A, 612, A30

Blanchard, P., Cenko, S. B., Li, W., et al. 2011, Central Bureau Electronic Telegrams, 2678

Borucki, W. J., Koch, D., Basri, G., et al. 2010, Science, 327, 977

Branch, D., Baron, E., Thomas, R. C., et al. 2004, PASP, 116, 903

Brauer, F., Dullemond, C. P., & Henning, T. 2008, A&A, 480, 859

Brauer, F., Dullemond, C. P., Johansen, A., et al. 2007, A&A, 469, 1169

Cardelli, J. A., Clayton, G. C., & Mathis, J. S. 1989, ApJ, 345, 245

Cenko, S. B., Li, W., & Filippenko, A. V. 2012, The Astronomer's Telegram, 3900

Chambers, J. E. 2016, ApJ, 825, 63

Chandar, R., Whitmore, B. C., Kim, H., et al. 2010, ApJ, 719, 966

Chevalier, R. A., & Fransson, C. 2006, ApJ, 651, 381

Chiang, E., & Youdin, A. N. 2010, Annual Review of Earth and Planetary Sciences, 38, 493

Choi, J., Dotter, A., Conroy, C., et al. 2016, ApJ, 823, 102

Claeys, J. S. W., Pols, O. R., Izzard, R. G., Vink, J., & Verbunt, F. W. M. 2014, A&A, 563, A83

Della Valle, M., Chincarini, G., Panagia, N., et al. 2006, Nature, 444, 1050

Dohnanyi, J. S. 1969, J. Geophys. Res., 74, 2531

Dolphin, A. E. 2000, PASP, 112, 1383

Dominik, C., Blum, J., Cuzzi, J. N., & Wurm, G. 2007, in Protostars and Planets V, ed. B. Reipurth, D. Jewitt, & K. Keil, 783

Dotter, A. 2016, ApJS, 222, 8

Dressler, A., Bigelow, B., Hare, T., et al. 2011, PASP, 123, 288

Eldridge, J. J., Langer, N., & Tout, C. A. 2011, MNRAS, 414, 3501

Eldridge, J. J., Stanway, E. R., Xiao, L., et al. 2017, PASA, 34, e058

Fink, M., Kromer, M., Seitenzahl, I. R., et al. 2014, MNRAS, 438, 1762

Foley, R. J. 2013, MNRAS, 435, 273

Foley, R. J., Brown, P. J., Rest, A., et al. 2010a, ApJ, 708, L61

Foley, R. J., Jha, S. W., Pan, Y.-C., et al. 2016, MNRAS, 461, 433

Foley, R. J., McCully, C., Jha, S. W., et al. 2014, ApJ, 792, 29

Foley, R. J., Van Dyk, S. D., Jha, S. W., et al. 2015, ApJ, 798, L37

Foley, R. J., Chornock, R., Filippenko, A. V., et al. 2009, AJ, 138, 376

Foley, R. J., Rest, A., Stritzinger, M., et al. 2010b, AJ, 140, 1321

Foley, R. J., Challis, P. J., Chornock, R., et al. 2013, ApJ, 767, 57

Foreman-Mackey, D., Hogg, D. W., Lang, D., & Goodman, J. 2013, PASP, 125, 306

Fressin, F., Torres, G., Charbonneau, D., et al. 2013, ApJ, 766, 81

Fryer, C. L. 1999, ApJ, 522, 413

Fryer, C. L., Brown, P. J., Bufano, F., et al. 2009, ApJ, 707, 193

Garaud, P. 2007, ApJ, 671, 2091

Geller, A. M., Mathieu, R. D., Harris, H. C., & McClure, R. D. 2009, AJ, 137, 3743

Gogarten, S. M., Dalcanton, J. J., Murphy, J. W., et al. 2009, ApJ, 703, 300

Gouliermis, D. A., Elmegreen, B. G., Elmegreen, D. M., et al. 2017, MNRAS, 468, 509

Guillochon, J., Parrent, J., Kelley, L. Z., & Margutti, R. 2017, ApJ, 835, 64

Guillot, T., Ida, S., & Ormel, C. W. 2014, A&A, 572, A72

Hachisu, I., Kato, M., Nomoto, K., & Umeda, H. 1999, ApJ, 519, 314

Heger, A., Fryer, C. L., Woosley, S. E., Langer, N., & Hartmann, D. H. 2003, ApJ, 591, 288

Herbig, G. H., & Bell, K. R. 1988,

Hicken, M., Challis, P., Kirshner, R. P., et al. 2012, ApJS, 200, 12

Housen, K. R., & Holsapple, K. A. 1990, Icarus, 84, 226

—. 1999, Icarus, 142, 21

Ida, S., Guillot, T., & Morbidelli, A. 2016, A&A, 591, A72

Immler, S., Brown, P. J., Milne, P., et al. 2006, ApJ, 648, L119

Jennings, Z. G., Williams, B. F., Murphy, J. W., et al. 2012, ApJ, 761, 26

—. 2014, ApJ, 795, 170

Jha, S., Branch, D., Chornock, R., et al. 2006, AJ, 132, 189

Jha, S. W. 2017, in Handbook of Supernovae, ed. A. W. Alsabti & P. Murdin, 375

Johansen, A., & Lambrechts, M. 2017, Annual Review of Earth and Planetary Sciences, 45, 359

Johansen, A., Oishi, J. S., Mac Low, M.-M., et al. 2007, Nature, 448, 1022

Jordan, IV, G. C., Perets, H. B., Fisher, R. T., & van Rossum, D. R. 2012, ApJ, 761, L23

Jorgensen, I. 1997, MNRAS, 288, 161

Kanagawa, K. D., Muto, T., Okuzumi, S., et al. 2018, ApJ, 868, 48

Kromer, M., Fink, M., Stanishev, V., et al. 2013, MNRAS, 429, 2287

Kromer, M., Ohlmann, S. T., Pakmor, R., et al. 2015, MNRAS, 450, 3045

Kroupa, P. 2001, MNRAS, 322, 231

Kuncarayakti, H., Doi, M., Aldering, G., et al. 2013a, AJ, 146, 30

—. 2013b, AJ, 146, 31

Kusaka, T., Nakano, T., & Hayashi, C. 1970, Progress of Theoretical Physics, 44, 1580

Lada, C. J. 2010, Philosophical Transactions of the Royal Society of London Series A, 368, 713

Lambrechts, M., & Johansen, A. 2012, A&A, 544, A32

—. 2014, A&A, 572, A107

Lambrechts, M., Johansen, A., & Morbidelli, A. 2014, A&A, 572, A35

Lee, E. J., & Chiang, E. 2016, ApJ, 817, 90

Levesque, E. M., Kewley, L. J., Berger, E., & Zahid, H. J. 2010, AJ, 140, 1557

Levison, H. F., Kretke, K. A., Walsh, K. J., & Bottke, W. F. 2015, Proceedings of the National Academy of Science, 112, 14180

Li, L., Wang, X., Zhang, J., et al. 2018, MNRAS, 478, 4575

Li, W., Filippenko, A. V., Chornock, R., et al. 2003, PASP, 115, 453

Liu, W.-M., Chen, W.-C., Wang, B., & Han, Z. W. 2010, A&A, 523, A3

Liu, Z.-W., Moriya, T. J., Stancliffe, R. J., & Wang, B. 2015, A&A, 574, A12

Long, M., Jordan, IV, G. C., van Rossum, D. R., et al. 2014, ApJ, 789, 103

Lyman, J. D., James, P. A., Perets, H. B., et al. 2013, MNRAS, 434, 527

Lyman, J. D., Taddia, F., Stritzinger, M. D., et al. 2018, MNRAS, 473, 1359

Magee, M. R., Kotak, R., Sim, S. A., et al. 2016, A&A, 589, A89

Maíz-Apellániz, J., Bond, H. E., Siegel, M. H., et al. 2004, ApJ, 615, L113

Margutti, R., Parrent, J., Kamble, A., et al. 2014, ApJ, 790, 52

Margutti, R., Soderberg, A. M., Chomiuk, L., et al. 2012, ApJ, 751, 134

Masi, G., Brimacombe, J., James, N., et al. 2014, Central Bureau Electronic Telegrams, 3949

Mathis, J. S., Rumpl, W., & Nordsieck, K. H. 1977, ApJ, 217, 425

Maund, J. R. 2017, MNRAS, 469, 2202

—. 2018, MNRAS, 476, 2629

Maund, J. R., & Ramirez-Ruiz, E. 2016, MNRAS, 456, 3175

McClure, M. K. 2019, A&A, 632, A32

McCully, C., Jha, S. W., Foley, R. J., et al. 2014a, Nature, 512, 54

—. 2014b, ApJ, 786, 134

Meng, X., & Yang, W. 2010, ApJ, 710, 1310

Miller, A. A., Kasliwal, M. M., Cao, Y., et al. 2017, ApJ, 848, 59

Miller, N. A., & Owen, F. N. 2001, ApJS, 134, 355

Milne, P. A., Brown, P. J., Roming, P. W. A., et al. 2010, ApJ, 721, 1627

Monard, L. A. G. 2010, Central Bureau Electronic Telegrams, 2334

Morbidelli, A., Lambrechts, M., Jacobson, S., & Bitsch, B. 2015, Icarus, 258, 418

Morbidelli, A., & Nesvorny, D. 2012, A&A, 546, A18

Moriya, T., Tominaga, N., Tanaka, M., et al. 2010, ApJ, 719, 1445

Murphy, J. W., Jennings, Z. G., Williams, B., Dalcanton, J. J., & Dolphin, A. E. 2011, ApJ, 742, L4

Nakano, S., Ichimura, Y., Itagaki, K., Kadota, K., & Hirose, Y. 2008, Central Bureau Electronic Telegrams, 1193

Natta, A., Testi, L., Neri, R., Shepherd, D. S., & Wilner, D. J. 2004, A&A, 416, 179

Ochner, P., Tomasella, L., Benetti, S., et al. 2014, The Astronomer's Telegram, 6648

Ormel, C. W., & Cuzzi, J. N. 2007, A&A, 466, 413

Ormel, C. W., & Klahr, H. H. 2010, A&A, 520, A43

Ormel, C. W., & Kobayashi, H. 2012, ApJ, 747, 115

Paxton, B., Bildsten, L., Dotter, A., et al. 2011, ApJS, 192, 3

Paxton, B., Cantiello, M., Arras, P., et al. 2013, ApJS, 208, 4

Paxton, B., Marchant, P., Schwab, J., et al. 2015, ApJS, 220, 15

Perets, H. B., & Murray-Clay, R. A. 2011, ApJ, 733, 56

Petigura, E. A., Howard, A. W., & Marcy, G. W. 2013, Proceedings of the National Academy of Science, 110, 19273

Phillips, M. M., Li, W., Frieman, J. A., et al. 2007, PASP, 119, 360

Picogna, G., Stoll, M. H. R., & Kley, W. 2018, A&A, 616, A116

Piersanti, L., Tornambé, A., & Yungelson, L. R. 2014, MNRAS, 445, 3239

Pignata, G., Maza, J., Hamuy, M., et al. 2008, Central Bureau Electronic Telegrams, 1531

Pignata, G., Cifuentes, M., Maza, J., et al. 2010, Central Bureau Electronic Telegrams, 2184

Piso, A.-M. A., & Youdin, A. N. 2014, ApJ, 786, 21

Postnov, K. A., & Yungelson, L. R. 2014, Living Reviews in Relativity, 17, 3

Powell, D., Murray-Clay, R., Pérez, L. M., Schlichting, H. E., & Rosenthal, M. 2019, ApJ, 878, 116

Powell, D., Murray-Clay, R., & Schlichting, H. E. 2017, ApJ, 840, 93

Puckett, T., Moore, C., Newton, J., & Orff, T. 2008, Central Bureau Electronic Telegrams, 1567

Pumo, M. L., Turatto, M., Botticella, M. T., et al. 2009, ApJ, 705, L138

Qi, C., Öberg, K. I., Wilner, D. J., et al. 2013, Science, 341, 630

Rest, A., Stubbs, C., Becker, A. C., et al. 2005, ApJ, 634, 1103

Rest, A., Scolnic, D., Foley, R. J., et al. 2014, ApJ, 795, 44

Rhee, J. H., Song, I., Zuckerman, B., & McElwain, M. 2007, ApJ, 660, 1556

Ricci, L., Testi, L., Natta, A., et al. 2010, A&A, 512, A15

Riess, A. G., Macri, L. M., Hoffmann, S. L., et al. 2016, ApJ, 826, 56

Rodríguez, Ó., Clocchiatti, A., & Hamuy, M. 2014, AJ, 148, 107

Röpke, F. K. 2005, A&A, 432, 969

Rosenthal, M. M., & Murray-Clay, R. A. 2018, ApJ, 864, 66

—. 2020, ApJ, 898, 108

Rosenthal, M. M., Murray-Clay, R. A., Perets, H. B., & Wolansky, N. 2018, ApJ, 861, 74

Ruiter, A. J., Belczynski, K., & Fryer, C. 2009, ApJ, 699, 2026

Ruiter, A. J., Belczynski, K., Sim, S. A., et al. 2011, MNRAS, 417, 408

Russell, B. R., & Immler, S. 2012, ApJ, 748, L29

Sahu, D. K., Tanaka, M., Anupama, G. C., et al. 2008, ApJ, 680, 580

Schlafly, E. F., & Finkbeiner, D. P. 2011, ApJ, 737, 103

Shakura, N. I., & Sunyaev, R. A. 1973, A&A, 24, 337

Stewart, S. T., & Leinhardt, Z. M. 2009, ApJ, 691, L133

Stritzinger, M. D., Hsiao, E., Valenti, S., et al. 2014, A&A, 561, A146

Stritzinger, M. D., Valenti, S., Hoeflich, P., et al. 2015, A&A, 573, A2

STSCI Development Team. 2012, DrizzlePac: HST image software, Astrophysics Source Code Library, ascl:1212.011

Szalai, T., Vinkó, J., Sárneczky, K., et al. 2015, MNRAS, 453, 2103

Taddia, F., Sollerman, J., Fremling, C., et al. 2015, A&A, 580, A131

Takaro, T., Foley, R. J., McCully, C., et al. 2020, MNRAS, 493, 986

Testi, L., Birnstiel, T., Ricci, L., et al. 2014, in Protostars and Planets VI, ed. H. Beuther, R. S. Klessen, C. P. Dullemond, & T. Henning, 339

Theureau, G., Hanski, M. O., Coudreau, N., Hallet, N., & Martin, J. M. 2007, A&A, 465, 71

Tomasella, L., Cappellaro, E., Benetti, S., et al. 2016, MNRAS, 459, 1018

Tully, R. B., Courtois, H. M., Dolphin, A. E., et al. 2013, AJ, 146, 86

Valenti, S., Pastorello, A., Cappellaro, E., et al. 2009, Nature, 459, 674

Visser, R. G., & Ormel, C. W. 2016, A&A, 586, A66

Wang, B., Chen, X., Meng, X., & Han, Z. 2009a, ApJ, 701, 1540

Wang, B., Justham, S., & Han, Z. 2013, A&A, 559, A94

Wang, B., Meng, X., Chen, X., & Han, Z. 2009b, MNRAS, 395, 847

Wang, B., Meng, X., Liu, D.-D., Liu, Z.-W., & Han, Z. 2014, ApJ, 794, L28

Weidenschilling, S. J. 1977, in IAU Colloq. 39: Comets, Asteroids, Meteorites: Interrelations, Evolution and Origins, ed. A. H. Delsemme, 541–544

Weidenschilling, S. J. 1984, Icarus, 60, 553

White, C. J., Kasliwal, M. M., Nugent, P. E., et al. 2015, ApJ, 799, 52

Williams, B. F., Peterson, S., Murphy, J., et al. 2014, ApJ, 791, 105

Xu, Z., Bai, X.-N., & Murray-Clay, R. A. 2017, ApJ, 847, 52

Yamanaka, M., Maeda, K., Kawabata, K. S., et al. 2015, ApJ, 806, 191

Youdin, A. N., & Goodman, J. 2005, ApJ, 620, 459

Youdin, A. N., & Lithwick, Y. 2007, Icarus, 192, 588

Zhu, W., Petrovich, C., Wu, Y., Dong, S., & Xie, J. 2018, ApJ, 860, 101

Zsom, A., Ormel, C. W., Güttler, C., Blum, J., & Dullemond, C. P. 2010, A&A, 513, A57

Zubko, V., Dwek, E., & Arendt, R. G. 2004, ApJS, 152, 211